ISSN Print: 2518-4245
ISSN Online: 2518-4253
Vol. 62(3), September 2025

PROCEEDINGS
OF THE PAKISTAN ACADEMY OF SCIENCES:
A. Physical and Computational Sciences

PAKISTAN ACADEMY OF SCIENCES
ISLAMABAD, PAKISTAN

Proceedings of the Pakistan Academy of Sciences: Part A Physical and Computational Sciences

Proceedings of the Pakistan Academy of Sciences A. Physical and Computational Sciences is the official flagship, the peer-reviewed quarterly journal of the Pakistan Academy of Sciences. This open-access journal publishes original research articles and reviews on current advances in the field of Computer Science (all), Materials Science (all), Physics and Astronomy (all), Engineering Sciences (all), Chemistry, Statistics, Mathematics, Geography, Geology in English. Authors are not required to be Fellows or Members of the Pakistan Academy of Sciences or citizens of Pakistan. The journal is covered by Print and Online ISSN, indexed in Scopus, and distributed to scientific organizations, institutes and universities throughout the country, by subscription and on an exchange basis.

Annual Subscription: **Pakistan:** Institutions, Rupees 8000/-; Individuals, Rupees 4000/- (Delivery Charges: Rupees 300/-)
Other Countries: US$ 200.00 (includes air-lifted overseas delivery)

HEC Recognized; Scopus Indexed

Published by **Pakistan Academy of Sciences**, 3 Constitution Avenue, G-5/2, Islamabad, Pakistan
Email: editor@paspk.org; **Tel:** 92-51-920 7140 & 921 5478; **Websites:** www.paspk.org/proceedings/; www.ppaspk.org

Printed at **Graphics Point.,** Office 3-A, Wasal Plaza, Fazal-e-Haq Road Blue Area Islamabad.
Ph: 051-2806257, **E-mail:** graphicspoint16@gmail.com

PROCEEDINGS OF THE
PAKISTAN ACADEMY OF SCIENCES: PART A
Physical and Computational Sciences

CONTENTS

Volume 62, No. 3, September 2025 **Page**

Research Articles

Instructions for Authors

Submission of Manuscripts: Manuscripts may be submitted as an e-mail attachment at editor@paspk.org or submit online at http://ppaspk.org/index.php/PPASA/about/submissions. Authors must consult the ***Instructions for Authors*** at the end of this issue or at the Website: www.paspk.org/proceedings/ or www.ppaspk.org.

Proceedings of the Pakistan Academy of Sciences: A Physical and Computational Sciences 62(3): 193-207 (2025)

ISSN (Print): 2518-4245; ISSN (Online): 2518-4253
http://doi.org/10.53560/PPASA(62-3)843

Pakistan Academy of Sciences

Research Article

Assessing Drought Vulnerability in Pakistan (2001-2022) Using EVI-Based Standardized Vegetation Index in Google Earth Engine

Imran Ahmed Khan[1]*, Shah Jahan Leghari[2], and Keshab Magar[3]

[1]Department of Geography, University of Karachi, Karachi 75270, Pakistan
[2]College of Mechanical and Electronical Engineering, Northwest A&F University, Yangling, Shaanxi, 712100, China
[3]Faculty of Science Health & Technology, Nepal Open University, Nepal

Abstract: This study examines vegetation dynamics and drought risk in Pakistan from 2001 to 2022 using MODIS Enhanced Vegetation Index (EVI) and Standardized Vegetation Index (SVI) processed in Google Earth Engine. EVI highlights high greenness in the irrigated plains of Punjab and Sindh, while SVI exposes widespread stress in these same areas, revealing a "greening paradox" where apparent productivity masks underlying vulnerability. Monthly SVI patterns follow strong seasonal cycles, with positive anomalies peaking during the monsoon driven kharif season (June-October) and persistent deficits occurring in the rabi season (December–May). Spatially, high EVI values (>0.4) were concentrated along the Indus River corridor, while arid zones such as Balochistan and the Thar Desert exhibited low EVI (<0.2). Mean SVI maps contradicted these patterns, showing negative anomalies in high EVI regions. Long term analysis indicated stable EVI until 2018, followed by a modest upward trend, while SVI shifted from chronic negative anomalies in the early 2000s (mean = –0.21) to sustained positive values after 2020 (mean = +0.58). At the provincial scale, Punjab showed a post 2015 decline, Sindh demonstrated recovery after drought episodes in 2010-2012 and 2017-2018, Khyber Pakhtunkhwa displayed high variability without a clear trend, and Balochistan recorded the strongest improvement since 2005. Overall, EVI captured absolute greenness, while SVI provided anomaly based insights into drought conditions, detecting hidden stress in intensively irrigated areas and identifying genuine recovery in marginal regions. By integrating EVI and SVI, this study offers a robust framework for spatiotemporal drought monitoring in Pakistan. The results provide a scientific basis for climate smart agriculture, early warning systems, and sustainable land and water management strategies aimed at safeguarding food security in the face of rising drought frequency.

Keywords: Standardized Vegetation Index (SVI), Drought Vulnerability, Vegetation Stress, Remote Sensing, Google Earth Engine (GEE), Drought in Pakistan.

1. INTRODUCTION

Agriculture serves as the foundation for numerous businesses and provides millions of people with a means of subsistence [1]. However, unpredictable weather brought on by climate change has drastically decreased agricultural output. Drought disaster is one of the most frequent, severe natural disasters widespread on a year to year basis. As a result, climate smart agribusiness is now more important than ever. With this approach, agricultural productivity is intended to increase while mitigating and adjusting to the impacts of climate change [2-4]. Climate smart agriculture now requires the use of remote sensing and machine learning methods on cloud data [5]. In remote sensing, sensors are used to collect data on the earth's surface and atmosphere [6]. This technique makes it possible to get information on crucial agricultural characteristics including crop health and soil moisture. As a result, choices may be made about crop management, such as when to schedule irrigation, fertilize, and apply pesticides [7]. In addition, crop monitoring and forecasting are aided by remote sensing [8].

Received: November 2023; Revised: August 2025; Accepted: September 2025
* Corresponding Author: Imran Ahmed Khan <imranak32@uok.edu.pk>

Unlike sudden onset disasters such as floods or earthquakes, drought is a slow onset hazard that is often difficult to define precisely due to its creeping nature, spatial variability, and delayed socio economic impacts. Drought occurrences are classified into four major categories based on the sectors they impact: meteorological, agricultural, hydrological, and socio economic drought. This study focuses primarily on agricultural drought defined as a period during which soil moisture falls below the level required for normal crop growth and development as it directly affects food production and rural livelihoods in Pakistan.

For agriculture, drought is characterized by a period of soil moisture being less than the amount required for normal plant growth and development [9]. Numerous methods for monitoring and quantitatively describing drought have been developed during the last few decades, including the development of drought indices used in meteorology, hydrology, and agriculture. Traditional drought monitoring techniques rely on indices derived from meteorological station data such as precipitation. A number of the most broadly utilized meteorological drought indexes based only on this parameter is the World Meteorological Organization's (WMO) proposed Standardized Precipitation Index (SPI).

However, other climatic factors, including as evapotranspiration and temperature, impact the occurrence and severity of droughts. Beguera *et al*. [10] introduced the Standardized Precipitation Evapotranspiration Index (SPEI), which is based on both precipitation and potential evapotranspiration (PET). SPEI, like SPI, may be calculated at time intervals ranging from one to forty eight months. According to several researches, a 3 month SPI and SPEI are preferable for monitoring the impacts of drought on plants [11]. Since traditional station based drought monitoring systems required continuous historical information, satellite based methods give rapid and realistic findings for close to real time acquisition, drought analysis, and extensive and continuous geographic coverage [12].

Tucker and Choudhury [13] applied the Normalized Vegetation Index (NDVI) as a satellite based drought monitoring tool. The greatest and widely used satellite based vegetation indicator 'NDVI' offers a useful indication of vegetation moisture conditions. In addition to NDVI, Land Surface Temperature (LST) derived from thermal satellite bands are used to improve drought measurements as temperature rises and soil moisture reduces.

Subsequently, numerous vegetation indices (VIs) like the Vegetation Condition Index (VCI) were developed to better the research of vegetation states without weathering, particularly in non homogeneous areas. Because of its amplified sensitivity to water stress, temperature was also employed to develop drought indices such as the Temperature Condition Index (TCI) [14]. Drought indices including VCI and TCI can efficiently identify drought conditions since the combination of NDVI and LST provides statistics on both vegetation and moisture. Finally, scientists created the Vegetation Health Index (VHI) based on a numerical combination of VCI and TCI [15]. Using machine learning on cloud data, like Google Earth Engine (GEE), makes it possible to examine remote sensing information, more quickly and affordably [16]. Machine learning algorithms can be trained on large datasets in order to find trends and forecast future crop yields or other crucial agricultural parameters. These forecasts can be used to improve crop management techniques, lower input costs, and boost total productivity [17].

The standardized vegetation index (SVI) is one of the most important instruments for climate smart agriculture [18]. SVI, a measurement of plant development and cover, is created using satellite data. Since drought conditions may significantly affect agricultural productivity, the indicator is especially helpful for keeping track of them. The Enhanced Vegetation Index (EVI), a gauge of vegetation greenness, may be used to determine the SVI. The EVI is then normalized to produce an index that may be utilized to contrast various places and periods [19]. SVI may be used as a drought mitigation tool and to detect water stress early on by tracking plant growth and cover [20].

This study operationalizes the SVI via Google Earth Engine (GEE) to deliver scalable, near real time drought intelligence for Pakistan. As country is a climate vulnerable region increasingly beset by intensifying water scarcity, prolonged dry spells, and more frequent and severe extreme weather events,

thus enabling proactive, data driven responses to agricultural stress. With employing SVI to enhance climate smart farming decision making is especially critical during periods of drought as early detection allows farmers and government agencies to implement timely interventions for adjusting irrigation schedules, shifting planting dates, or selecting drought resilient crop varieties. This can significantly mitigate yield losses and reduce systemic vulnerability to water shortages, ultimately supporting food security and rural livelihoods [21, 22].

The utility of SVI extends beyond mere drought assessment, as it provides a robust, spatially explicit indicator that can inform adaptive land management strategies, optimize resource allocation, improve crop yield forecasts, and help buffer agricultural systems against the escalating impacts of climate change, including rising temperatures, erratic rainfall patterns, and accelerated soil degradation. This study is good to leverage the power of cloud based remote sensing and Google Earth Engine to compute, monitor, and map SVI across Pakistan's diverse agro ecological zones, where recurrent droughts, declining groundwater tables, and extreme climatic variability have rendered traditional monitoring approaches inadequate. Pakistan needs an integrated, high resolution, and operationally feasible drought early warning system to safeguard national agricultural resilience in an era of accelerating environmental uncertainty.

This study aims to establish a satellite based, cloud computing framework for agricultural drought monitoring in Pakistan using the Standardized Vegetation Index (SVI). Specifically, it seeks to:

(1) To generate multi decadal (2001-2022) SVI and EVI time series for Pakistani provinces using MODIS data within Google Earth Engine;
(2) To characterize mean, monthly, and inter annual patterns of vegetation stress to identify regional drought vulnerabilities and seasonal dynamics;
(3) To evaluate SVI's performance in capturing agriculturally relevant drought signals compared to traditional metrics; and
(4) To make the foundation for integrating SVI analytics into national early warning systems and climate smart agricultural policies for supporting targeted interventions in irrigation, crop selection.

2. MATERIALS AND METHODS

2.1. Study Area

Pakistan is a South Asian nation bordered to the east by India, to the northwest by Afghanistan, to the west by Iran, and to the northeast by China (Figure 1). It has a total land size of approximately 881,913 km² and a diverse topography of mountains, plateaus, and plains. Agriculture industry contributes significantly to the country's economy and employing approximately 42% of the labour force and accounts for more than one fifth of GDP share. The farming is heavily dependent on irrigation, as around 90% of its agricultural land needs irrigation water. The main crops are wheat, rice, cotton, sugarcane, and maize, these are among Pakistan's for food and export items,also significant production of fruits and vegetables such as mangoes, citrus, apples, and potatoes. The agriculture industry in Pakistan is confronted with a number of issues, including water scarcity, soil degradation, and climate change [23]. Pakistan has experienced severe droughts in recent years and affecting its agriculture. The agriculture sector is also vulnerable to floods that can cause extensive damage to crops and infrastructure [24, 25]. The Pakistani government has launched a number of initiatives in response to these challenges, including irrigation techniques and new methods, to support climate smart agriculture practices. These initiatives aim to increase agricultural productivity while mitigating the negative impacts of climate change [23]. The government is also investing in the study and creation of new technologies and practices to improve the efficiency and sustainability of

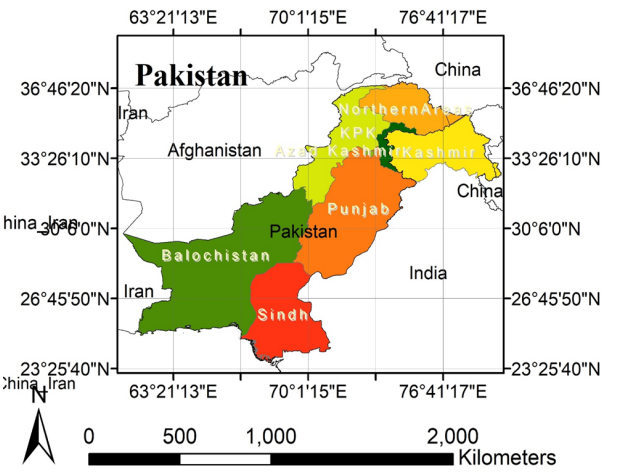

Fig. 1. Study area Pakistan.

agriculture, as country geography and topography make it ideal for agriculture which is a significant contributor to the country's economy [26]. Though, country still faces a number of challenges, such as water scarcity, soil degradation, and climate change, necessitating the creation of novel solutions and practices [27].

2.2. MODIS Data Product (MOD13Q1)

The MOD13Q1 is a product of the Moderate Resolution Imaging Spectroradiometer (MODIS) sensor aboard NASA's Terra and Aqua satellites. It is a vegetation index dataset, global data is available that provides information on vegetation health and productivity at a spatial resolution of 250 meters. This MOD13Q1 data is using in many applications such as crop monitoring, land cover classification, and climate change studies [28, 29]. MOD13Q1 provides both the Normalized Difference Vegetation Index (NDVI) and Enhanced Vegetation Index (EVI) data products. However, in this study only MODIS derived EVI product has been used.

2.3. Enhanced Vegetation Index (EVI)

MODIS is an excellent sensor system, this is one of NASA's most extensively used in scientific studies. MODIS product/vegetation datasets is the MOD13Q1, this global level product provides reliable and high quality measures of vegetation health and productivity. This has a spatial resolution of 250 meters with biweekly temporal coverage, and is widely used in the scientific and operational areas. The MOD13Q1 data is useful for applications such as crop monitoring, land cover categorization, drought assessment, phenological analysis, and long term climate change studies. Its uniform processing, substantial archive since 2000 and multi sensor continuity make it a must have resource for understanding terrestrial ecosystem processes at regional and global scales [28-31].

The EVI equation includes blue and red bands, as well as the near infrared band. The equation is:

$$EVI = 2.5 \times \frac{(NIR - Red)}{NIR + 6 \times Red - 7.5 \times Blue + L} \quad (1)$$

Where, NIR is the reflectance in the near infrared band, Red is the reflectance in the red band, and Blue is the reflectance in the blue band.

In an attempt to provide a more accurate measurement of vegetation canopy, the factors in the equation are employed to lessen the impact of the aerosol component of the atmosphere on the vegetation signal. Higher numbers denote more plant density and good growth, and the resulting EVI values range from -1 to +1.

2.4. Standardized Vegetation Index (SVI)

The SVI is a standardised measure that may be used to assess the productivity and health of vegetation in various places and throughout various time periods, particularly during extreme weather. This index offers information on the length and severity of droughts as well as how they affect vegetation [32]. SVI is derived from EVI by standardizing the EVI values across time and space:

$$SVI = \frac{(EVI - \text{mean}(EVI))}{\text{standard deviation}(EVI)} \quad (2)$$

Where, mean(EVI) is the average EVI value across a specified time period and area, and standard deviation (EVI) is the standard deviation of EVI across the same time period and area.

SVI evaluation applying MODIS EVI data in Google Earth Engine (GEE) involves a number of processes. The accuracy of the study is increased by first filtering the data from MODIS EVI by date and area of interest (AOI). The EVI range is then scaled to -1 to +1 after the filters have been applied to the data. Each image has statistics computed for it, such as mean values and standard deviation [33]. The rescaled EVI data, mean, and standard deviation numbers are then factored into a formula to determine the SVI. The mean EVI, and SVI image are used for visualization. The rescaled EVI data, mean, and standard deviation numbers are then factored into a formula to determine the SVI. The mean EVI, most recent EVI and SVI image are all included in the data display process using GEE. This method offers a quick and precise means to evaluate SVI using MODIS EVI data using GEE [34]. Provincial wise time series data were retrieved on monthly SVI data from 2001 to 2022, finally, mean SVI for whole Pakistan was calculated.

3. RESULTS AND DISCUSSION

The EVI was calculated for the entire Pakistan region. The mean EVI map shows high vegetation

productivity (>0.4) along the Indus River corridor in Punjab and Sindh, driven by irrigation and agriculture. Lower values (<0.2) dominate arid regions like Balochistan and the Thar Desert, reflecting limited biomass. Negative values in mountainous and urban areas suggest bare soil (Figure 2). Monthly SVI datasets were used to obtain the mean SVI index for Pakistan indicating significant deviations from long term climatological norms. Negative SVI values (yellow to red) dominate central and southern regions, reflecting persistent drought conditions in irrigated and rainfed agricultural zones. In contrast, positive SVI values (green) are localized in northern mountainous areas and in many parts of Balochistan, suggesting above average vegetation health during the study period (Figure 3).

3.1. Mean Monthly EVI and SVI Dynamics in Pakistan (2001 2022)

Figure 4 shows mean monthly EVI and SVI dynamics in Pakistan during the study period. This monthly averaged EVI and SVI reveal distinct seasonal patterns that closely align with the region's dual cropping agricultural system. EVI, which serves as a robust proxy for vegetation density and photosynthetic activity, exhibits a bimodal distribution with two pronounced peaks: one in February (0.153) and another in August (0.164). These peaks correspond to the growth phases of the rabi (winter) and kharif (monsoon) cropping seasons, respectively. The February peak reflects the vigorous development of rabi crops such as wheat and mustard, which benefit from winter precipitation and irrigation. The August peak, the highest of the year, coincides with the monsoon season, during which kharif crops like rice and maize achieve full canopy closure under favorable moisture conditions. The subsequent decline in EVI during September and October indicates crop maturation and harvest, leading to reduced green vegetation cover.

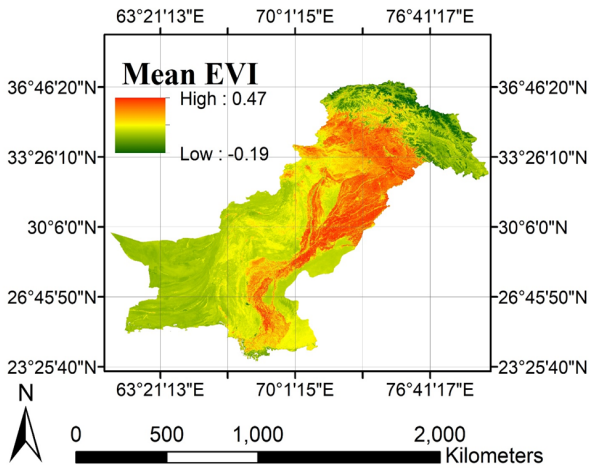

Fig. 2. Mean EVI index values in Pakistan.

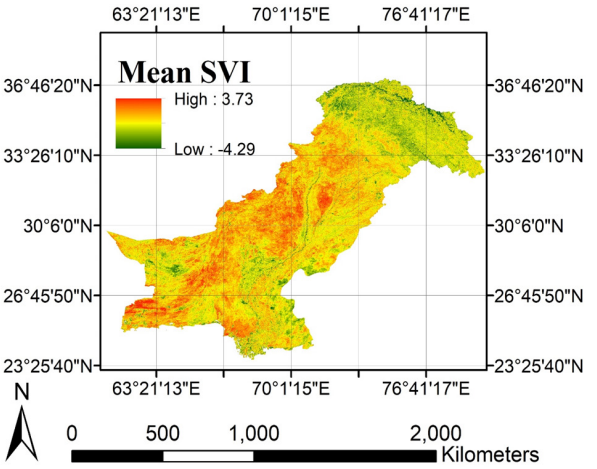

Fig. 3. Mean SVI index values in Pakistan.

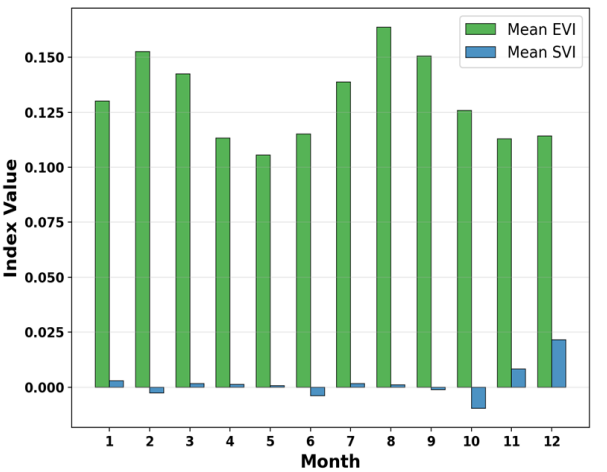

Fig. 4. Mean monthly EVI and SVI dynamics in Pakistan (2001-2022).

In contrast, the SVI remains largely neutral (≈0.00) across most months, suggesting relatively stable. Notably, SVI registers a slight negative value in October (-0.01), likely reflecting post monsoon soil drying following the kharif harvest. However, a modest but meaningful positive shift occurs in November (0.01) and peaks in December (0.02), indicating improved soil moisture conditions coinciding with the sowing and early establishment of rabi crops. This late year rise in SVI may be

attributed to winter rainfall, residual soil moisture retention, or supplemental irrigation, all critical for supporting the rabi cropping cycle in this semi-arid agro climatic zone.

The near zero SVI values observed during the peak EVI months (February and August) suggest that while vegetation is thriving, the soil moisture signal is either masked by dense canopy cover or remains within a balanced range that does not trigger strong positive or negative SVI responses. This underscores the complementary nature of EVI and SVI: while EVI effectively captures vegetation phenology, SVI provides nuanced insights into underlying conditions that support or constrain vegetation growth. Together, these indices confirm the resilience and productivity of Pakistan's agricultural system, which leverages both monsoon rains and winter moisture (natural or managed) to sustain year-round cultivation. The 2001-2022 data thus encapsulate a typical, well-functioning agricultural calendar in Pakistan, characterized by timely transitions between cropping seasons and effective moisture management.

3.2. Temporal Dynamics of Vegetation and Soil Conditions in Pakistan (2001–2022): Insights from EVI and SVI Time Series

The SVI and EVI derived long term monthly time series for Pakistan from 2001 to 2022 provide crucial data on vegetation phenology and soil vegetation interactions (Figure 5). This reflects the region's dominant double cropping system, the EVI time series shows consistent seasonal trends with recurring peaks during the kharif (monsoon) season, particularly in August, and secondary peaks during the rabi (winter) season, primarily in February and March. The primary forces behind these bimodal cycles are monsoon rains (June-September), which support kharif crops like rice and maize, and winter irrigation and rainfall, which support rabi crops like wheat and mustard. It's interesting to note that while EVI values fluctuate from year to year, noteworthy increases have been observed recently (e.g., 2019-2022), suggesting higher vegetation production possibly linked to improved irrigation practices, crop management, or favorable climatic conditions.

In contrast, the SVI time series displays more dynamic and variable behavior, indicating significant fluctuations over time (Figure 6). The early years (2001-2005) show predominantly negative SVI values (down to –1.18), suggesting dry soil conditions or sparse vegetation cover, a marked shift occurs post 2007, with increasing frequency and magnitude of positive SVI anomalies. The most notable surge occurs around 2020-2022, where SVI reaches values exceeding 1.0, indicating exceptionally favorable soil moisture and vegetation conditions. This upward trend may reflect changes in land use, increased groundwater utilization, climate variability (e.g., higher winter precipitation), or improvements in agricultural infrastructure. However, the high volatility in SVI suggests sensitivity to short term weather events, such as droughts or heavy rainfall, which can rapidly alter soil moisture dynamics and impact crop health.

The mean monthly SVI index values were estimated for Pakistan (Figure 7), This shows

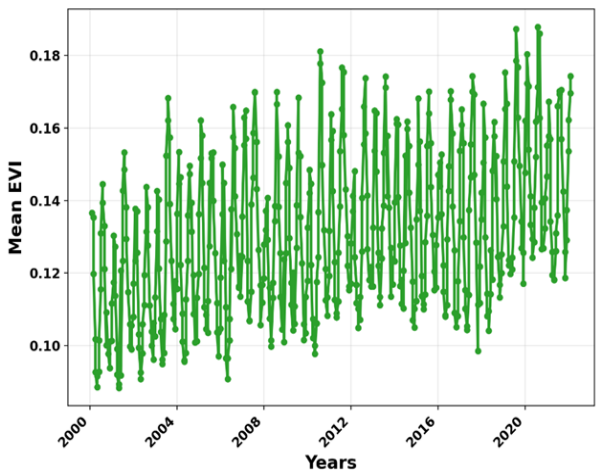

Fig. 5. Monthly time series of EVI.

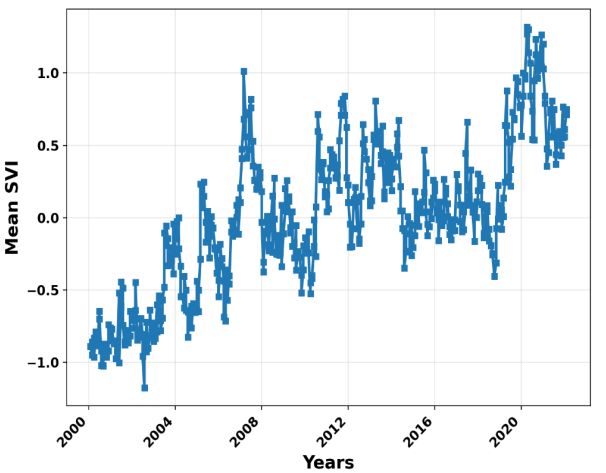

Fig. 6. Monthly time series of SVI.

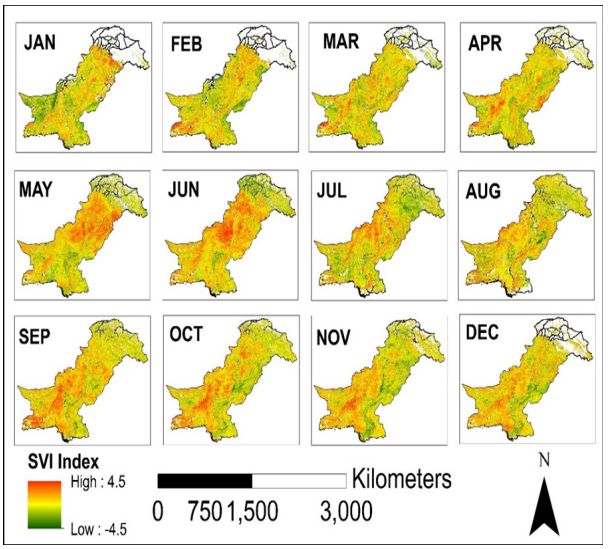

Fig. 7. Mean monthly SVI index values in Pakistan.

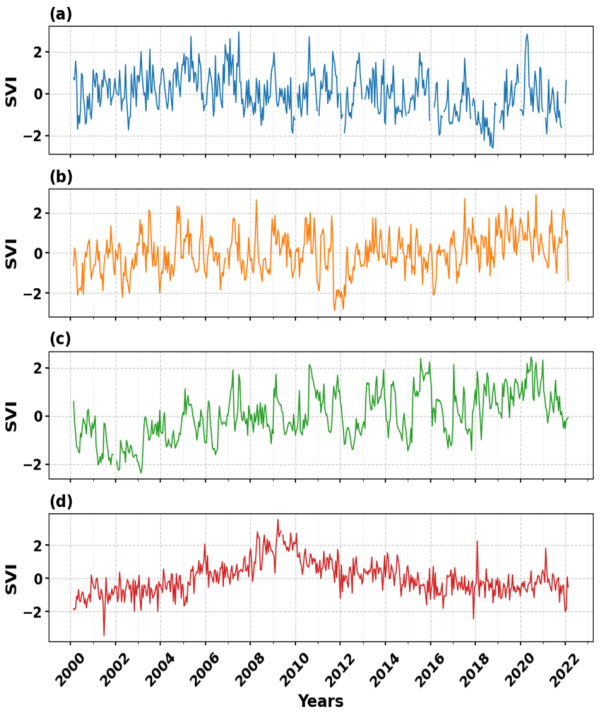

Fig. 8. Time series SVI in provinces of Pakistan: (a) Punjab, (b) Sindh, (c) Khyber Pakhtunkhwa, and (d) Balochistan.

the monthly variation in vegetation stress across Pakistan from January to December. The highest SVI values occur during June–October, corresponding with the monsoon season and peak crop growth, particularly in Punjab and Sindh. In contrast, negative SVI values dominate during the dry winter months (December-February), indicating below average vegetation conditions. This seasonal pattern reflects strong dependence on monsoon rains and agricultural phenology, with central and southern regions showing greater variability due to irrigation and rainfall fluctuations.

Inter annual SVI conditions were observed using time series SVI in Punjab, Sindh, Khyber Pakhtunkhwa, and Balochistan provinces respectively in Figures 8(a to d). The SVI for Punjab shows strong seasonal fluctuations with distinct peaks during the summer months, indicating healthy vegetation growth driven by monsoon rains and agricultural activity (Figures 8(a)). However, the index displays no significant long-term trend and even suggests a slight decline after 2015, potentially reflecting increasing water stress, overuse of resources, or environmental degradation despite high agricultural productivity. In Sindh, the SVI exhibits moderate seasonality and a notable upward trend starting around 2015, signaling improved vegetation conditions over time (Figures 8(b)). This positive shift may be attributed to better irrigation infrastructure, climate variability, or agricultural development, suggesting a recovery from earlier periods of drought and land degradation, particularly observed during 2010-2012 and 2017-2018. Khyber Pakhtunkhwa experiences high variability in SVI, with sharp peaks and frequent negative values, reflecting its mountainous terrain and dependence on seasonal rainfall (Figures 8(c)). The lack of a consistent long-term trend indicates ongoing ecological instability, with vegetation remaining vulnerable to climate extremes and land degradation, highlighting the need for sustainable land and water management practices. Balochistan stands out with a remarkable upward trend in SVI beginning around 2005, transitioning from very low vegetation levels to near normal conditions by 2015 (Figures 8(d)). This significant improvement suggests successful rangeland restoration, afforestation efforts, or increased rainfall, marking one of the most positive environmental developments across Pakistan's provinces in the past two decades.

The SVI provides a powerful metric for assessing vegetation stress and productivity by quantifying deviations of current vegetation conditions from long term climatological norms. Low or negative SVI values typically indicate below average vegetation performance, often linked to water stress, drought, or poor soil

moisture availability, while positive values signify above average vigor, suggesting favorable growing conditions. The magnitude of these anomalies offers insight into the severity of stress or the degree of productivity enhancement. However, interpretation must be contextualized: a negative SVI may reflect natural aridity in rangelands but signal critical stress in irrigated croplands, where even minor moisture deficits can compromise yield. Thus, SVI should not be interpreted in isolation but integrated with land use, crop type, and hydrological data to avoid misclassification of ecological states.

Drought is a pervasive and escalating global phenomenon, characterized by prolonged deficiencies in atmospheric, surface, or subsurface water supplies that persist for months or years [35]. Driven by climate change, population growth, and intensified land use, droughts have become more frequent, severe, and widespread particularly in tropical and subtropical regions such as South Asia. Their impacts include soil retrogression, desertification, reduced agricultural output, ecosystem degradation, increased frequency of wildfires and sandstorms, and heightened socio-economic vulnerabilities [36-38]. As one of the most dangerous climate related hazards, drought directly threatens food security, economic stability, and rural livelihoods [39], making timely monitoring and assessment essential for proactive adaptation and resource allocation [40]. In this context, remote sensing-based drought monitoring has emerged as a scalable and cost-effective tool for tracking spatiotemporal dynamics across vast, data scarce regions like Pakistan.

This study leverages MODIS derived Enhanced Vegetation Index (EVI) and Standardized Vegetation Index (SVI), processed via Google Earth Engine (GEE), to investigate the evolution of vegetation stress and resilience over a 22-year period (2001-2022). GEE enables efficient access to decades of satellite data, facilitates large scale analysis, and supports visualization of spatial trends through maps and time series critical for collaboration among researchers and decision makers [41-43]. Drought assessment is critically important in Pakistan, where arid and semi-arid climates heighten vulnerability to water scarcity, threatening agricultural productivity, economic stability, and social wellbeing [44, 45]. Timely monitoring enables proactive interventions such as deploying drought resistant crops [46], optimizing irrigation, and activating early warning systems to mitigate impacts on vulnerable communities. Integrating remote sensing and machine learning enhances the accuracy and scalability of drought detection, supporting data driven policy and resource allocation [47]. Ultimately, robust drought assessment strengthens climate resilience, safeguards food security, and contributes to poverty reduction and sustainable development across Pakistan's agricultural landscapes. By analyzing EVI and SVI jointly, we move beyond passive observation toward diagnostic assessment: EVI captures absolute biomass and canopy greenness, while SVI reveals whether current vegetation performance deviates significantly positively or negatively from historical baselines [48, 49].

Pakistan's agro ecosystem, dominated by the Indus Basin irrigation network, is particularly vulnerable due to its arid and semi-arid climate, heavy reliance on groundwater, and exposure to monsoon variability. The consistent bimodal pattern in EVI peaking in February-March (rabi season) and August (kharif season) confirms the enduring stability of Pakistan's dual cropping system, sustained by canal irrigation and extensive groundwater extraction [50]. The modest upward trend in EVI since 2018 aligns with documented increases in cropping intensity, adoption of high yielding varieties, and expansion of double cropping into marginal lands, driven by government subsidies, mechanization, and improved seed distribution [51, 52].

However, EVI alone cannot distinguish between sustainable intensification and ecologically unsustainable practices. Here, SVI provides critical diagnostic clarity. The emergence of sustained positive SVI anomalies (> +1.0) after 2007, and their culmination in record high values during 2020-2022 indicates that vegetation performance has consistently exceeded historical expectations over the past 15 years. This shift is not merely recovery from earlier droughts (evident in persistent negative SVI during 2000-2006) [53]. It reflects a systemic transformation in the drivers of vegetation productivity. Three interrelated factors underpin this transition: First, intensified water management driven by proliferation of subsidized tubewells post 2005 has enabled farmers in Punjab (where >90% of irrigation is groundwater dependent) to advance rabi sowing and extend kharif seasons

beyond natural rainfall limits [54, 55]. Yet this intensification comes at the cost of severe aquifer depletion, with the Indus Basin now recognized as one of the world's most overstressed groundwater systems, where extraction exceeds recharge by 100-120% in key districts [56].

Second, improved agronomic practices including zero till drilling, residue retention, and precision fertilizer application have gained traction since 2010 under Climate Smart Agriculture initiatives, enhancing soil moisture retention and reducing evaporation, thereby boosting SVI even under suboptimal rainfall [57]. Third, climatic amelioration has contributed: recent analyses confirm an increase in winter precipitation events linked to shifting mid latitude cyclones and enhanced moisture transport from the Mediterranean and Caspian Sea [58]. Though episodic, their heightened frequency since 2007 has provided critical supplemental recharge during key sowing windows, synergizing with managed irrigation and conservation practices.

Provincial level analysis (Figures 8(a-d)) reveals stark regional contrasts. In Punjab, rising EVI and increasingly positive SVI since 2015 mask alarming groundwater decline and a temporary boost in productivity fueled by non-renewable aquifer drawdown [59]. In Sindh, moderate EVI gains coupled with a clear, accelerating SVI rise since 2015 suggest improved resilience through infrastructure investments canal lining, floodwater harvesting, and distributary rehabilitation reducing conveyance losses without excessive groundwater dependence [60]. Khyber Pakhtunkhwa exhibits high SVI volatility with no long-term trend, reflecting its rain fed, mountainous terrain and vulnerability to erratic precipitation; however, the province's Billion Tree Tsunami afforestation project (2014-2017) the world's largest single region reforestation initiative has significantly restored upland ecosystems, indirectly supporting microclimatic stability and groundwater recharge, though its impact on lowland cropland SVI remains limited [61, 62]. Most notably, Balochistan demonstrates the most dramatic transformation: transitioning from among the lowest SVI values nationally (pre-2005) to consistently positive anomalies by 2015. This recovery correlates strongly with community-based rangeland restoration programs led by the Balochistan Forest and Range Department, supported by FAO, UNDP, and ICARDA, which promoted native species (Prosopis cineraria, Acacia nilotica, Ziziphus mauritiana), contour bunding, water harvesting, and regulated grazing resulting in improved soil moisture, reduced erosion, and increased biomass all achieved without significant groundwater extraction [63]. Balochistan thus offers a replicable model of ecological resilience grounded in ecosystem-based adaptation rather than resource exploitation.

The central insight of this study is that a positive SVI does not equate to sustainability. This reflects relative performance against historical norms, not absolute ecological health. In Pakistan the rising SVI may signal genuine improvement through better water delivery, conservation agriculture, or restoration but it may also mask dangerous tradeoffs as unsustainable groundwater mining, land degradation, chemical overuse, and biodiversity loss.

Punjab and parts of Sindh also experience a more severe self-reinforcing feedback loop: higher SVI → increased farmer confidence → increased tubewell pumping → rapid aquifer depletion → eventual system collapse. Similar patterns have been observed in other areas where satellite derived greening concealed a disastrous groundwater decrease until wells dried up and farming ceased to be profitable [64].

Pakistan now stands at a point, where short term productivity gains are being purchased at the expense of long-term hydrological capital. Relying on SVI alone as a success indicator risks incentivizing practices that maximize yield today at the cost of ruin tomorrow. A farmer achieving an SVI of +1.5 through 50% more groundwater abstraction may reap bumper harvests now but face poverty when the aquifer collapses. Therefore, policy must evolve beyond measuring "performance" to evaluating true resilience: the capacity of the agro ecosystem to maintain productivity under future stress without depleting its natural capital.

While our analysis leverages robust MODIS derived EVI and SVI data processed via Google Earth Engine, several methodological limitations must be acknowledged. First, the 500 m spatial resolution of MODIS aggregates heterogeneous land covers including irrigated fields, fallow land,

urban patches, and degraded rangelands potentially smoothing local anomalies and obscuring field scale dynamics; future studies should integrate higher resolution sensors such as Sentinel 2 or Landsat 8/9 to resolve fine grained heterogeneity [65].

Second, SVI is sensitive to atmospheric aerosols, cloud contamination, and sensor calibration drift, particularly during the monsoon months (July-September), introducing noise and data gaps in peak season estimates; rigorous quality control and temporal gap filling techniques (e.g., harmonic regression) are essential [66]. Third, the absence of a nationwide network of in situ validation sites measuring soil moisture, groundwater levels, and crop yields severely limits causal inference; urgent collaboration between remote sensing teams, universities (e.g., University of Agriculture Faisalabad, National Defence University), and institutions like FAO is needed to establish ground truth stations across agro climatic zones. Fourth, SVI captures vegetation response to moisture with lags of weeks to months, especially for deep rooted crops such as sugarcane or cotton; integrating thermal indices (e.g., Land Surface Temperature, LST; Thermal Condition Index, TCI) could improve detection of immediate soil moisture stress. Fifth, SVI cannot distinguish between cultivated crops, weeds, invasive species, or fallow land a high SVI value in non-agricultural areas may falsely suggest "improvement"; coupling SVI with high resolution land cover classifications (e.g., GlobeLand30) would enhance interpretability. Finally, while we correlate SVI trends with policy interventions (e.g., canal lining, afforestation), we cannot quantify their individual contributions without econometric modeling or farm level surveys; future research must combine remote sensing with participatory rural appraisals and household level water use data to disentangle climate, management, and policy drivers.

This study provides actionable intelligence for designing climate resilient agricultural policies in Pakistan, proposing five evidence-based priorities. First, energy and fertilizer subsidies must be reoriented away from water intensive crops such as rice and sugarcane toward drought tolerant alternatives including millets, sorghum, and chickpeas and scaled up investments in precision irrigation technologies like drip and sprinkler systems, as well as solar powered tubewells to reduce fossil fuel dependence. Evidence from pilot programs in Punjab demonstrates that drip irrigation on wheat can achieve 30-40% water savings without yield loss, yet adoption remains below 5% due to upfront cost barriers [67].

Second, ecosystem-based adaptation (EbA) strategies proven successful in Balochistan such as community managed afforestation using native, drought tolerant species (Prosopis cineraria, Acacia nilotica), contour bunding, check dams, and micro watershed restoration must be replicated nationwide, particularly in Khyber Pakhtunkhwa and southern Punjab. These approaches have demonstrably improved soil organic matter by 22%, reduced runoff by 40%, and increased forage biomass by 60% over five years in Balochistan, offering a low input, high resilience model distinct from groundwater dependent intensification. Third, Pakistan must establish a National Vegetation Anomaly Monitoring System (PVAMS), operationalized through the National Disaster Management Authority (NDMA) and the Ministry of Climate Change, featuring real time dashboards displaying monthly SVI anomalies at the district level, automated alerts triggered when SVI falls below -1.0 for three consecutive months, and linkage to parametric drought insurance schemes that disburse payouts based on index thresholds rather than costly and delayed yield assessments models successfully deployed in India's Agromet Advisory System and Kenya's index based livestock insurance [68].

Fourth, groundwater governance must be modernized using remote sensing as an enforcement tool: areas exhibiting high EVI coupled with rapidly increasing SVI and declining groundwater tables should be designated "critical overdraft zones", where mandatory metering of tubewells and progressive pricing for excessive extraction are enforced mirroring the 35% reduction in groundwater use achieved in Gujarat, India, through satellite guided zoning [69, 70].

Fifth, national investment in data infrastructure and human capacity is critical: training for number of experts, agricultural extension officers to interpret EVI/SVI maps, launching mobile applications delivering localized SVI advisories in Urdu, Pashto, and Balochi, and establishing a centralized, open access national repository of in situ soil

moisture, yield, and groundwater data all integrated with Google Earth Engine would empower farmers and policymakers alike with timely, actionable intelligence. Pakistan's agricultural system is not failing it is adapting, innovating, and, in many places, thriving. The sustained rise in EVI and the dramatic surge in SVI since 2007 stand as testament to the ingenuity of millions of smallholder farmers and decades of public investment in irrigation infrastructure and extension services. But we must ask: at what cost? The most alarming finding of this study is not the absence of progress, but the dangerous illusion of progress. Rising SVI values in Punjab and Sindh may reflect short term gains achieved through the liquidation of Pakistan's most vital natural asset: its groundwater. The same SVI signal that tells us "vegetation is doing better than ever" may also be screaming: "the aquifer is dying". True resilience is not measured by how well crops grow in a good year it is measured by how well the system survives in a bad one. Balochistan teaches us that ecological restoration can build resilience without exploitation. Sindh shows that infrastructure efficiency can decouple productivity from groundwater dependence. Punjab demonstrates the peril of intensification without regulation.

We urge policymakers to shift from reactive crisis response to proactive, data driven governance. The tools exist: MODIS, Google Earth Engine, SVI, and emerging ground networks. The future of Pakistan's food security does not lie in pumping more water it lies in managing less, smarter, and fairer. Continued monitoring of EVI and SVI is not optional, it is foundational. This can be good in management.

4. CONCLUSIONS

This study presents the first long term (2001-2022), province scale assessment of agricultural drought across Pakistan using the Standardized Vegetation Index (SVI) derived from MODIS EVI data processed in Google Earth Engine (GEE). Our analysis reveals distinct regional trajectories: Punjab shows a concerning post 2015 decline in SVI, indicative of mounting water stress despite intensive irrigation; Sindh and Balochistan exhibit significant recovery, likely attributable to improved water infrastructure and large scale afforestation efforts; while Khyber Pakhtunkhwa remains highly volatile, reflecting its rainfall dependent ecosystems. This work advances drought monitoring in semi arid, data scarce regions by introducing an open source, reproducible GEE workflow for operational SVI computation and statistically robust drought classification, the spatiotemporal behavior of SVI corresponds closely with documented drought events and regional patterns of agricultural water stress across Pakistan particularly in major cropping zones such as Punjab and Sindh. This alignment suggests that SVI, derived from satellite based vegetation dynamics, captures signals relevant to agricultural drought conditions beyond purely meteorological indicators like precipitation based indices. The SVI outputs offer practical utility for operational drought monitoring and can inform climate smart agriculture (CSA) decision making including strategic crop planning, irrigation prioritization, and early warning dissemination empowering provincial and national agencies to target interventions, allocate resources efficiently, and strengthen resilience in Pakistan's increasingly climate vulnerable farming systems.

5. ACKNOWLEDGEMENT

We gratefully acknowledge the use of MODIS MOD13Q1 vegetation index data (NASA LP DAAC) and the Google Earth Engine (GEE) platform in this study. The 250 meter resolution satellite observations and GEE's cloud based computational infrastructure were indispensable to our analysis. We extend our sincere appreciation to the developers and maintainers of both MODIS and GEE for providing open, high quality geospatial resources that enabled and enriched this research.

6. CONFLICT OF INTEREST

The authors have declared no conflict of interest.

7. DATA AND CODE AVAILABILITY

All data used are publicly available via Google Earth Engine: MODIS (MOD13Q1 V006) This study follows FAIR (Findable, Accessible, Interoperable, Reusable) principles; code for SVI computation and analysis will be made available upon request to ensure reproducibility and regional adaptation.

8. REFERENCES

1. S.J. Scherr, S. Shames, and R. Friedman. From

climate smart agriculture to climate smart landscapes. *Agriculture & Food Security* 1: 12 (2012).
2. H. Azadi, S.M. Moghaddam, S. Burkart, H. Mahmoudi, S. Van Passel, A. Kurban, and D.L. Carr. Rethinking resilient agriculture: From climate smart agriculture to vulnerable smart agriculture. *Journal of Cleaner Production* 319: 128602 (2021).
3. R. Singh and G.S. Singh. Traditional agriculture: a climate smart approach for sustainable food production. *Energy, Ecology and Environment* 2: 296-316 (2017).
4. K. Chandra, K.E. McNamara, and P. Dargusch. Climate smart agriculture: perspectives and framings. *Climate Policy* 18(4): 526-541 (2018).
5. M. Shelestov, M. Lavreniuk, N. Kussul, A. Novikov, and S. Skakun. Exploring Google Earth Engine platform for big data processing: Classification of multi temporal satellite imagery for crop mapping. *Frontiers in Earth Science* 5: 17 (2017).
6. S.S. Ray, S.M. Neetu, and S. Gupta. Use of remote sensing in crop forecasting and assessment of impact of natural disasters: operational approaches in India. In: Crop Monitoring for Improved Food Security. M.K. Srivastava (Ed.). *Food and Agriculture Organization of the United Nations and the Asian Development Bank, Bangkok* pp. 111 (2015).
7. V.K. Dadhwal, R.P. Singh, S. Dutta, and J.S. Parihar. Remote sensing-based crop inventory: A review of Indian experience. *Tropical Ecology* 43(1): 107-122 (2002).
8. I. Ahmad, A. Ghafoor, M.I. Bhatti, I.U.H. Akhtar, M. Ibrahim, and O. Rehmann. Satellite remote sensing and GIS based crops forecasting & estimation system in Pakistan. In: Crop Monitoring for Improved Food Security. M.K. Srivastava (Ed.). *Food and Agriculture Organization of the United Nations and the Asian Development Bank, Bangkok* pp. 95 (2015).
9. X. Wang, D. P. Lettenmaier, and J. Sheffield. Soil moisture drought in China, 1950–2006. *Journal of Climate* 24(13): 3257-3271 (2011).
10. S. Beguería, S.M.V. Serrano, F. Reig, and B. Latorre. Standardized precipitation evapotranspiration index (SPEI) revisited: parameter fitting, evapotranspiration models, tools, datasets and drought monitoring. *International Journal of Climatology* 34(10): 3001-3023 (2014).
11. J.H. Stagge, L.M. Tallaksen, L. Gudmundsson, A.F. Van Loon, and K. Stahl. Candidate distributions for climatological drought indices (SPI and SPEI). *International Journal of Climatology* 35(13): 4027-4040 (2015).
12. L. Li, D. She, H. Zheng, P. Lin, and Z.L. Yang. Elucidating diverse drought characteristics from two meteorological drought indices (SPI and SPEI) in China. *Journal of Hydrometeorology* 21(7): 1513-1530 (2020).
13. J. Tucker and B.J. Choudhury. Satellite remote sensing of drought conditions. *Remote Sensing of Environment* 23(2): 243-251 (1987).
14. Z. Li, Y. Han, and T. Hao. Assessing the consistency of remotely sensed multiple drought indices for monitoring drought phenomena in continental China. *IEEE Transactions on Geoscience and Remote Sensing* 58(8): 5490-5502 (2020).
15. L. Zhang, W. Jiao, H. Zhang, C. Huang, and Q. Tong. Studying drought phenomena in the Continental United States in 2011 and 2012 using various drought indices. *Remote Sensing of Environment* 190: 96-106 (2017).
16. A. Bégué, D. Arvor, B. Bellon, J. Betbeder, D. De Abelleyra, R.P.D. Ferraz, and S.R. Verón. Remote sensing and cropping practices: A review. *Remote Sensing* 10(1): 99 (2018).
17. Y. Guo, H. Xia, L. Pan, X. Zhao, and R. Li. Mapping the northern limit of double cropping using a phenology-based algorithm and Google Earth Engine. *Remote Sensing* 14(4): 1004 (2022).
18. T. Rotjanakusol and T. Laosuwan. Remote Sensing Based Drought Monitoring in the Middle Part of Northeast Region of Thailand. *Studia Universitatis Vasile Goldis Arad, Seria Stiintele Vietii* 28(1): 14-21 (2018).
19. J. Veneros and L. García. Application of the Standardized Vegetation Index (SVI) and Google Earth Engine (GEE) for Drought Management in Peru. *Tropical and Subtropical Agroecosystems* 25: 27 (2022).
20. S. Sangpradid, Y. Uttaruk, T. Rotjanakusol, and T. Laosuwan. Forecasting Time Series Change of the Average Enhanced Vegetation Index to Monitoring Drought Condition by Using Terra/Modis Data. *Agriculture and Forestry* 67(4): 115-129 (2021).
21. H. Sun, W. Liu, Y. Wang, and S. Yuan. Evaluation of typical spectral vegetation indices for drought monitoring in cropland of the north China plain. *IEEE Journal of Selected Topics in Applied Earth Observations and Remote Sensing* 10(12): 5404-5411 (2017).
22. O. Mikaili and M. Rahimzadegan. Investigating remote sensing indices to monitor drought impacts on a local scale (case study: Fars province, Iran). *Natural Hazards* 111(3): 2511-2529 (2022).

23. S. Ali and M. Imran. The Challenge of Spatial Information Accessibility for Agricultural Policies: Case of Pakistan. *Journal of Regional Socio-Economic Issues* 10(3): 62 (2020).
24. S. Aziz, M. Umar, M. Mansha, M.S. Khan, M.N. Javed, H. Gao, and S. Abdullah. Assessment of drought conditions using HJ 1A/1B data: a case study of Potohar region, Pakistan. *Geomatics, Natural Hazards and Risk* 9(1): 1019-1036 (2018).
25. M.Z. Zakar and R. Zakar. Diffusion of information technology for agricultural development in rural Punjab: Challenges and opportunities. *Pakistan Vision* 9(2): 136-174 (2021).
26. A. Hameed, I.U.H. Padda, and S. Karim. Spatial analysis of food and nutrition security in Pakistan: a holistic pathway towards zero hunger policies. *GeoJournal* 88(6): 2563-2585 (2023).
27. M.A. Imran, A. Ali, M. Ashfaq, S. Hassan, R. Culas, and C. Ma. Impact of Climate Smart Agriculture (CSA) practices on cotton production and livelihood of farmers in Punjab, Pakistan. *Sustainability* 10(6): 2101 (2018).
28. S. Bhandari, S. Phinn, and T. Gill. Assessing viewing and illumination geometry effects on the MODIS vegetation index (MOD13Q1) time series: Implications for monitoring phenology and disturbances in forest communities in Queensland, Australia. *International Journal of Remote Sensing* 32(22): 7513-7538 (2011).
29. S. Testa, E.C.B. Mondino, and C. Pedroli. Correcting MODIS 16-day composite NDVI time-series with actual acquisition dates. *European Journal of Remote Sensing* 47(1): 285-305 (2014).
30. S. Panigrahi, K. Verma, and P. Tripathi. Review of MODIS EVI and NDVI data for data mining applications (Chapter 12). In: Data Deduplication Approaches. T.T. Thwel and G.R. Sinha (Eds.). *Academic Press* pp. 231-253 (2021).
31. X. Peng, X. Zhang, B. Zhang, L. Liu, X. Liu, A.R. Huete, and H. Zhang. Scaling effects on spring phenology detections from MODIS data at multiple spatial resolutions over the contiguous United States. *ISPRS Journal of Photogrammetry and Remote Sensing* 132: 185-198 (2017).
32. L.D. Fiore, G. Piovesan, M. Baliva, and A.D. Filippo. Combined analysis of tree rings and MODIS images to evaluate beech forest productivity along geographic gradients. *EGU General Assembly Conference, Abstracts* pp. 5335 (2020). https://doi.org/10.5194/egusphere-egu2020-5335.
33. T. Phompila, M. Lewis, B. Ostendorf, and K. Clarke. MODIS EVI and LST temporal response for discrimination of tropical land covers. *Remote Sensing* 7(5): 6026-6040 (2015).
34. K.A. Uyeda, D.A. Stow, D.A. Roberts, and P.J. Riggan. Combining ground-based measurements and MODIS-based spectral vegetation indices to track biomass accumulation in post-fire chaparral. *International Journal of Remote Sensing* 38(3): 728-741 (2017).
35. C. Fernando, K.C. Mo, R. Fu, B. Pu, A. Bowerman, B.R. Scanlon, and K. Zhang. What caused the spring intensification and winter demise of the 2011 drought over Texas? *Climate Dynamics* 47: 3077-3090 (2016).
36. R. McLeman, S. Herold, Z. Reljic, M. Sawada, and D. McKenney. GIS based modeling of drought and historical population change on the Canadian Prairies. *Journal of Historical Geography* 36(1): 43-56 (2010).
37. P. Chopra. Drought Risk Assessment Using Remote Sensing and GIS: A Case Study of Gujarat. Master Thesis. *International Institute for Geo-Information Science and Earth Observation, Enschede, The Netherlands* (2006).
38. M.R. Rahman and H. Lateh. Meteorological drought in Bangladesh: assessing, analysing and hazard mapping using SPI, GIS and monthly rainfall data. *Environmental Earth Sciences* 75: 1026 (2016).
39. J. Peters, E.A.W. Shea, L. Ji, A. Vina, M. Hayes, and M.D. Svoboda. Drought monitoring with NDVI based standardized vegetation index. *Photogrammetric Engineering and Remote Sensing* 68(1): 71-75 (2002).
40. C. Pachanaparn, P. Jeefoo and P. Rojanavasu. Application of Remote Sensing for Drought Monitoring with NDVI-based Standardized Vegetation Index in Nan Province, Thailand. *2022 Joint International Conference on Digital Arts, Media and Technology with ECTI Northern Section Conference on Electrical, Electronics, Computer and Telecommunications Engineering (ECTI DAMT & NCON), Chiang Rai, Thailand* pp. 323-328 (2022).
41. S. Aksoy, O. Gorucu, and E. Sertel. Drought monitoring using MODIS derived indices and Google Earth Engine platform. *8th International Conference on Agro Geoinformatics (Agro Geoinformatics) (16th – 19th July 2019), IEEE, Istanbul, Turkey* (2019).
42. O. Mutanga and L. Kumar. Google earth engine applications. *Remote Sensing* 11(5): 591 (2019).
43. E. Roteta, A. Bastarrika, A. Ibisate, and E. Chuvieco. A preliminary global automatic burned

area algorithm at medium resolution in Google Earth Engine. *Remote Sensing* 13(21): 4298 (2021).
44. R. Tabassum, I.A. Khan, and M.H. Arsalan. Monitoring drought events and vegetation conditions in Pakistan: Implications for drought management and food security. *Proceedings of the Pakistan Academy of Sciences* 60(4): 13-28 (2023).
45. S.S. Hassan, M.A. Goheer, H. Farah, F. Hafeez, K. Sheraz, J. Fahad, and A. Tariq. Geospatial assessment of climate variability and drought patterns: a case study from Pakistan. *Theoretical and Applied Climatology* 156(3): 185 (2025).
46. K. Ahmed, G. Shabbir, and M. Ahmed. Exploring drought tolerance for germination traits of diverse wheat genotypes at seedling stage: a multivariate analysis approach. *BMC Plant Biology* 25(1): 390 (2025).
47. Z.M. Yaseen, B. Halder, M.L. Tan, H.C. Kilinc, I. Ahmadianfar, S.I. Abba, K.N.A. Maulud, V. Demir, A.M. Al-Areeq and S. Heddam. Climate change impact analysis on seasonal drought and landforms using meteorological and remote sensing derived indices. *Acta Geophysica* 73: 4849-4881(2025).
48. I. Nazeer. Optimizing Agricultural Inputs and Cropped Area Dynamics: A Decade Long Analysis in Pakistan. *International Journal of Agriculture and Sustainable Development* 6(2): 117-126 (2024).
49. A. Khan, M. Jawad, S. Ali, A. Ali, Z.U.D. Khan, W. Murad, and M.B. Baig. Impact of Climate Change on Biodiversity and Food Security in Khyber Pakhtunkhwa: Challenges, Vulnerabilities, and Strategies for Sustainable Development. In: Food Systems and Biodiversity in the Context of Environmental and Climate Risks: Dynamics and Evolving Solutions. M. Behnassi, M.B. Baig, H. Gupta, R. Sabbahi, G.N. Gill, and M.E. Haiba (Eds.). *Springer Nature Switzerland* pp. 101-140 (2025).
50. S. Ahmad, M. Islam, and S.N. Mirza. Rangeland degradation and management approaches in Balochistan, Pakistan. *Pakistan Journal of Botany* 44: 127-136 (2012).
51. A. Hussain, S. Majeed, A. Hassan, M.A. Khathian, M.Z.U. Khan, I. Raza, and J.K. Bajkani. Adoption and Cost benefit Analysis of Drip Irrigation for Production of High Value Crops in Pakistan. *Proceedings of the Pakistan Academy of Sciences: Part B* 59(1): 57-68 (2022).
52. A. Huete, K. Didan, T. Miura, E.P. Rodriguez, X. Gao, and L.G. Ferreira. Overview of the radiometric and biophysical performance of the MODIS vegetation indices. *Remote Sensing of Environment* 83(1-2): 195-213 (2002).
53. M.A. Watto, A.W. Mugera, R. Kingwell, and M.M. Saqab. Re thinking the unimpeded tube well growth under the depleting groundwater resources in the Punjab, Pakistan. *Hydrogeology Journal* 26(7): 2411-2425 (2018).
54. A.K. Sikka, M.F. Alam, and P. Pavelic. Managing groundwater for building resilience for sustainable agriculture in South Asia. *Irrigation and Drainage* 70(3): 560-573 (2021).
55. M. Aleem, S.N. Khan, M. U. Akbar, A. Arshad, Y. Alsubhi, M. Pandey, A. Nasir, and *et al*. Ten Billion Tree Tsunami Project Reveals Climate Change Mitigation and Precipitation Increase in Khyber Pakhtunkhwa Province, Pakistan. *Earth Systems and Environment* in press (2025). https://doi.org/10.1007/s41748-024-00533-7.
56. C. Srinivasarao, R. Lal, S. Kundu, and P.B. Thakur. Conservation agriculture and soil carbon sequestration. In: Conservation Agriculture. M. Farooq and K.H.M. Siddique (Eds.). *Springer, Cham, Heidelberg, New York, Dordrecht, London* pp. 479- 524 (2014).
57. Z. Wan, P. Wang, and X. Li. Using MODIS land surface temperature and normalized difference vegetation index products for monitoring drought in the southern Great Plains, USA. *International Journal of Remote Sensing* 25(1): 61-72 (2004).
58. A. Abbas, S. Ullah, W. Ullah, C. Zhao, A. Karim, M. Waseem, and *et al*. Characteristics of winter precipitation over Pakistan and possible causes during 1981-2018. *Water* 15(13): 2420 (2023).
59. T.R. Saha, P.K. Shrestha, O. Rakovec, S. Thober, and L. Samaniego. A drought monitoring tool for South Asia. *Environmental Research Letters* 16(5): 054014 (2021).
60. E. Fisher, J. Hellin, H. Greatrex, and N. Jensen. Index insurance and climate risk management: Addressing social equity. *Development Policy Review* 37(5): 581-602 (2019).
61. S.A. Memon, F. Osanami, and T. Kondo. Economic Impact Assessment of the Left Bank Out fall Drainage Project: A Case Study. In: New Challenges Facing Asian Agriculture under Globalisation, Volume II. J. Sulaiman, F.M. Arshad, and M.N. Shamsudin (Eds.) *AgEcon Search* pp. 665-673 (2005).
62. M.A. Kahlown and A. Majeed. Water resources situation in Pakistan: challenges and future strategies. In: Water Resources in the South: Present Scenario and Future Prospects. *Commission on Science and Technology for Sustainable Development in the South (COMSTECH), Islamabad, Pakistan* pp. 21

(2003). https://comsats.org/Publications/Books_SnT_Series/03.%20Water%20Resources%20in%20the%20South%20-%20Present%20Scenario%20and%20Future%20Prospects%20(Nov.%202003).pdf

63. M. Usman, M.U. Qamar, R. Becker, M. Zaman, C. Conrad, and S. Salim. Numerical modelling and remote sensing-based approaches for investigating groundwater dynamics under changing land use and climate in the agricultural region of Pakistan. *Journal of Hydrology* 581: 124408 (2020).
64. T. Tanaka. Groundwater governance in Asia: present state and barriers to implementation of good governance. *Proceedings of the International Association of Hydrological Sciences* 364: 470-474 (2014).
65. R.S.D. Fries, M. Hansen, J.R.G. Townshend, and R. Sohlberg. Global land cover classifications at 8 km spatial resolution: The use of training data derived from Landsat imagery in decision tree classifiers. *International Journal of Remote Sensing* 19(16): 3141-3168 (1998).
66. M. Casazza. Climate Parameter Variability. In: Handbook of Drought and Water Scarcity, (1st Edition). S. Eslamian and F.A. Eslamian (Eds.). *CRC Press, Taylor & Francis Group, Boca Raton, Florida, USA* pp. 65-80 (2017).
67. A.W. Rana and S. Gill. Pakistan: Strategy to promote climate smart agriculture practices. *International Food Policy Research Institute* (2025). https://cgspace.cgiar.org/server/api/core/bitstreams/17bec81f-dbd3-4a2d-b2bb-750a484f93e4/content
68. X. Zhang, M.A. Friedl, C.B. Schaaf, A.H. Strahler, J.C. Hodges, F. Gao, B.C. Reed, and A. Huete. Monitoring vegetation phenology using MODIS. *Remote Sensing of Environment* 84(3): 471-475 (2003).
69. S. Khan and S.H. Maqsoom. Elaborating on the Water Wars: The Politics of a Thirsty World. Roshni *Analysis and Report* (2025). https://papers.ssrn.com/sol3/papers.cfm?abstract_id=5394527.
70. S. Sato. Water security in South Asia: Transboundary water politics between India, Pakistan, and Bangladesh. *Authorea* pp. 1-4 (2024). https://d197for5662m48.cloudfront.net/documents/publicationstatus/229174/preprint_pdf/f790bfc3b5b097e8957dcfc831c26fca.pdf

Proceedings of the Pakistan Academy of Sciences: A Physical and Computational Sciences 62(3): 209-220 (2025)

ISSN (Print): 2518-4245; ISSN (Online): 2518-4253
http://doi.org/10.53560/PPASA(62-3)695

Pakistan Academy of Sciences

Research Article

Assessment of Heavy Metal Contamination and Associated Health Risks in Drugs Administered to Newborns in Iraq

Ban Hussein Ali and Ali Abid Abojassim*

Department of Physics, Faculty of Science, University of Kufa, Al-Najaf, Iraq

Abstract: In this research, heavy metals such as lead (Pb), cadmium (Cd), and chromium (Cr) were determined in two types of drug samples, namely syrups and injections that were administered to newborns in Iraqi hospitals, during 2024. 30 samples of drugs were collected to investigate heavy metals using a Shimadzu AA-7000 atomic absorption spectrometer (AAS). The current study used the US Environmental Protection Agency model to calculate the carcinogen and non-carcinogen risk criteria for heavy metals in all medical samples. The average values of Pb, Cd, and Cr in syrup drug samples were 1.65 ± 0.47 mg/L, 0.34 ± 0.06 mg/L, and 1.17 ± 0.09 mg/L, respectively. For injection drug samples, the corresponding average concentrations were 1.71 ± 0.45 mg/L, 0.45 ± 0.04 mg/L, and 1.26 ± 0.04 mg/L, respectively. All measured values of the concentrations of Pb, Cd, and Cr in syrup drug and injection drug were within international permissible limits; though, some injection samples showed elevated Pb levels. However, the TNCR and TCCR results for all samples were within the globally recommended limits by the US Environmental Protection Agency. Although measured concentrations of Pb, Cd, and Cr were within international permissible limits, carcinogenic and non-carcinogenic risk assessments indicate the need for continued monitoring of neonatal drugs, particularly those with elevated Pb levels.

Keywords: Heavy Metals, Medical Drugs, Health Risks, New-born, Carcinogen.

1. INTRODUCTION

Heavy metals are defined as elements with a density greater than 5 g/cm³ [1]. Heavy metals can be found ubiquitously in the natural realm. Nevertheless, their existence in the environment can be augmented due to human-induced actions. The global community is deeply concerned about the environmental contamination caused by heavy metals [2]. Their toxicity increases, even at low concentrations, due to various activities that pollute the environment, water, and soil, and then living organisms through the food chain, causing the formation of stable and non-degradable toxic compounds in bodies, which leads to the destruction of their vital functions [3]. Heavy metals are essential minerals for human, but in small proportions, depending on the type of metal and the body's need for it, which may be a few milligrams per day, and their increase causes health problems. Among the most important minerals necessary for humans are calcium (Ca), phosphorus (P), iron (Fe), magnesium (Mg), copper (Cu), zinc (Zn), manganese (Mn), iodine (I), sodium (Na), potassium (K), and chlorine (Cl) [4]. On the other hand, there are toxic heavy metals whose presence in the human body poses a risk. These include chromium (Cr), cadmium (Cd), lead (Pb), mercury (Hg), etc. [1]. Numerous independent investigations have raised concerns about the presence of pollutants, including heavy metals, in various drug products specifically formulated for children, especially newborns. The susceptibility to both carcinogenic and non-carcinogenic impacts of excessive exposure to heavy metals is a concern for all individuals; however, infants, toddlers, and children are particularly at risk due to their underdeveloped physiological systems [5, 6].

Although environmental exposure to heavy metals is widely documented, their presence in pharmaceutical products used for newborns is of greater concern. In particular, oral syrups and injectable medications may be direct pathways for heavy metal consumption during treatment [7, 8].

Received: July 2025; Revised: August 2025; Accepted: September 2025
* Corresponding Author: Ali Abid Abojassim <ali.alhameedawi@uokufa.edu.iq>

Heavy metals are harmful because the body does not metabolize them. They accumulate in soft tissues, which may enter newborns through food, water, air, or absorption through the skin [9]. Heavy metal concentrations in drug samples were studied by many scientists worldwide using different technical [10-12]. 30 types of medications used to treat newborns from the most common diseases affecting this category of children in Iraq.

Since no previous studies have assessed heavy metal levels in drugs used by newborns and available in Iraqi hospitals, the current work provides the first baseline data. Therefore, this work aims to determine Pb, Cd, and Cr levels using atomic absorption spectrometry (AA-7000, Shimadzu, Japan) in medical medications available in Iraq. Carcinogen and non-carcinogen risk parameters such as chronic daily intake (CDI), hazard ratio (HQ), chronic risk index (HI), cancer risk (CR), and total cumulative cancer risk (TCCR) were also calculated in all samples of the current study. This study not only addresses a critical public health issue but also provides valuable insights for policymakers and healthcare providers to ensure safer pharmacy practices.

2. MATERIALS AND METHODS

2.1. Drugs Samples

Drug samples in the present work included syrups and injectable drugs that are commonly used and administered to neonates in Iraqi hospitals. Selection criteria were based on their frequency of prescription and availability in neonatal wards, ensuring representativeness of routine clinical practice. Initial quality control properties, such as labeling, packaging, and expiry, were performed. All drug samples were securely packaged to prevent moisture absorption and reduce microbial contamination. To maintain sample integrity, all medications were stored in their original sealed containers under recommended storage conditions (at room temperature and away from direct sunlight) until analysis. These samples were collected from November 01, 2024, to December 01, 2024. The sources of these samples (30 samples) were chosen from various countries and obtained from the Iraqi hospitals. The medical drug samples were divided into 8 syrups and 22 injections at different manufacturing facilities (Table 1).

2.2. Drugs Preparation and Digestion

In the present study, 5-10 ml of the drug samples were taken and put in the digestion vessel, and 5-8 ml of nitric acid (HNO_3 65%) and 1-2 ml of hydrogen peroxide (H_2O_2 30%) were added to speed up the reaction. Then the digestion vessel is placed in the heating device at 180-220 °C for 20-45 minutes. After the reaction is complete, we transfered the resulting solution to a volumetric flask, added distilled water (50 - 100 ml), then employed an atomic absorption device (AAS) [13-16].

To ensure analytical accuracy and precision, three other vials were taken to digest the blank sample, using the same mixture of acids used in the samples, but without adding them to it. These were used to compare the changes between acids in the absence and presence of the sample. The blank sample was used to calibrate the zero to set the spectrophotometer [duha drugs]. Recovery rates ranged within the acceptable limits (80-120%), confirming the reliability of the digestion and measurement procedures.

2.3. Atomic Absorption Spectrometer

Heavy metals (lead, cadmium, and chromium) were analyzed using a flame atomic absorption spectrometer (AA-7000, Japan) model SHIMADZU. Concentrations of lead, cadmium, and chromium are determined using heating. Atomic spectrometers measured at wavelengths of 283.3 nm, 228.8 nm, and 357.9 nm, respectively, and lamp currents of 10 mA, 8 mA, and 10 mA, respectively. The calibration standards of solutions for Pb and Cr were 0.2, 0.5, and 1 ppm, while for Cd were 0.1, 0.5, and 1 ppm. It was calculated that the background level of the blank was 0.01 ppm. Also, the limits of detection for the three heavy metals of the present study were for Pb <0.01, for Cd <0.01, and for Cr 0.09 ppm.

To ensure quality control (QA/QC), the certified reference materials (CRM) of plant origin for metal analysis are also used, and the recovery test is conducted with the best digestion method for each metal. QA/QC procedures included analysis of blanks, duplicates, and spiked samples, and all measurements were performed in triplicate to ensure precision and accuracy.

Table 1. Drug sample information in the present work.

S. No.	Type of drugs	Sample name	Sample code	Origin
1	Syrups	Baby Gas drops 30 ml	SD1	Iraq
2		Paracetamol Syrup	SD2	Iraq
3		Brufemol Syrup	SD3	Iraq
4		Spasmo - drop	SD4	Iraq
5		Butadin Syrup	SD5	Iraq
6		Safaprim Syrup	SD6	Iraq
7		Piodol drop 30 ml	SD7	Iraq
8		Nystatin drops 30 ml	SD8	Iraq
9	Injections	Glucose/ Dextrose 5%	ID1	Iraq
10		Glucose/ Dextrose 10%	ID2	Iraq
11		Difen 10 mg/ml	ID3	Iraq
12		Piodol 10 mg/ml	ID4	Iraq
13		Ciprofloxacin 200 mg/100 ml	ID5	Iraq
14		Ceftriaxone 1mg	ID6	Iraq
15		Meropenem 1000 mg	ID7	Germany
16		Ondansetron 2 mg/ml	ID8	Iraq
17		Piopenem 1000 mg	ID9	Iraq
18		Omnip Aque 350mg/ml	ID10	Ireland
19		TZD Ceftazidime 1000 mg/vail	ID11	India
20		Vancotech 1mg/vial	ID12	India
21		Glucose 50% W/V	ID13	Iraq
22		Flagyl 100 ml	ID14	Iraq
23		Amoxicillin	ID15	Iraq
24		Vanconeer IV	ID16	Iraq
25		Glueose 50% W/V 20 ml	ID17	Germany
26		Tavoctamo piperacillin	ID18	Iraq
27		Potassium chloride 15%	ID19	Iraq
28		Calcium Cluconate 10 ml	ID20	Germany
29		Aminophyline 250 mg/10 ml	ID21	Cyprus
30		Ampicillin 500 ml	ID22	India

2.4. Calculation of Healthy Risk Assessments

The health risk parameters were calculated due to Pb, Cd, and Cr concentrations in drug samples in the present study, which can be classified into two parts (non-carcinogen and carcinogen parameters), as follows:

2.4.1. Non - carcinogen parameters

Three health risk parameters for non-carcinogens were assessed as follows:

a. Chronic daily intake for non-carcinogens (CDI nca) [17]:

$$CDI_{nca}\left(\frac{mg}{kg}.d^{-1}\right) = \frac{Cs \times IR \times EF \times ED \times CF}{BW \times AT(nca)} \quad (1)$$

b. Hazard quotient (HQ) [17]:

$$HQ = \frac{CDI_{nca}}{RFD_O} \quad (2)$$

c. Hazard index (HHI) or total non-carcinogens risk (TNCR) [18, 19]:

$$HI = \sum_1^K \frac{CDI_k}{RFD_k} \quad (3)$$

where Cs is concentrations of Pb, Cd, and Cr concentrations (mg/L), IR is ingestion rate consumption of drugs (1.25 ml/day) for injection [20] and (5.250 ml/day) for syrups [21], EF is exposure frequency (350 day/year) [22], ED is exposure duration (30 years), CF is conversion factor 10^{-6} kg/mg) [17], BW is the average of body weight of newborn (5.7 kg) [23], AT (nca) is the average time for non-carcinogens (365 × 30 days) [22], and RFD_0 is "chronic reference dose of the toxicant" (Pb = 0.004 mg/kg/day, Cd = 0.001 mg/kg/day, and Cr = 0.003 mg/kg/day) [24].

2.4.2. Carcinogen parameters

There are three health risk parameters for carcinogens assessed as follows:

a. Chronic daily intake for carcinogens (CDI_{ca}) [17]:

$$CDI_{ca}\left(\frac{mg}{kg}.d^{-1}\right) = \frac{Cs \times IR \times EF \times ED \times CF}{BW \times AT(na)} \quad (4)$$

b. Cancer risk (CR) [25]:

$$CR = CDI_{ca} \times SF \quad (5)$$

c. Total cumulative cancer risk (TCCR) [18]:

$$TCCR = \sum_1^k CDI_k \times SF_k \quad (6)$$

where, AT (ca) is average time for carcinogens (365×70 days) [22], and SF is "slope factor" (Pb= 0.0085 mg/kg/day, Cd= 6.7 mg/kg/day, and Cr = 0.5 for Pb, Cd, and Cr mg/kg/day) [26].

It should be noted that the selected criteria (IR, EF, ED, and BW) are primarily derived from neonatal studies and EPA guidelines. However, because the EPA equations were originally developed for the general population, their direct application to neonates may raise some concerns; therefore, in this work, we relied on neonatal-specific references whenever possible.

3. RESULTS AND DISCUSSION

Table 2 presents the results of drug samples showing concentrations of Pb, Cd, and Cr. The range value of Pb, Cd, and Cr concentrations (mg/L or ppm) in syrup drug samples were 0.01-3.43, 0.01-0.57, and 0.69-1.62, respectively, with average values of 1.65 ± 0.47, 0.34 ± 0.06, and 1.17 ± 0.09. Whereas, the range values of Pb, Cd, and Cr concentrations (mg/L or ppm) in injection drug samples were 0.001-10.1, 0.13-0.8, and 0.76-1.69, respectively, with average values of 1.71 ± 0.45, 0.45 ± 0.04, and 1.26 ± 0.04. All samples' average Pb, Cd, and Cr concentrations were 1.7 ± 0.35, 0.42 ± 0.03, and 1.23 ± 0.04, respectively. Figure 1 shows the Comparison of the Concentration (mg/L) of Pb, Cd, and Cr in drug samples between the syrups and injections with the safe limit.

Figure 2 shows the percentage values of Pb concentrations in drug samples (syrups and

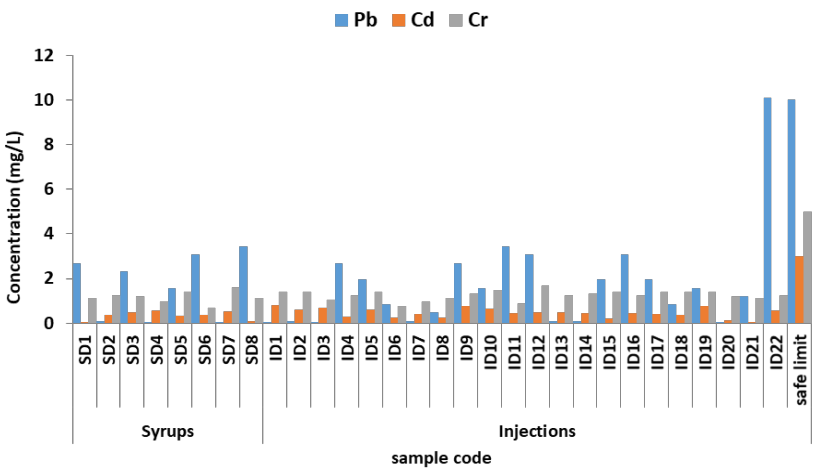

Fig. 1. Comparison of the Concentration (mg/L) of Pb, Cd, and Cr in drugs samples between the syrups and injections with safe limit.

Table 2. Results of heavy metals in drugs sample in the present work.

S. No.	Type of drugs	Sample code	Concentration (mg/L)		
			Pb	**Cd**	**Cr**
1	Syrups	SD1	2.69	0.01	1.12
2		SD2	0.09	0.38	1.26
3		SD3	2.32	0.49	1.19
4		SD4	0.01	0.57	0.98
5		SD5	1.58	0.33	1.40
6		SD6	3.06	0.38	0.69
7		SD7	0.03	0.51	1.62
8		SD8	3.43	0.08	1.12
9	Injections	ID1	0.03	0.80	1.40
10		ID2	0.09	0.60	1.40
11		ID3	0.02	0.69	1.05
12		ID4	2.69	0.28	1.26
13		ID5	1.95	0.60	1.40
14		ID6	0.84	0.26	0.76
15		ID7	0.09	0.40	0.98
16		ID8	0.47	0.24	1.12
17		ID9	2.69	0.76	1.33
18		ID10	1.58	0.64	1.48
19		ID11	3.43	0.44	0.90
20		ID12	3.06	0.48	1.69
21		ID13	0.07	0.48	1.26
22		ID14	0.09	0.44	1.33
23		ID15	1.95	0.22	1.40
24		ID16	3.06	0.44	1.26
25		ID17	1.95	0.40	1.40
26		ID18	0.84	0.37	1.40
27		ID19	1.58	0.76	1.40
28		ID20	0.001	0.13	1.19
29		ID21	1.21	0.01	1.12
30		ID22	10.10	0.55	1.26
Avearge±S.D.(Syrups)			1.65 ± 0.47	0.34 ± 0.06	1.17 ± 0.09
Avearge±S.D.(Injections)			1.71 ± 0.45	0.45 ± 0.04	1.26 ± 0.04
Avearge±S.D.(All)			1.7 ± 0.35	0.42 ± 0.03	1.23 ± 0.04

injections) in the present work. While, Figure 3 shows the percentage values of Cd concentrations in the present samples. Whereas, Figure 4 shows the percentage values of Cr concentrations in the present samples. Figures 2 illustrates that the maximum percentage of Pb concentrations was 17% in ID22 (Ampicillin 500ml, made in India). Figure 5 shows the difference in the average heavy metals in drug samples between syrups and injections. The average of all heavy metals (Pb, Cd, and Cr) in injection samples is higher than in syrup samples. Because when the medicine (needles) is

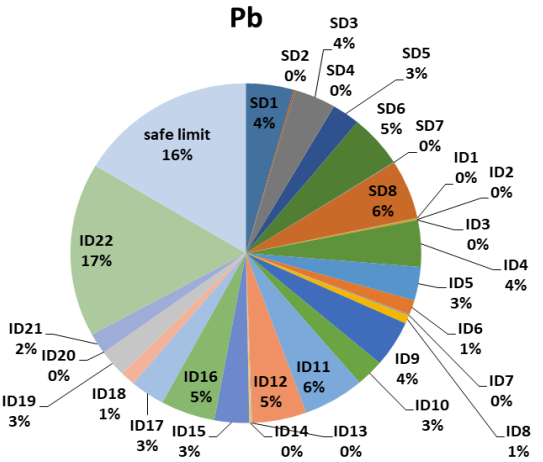

Fig. 2. The percentage value of Lead in drugs samples in the present study.

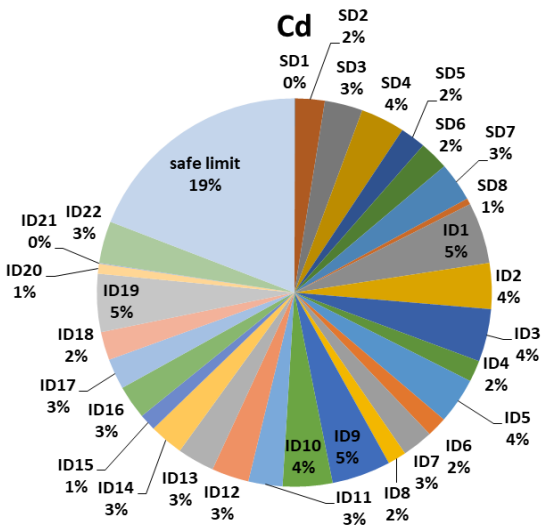

Fig. 3. The percentage value of cadmium in drugs samples in the present study.

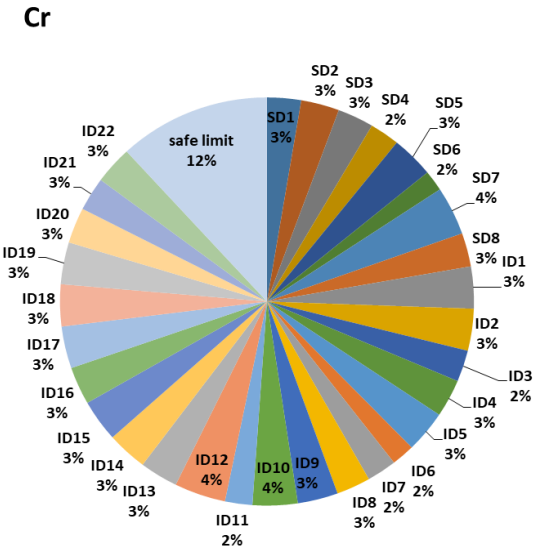

Fig. 4. The percentage value of chromium in drugs samples in the present study.

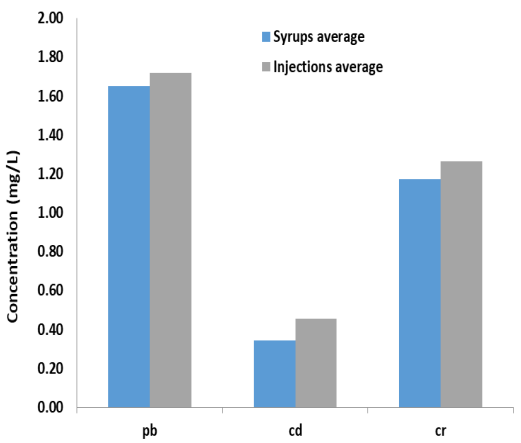

Fig. 5. Comparison of the average of Pb, Cd, and Cr in drugs samples between the syrups and injections.

given intravenously, it immediately reaches the bloodstream, while the medicines (drinks) that are given orally are convenient, safe, and less expensive, as absorption begins from the mouth, stomach, then the small intestine, and the liver proceeds before transporting it through the bloodstream to its location. The injection medicine shows its effectiveness within 5-10 minutes, while the swallowing medicine shows its effectiveness within 45-60 minutes. The study showed that the average lead, cadmium, and chromium for drug samples were within the global limit (Pb = 10 ml/L, Cd = 3 ml/L, and Cr = 5 ml/L) [27]. The Pb detection in injection ID22 at 10.1 mg/L from Table 2 indicates a possible risk from outlier samples. Leaching from packing or equipment, contamination during manufacturing, or inadequate quality control might all be the cause of this abnormally high Pb level. These outliers highlight the necessity of rigorous monitoring, even while the majority of samples fall within safe bounds. To avoid these kinds of incidents, it is crucial to maintain appropriate production and storage conditions. Even while the average Pb levels in each injection are within acceptable bounds, large amounts in specific batches may still be harmful to a newborn's health. To avoid exposure to harmful heavy metals, this emphasises the significance of strict quality control, frequent drug batch monitoring, and adherence to safety protocols.

Table 3 displays the results of non-carcinogen parameters, Chronic Daily Intake (CDInca), Hazard Quotient (HQ), and Hazard Index (HI) for the Pb, Cd, and Cr concentrations in the present study. The average values of CDInca (unit µg/L/day) for Pb, Cd, and Cr concentrations were 0.653 ± 0.159, 0.151 ± 0.024, and 0.470 ± 0.066, respectively. The average values of HQ of Pb, Cd, and Cr concentrations were 0.163 ± 0.039, 0.151 ± 0.024, and 0.156 ± 0.022, respectively. At the same time, as presented in Table 3, the results of HI vary from 0.111 in sample ID20 (Calcium Cluconate 10 ml, Germany) to 1.298 in sample SD3 (Brufemol Syrup, Iraq), with an average of 0.471± 0.065.

The carcinogen parameters, chronic daily intake (CDIca), Carcinogenic Risk (CR), and Total Carcinogenic Risk (TCR) of newborns from

Table 3. Results of non-carcinogen parameters for drug samples in the current study.

S. No.	Sample code	CDI_{nca} (ng/L/day)			HQ×10^{-3}			HI×10^{-3}
		Pb	Cd	Cr	Pb	Cd	Cr	
1	SD1	2.374	0.008	0.988	0.594	0.008	0.329	0.931
2	SD2	0.083	0.340	1.114	0.021	0.340	0.371	0.732
3	SD3	2.047	0.436	1.051	0.512	0.436	0.350	1.298
4	SD4	0.011	0.500	0.862	0.003	0.500	0.287	0.790
5	SD5	1.392	0.292	1.240	0.348	0.292	0.413	1.053
6	SD6	2.701	0.340	0.610	0.675	0.340	0.203	1.218
7	SD7	0.025	0.452	1.429	0.006	0.452	0.476	0.934
8	SD8	3.029	0.068	0.988	0.757	0.068	0.329	1.154
9	ID1	0.005	0.168	0.295	0.001	0.168	0.098	0.268
10	ID2	0.020	0.127	0.295	0.005	0.127	0.098	0.230
11	ID3	0.004	0.146	0.220	0.001	0.146	0.073	0.220
12	ID4	0.565	0.058	0.265	0.141	0.058	0.088	0.288
13	ID5	0.409	0.127	0.295	0.102	0.127	0.098	0.327
14	ID6	0.176	0.054	0.160	0.044	0.054	0.053	0.152
15	ID7	0.020	0.085	0.205	0.005	0.085	0.068	0.158
16	ID8	0.098	0.050	0.235	0.024	0.050	0.078	0.153
17	ID9	0.565	0.161	0.280	0.141	0.161	0.093	0.396
18	ID10	0.332	0.134	0.310	0.083	0.134	0.103	0.320
19	ID11	0.721	0.092	0.190	0.180	0.092	0.063	0.336
20	ID12	0.643	0.100	0.355	0.161	0.100	0.118	0.379
21	ID13	0.015	0.100	0.265	0.004	0.100	0.088	0.192
22	ID14	0.020	0.092	0.280	0.005	0.092	0.093	0.191
23	ID15	0.409	0.047	0.295	0.102	0.047	0.098	0.247
24	ID16	0.643	0.092	0.265	0.161	0.092	0.088	0.341
25	ID17	0.409	0.085	0.295	0.102	0.085	0.098	0.285
26	ID18	0.176	0.077	0.295	0.044	0.077	0.098	0.219
27	ID19	0.332	0.161	0.295	0.083	0.161	0.098	0.342
28	ID20	0.001	0.028	0.250	0.000	0.028	0.083	0.111
29	ID21	0.254	0.003	0.235	0.063	0.003	0.078	0.145
30	ID22	2.124	0.115	0.265	0.531	0.115	0.088	0.734
Avearge±S.D.		0.653 ±0.159	0.151 ±0.024	0.470 ±0.066	0.163 ±0.039	0.151 ±0.024	0.156 ±0.022	0.471 ±0.065

drug samples are given in Table 4. It is observed that the average values of CDIca due to Pb, Cd, and Cr concentrations in unit (µg/L/day) were 0.28 ± 0.068, 0.064 ± 0.010, and 0.201 ± 0.028, respectively. While, the average value of CR was 2.379 ± 0.58 for Pb concentrations, 434.029 ± 69.047 for Cd concentrations, and 100.930 ± 14.162 for Cr concentrations. Also, the results of TCR, as presented in Table 4 ranged from 59.60 in the sample DI21 (Aminophyline 250 mg/10 ml, Cyprus) to 1619.38 in the sample SD4 (Spasmodrop, Iraq), with an average value of 537.34 ± 79.63.

The safe limits of Chronic Daily Intake (CDI) for non-carcinogenic risk (CDI_nC_a) are as follows:

Table 4. Results of carcinogen parameters for drug samples in the current study.

S. No.	Sample code	CDI_{ca} (ng/L/day)			$CR\times10^{-9}$			$TCR\times10^{-9}$
		Pb	Cd	Cr	Pb	Cd	Cr	
1	SD1	1.017	0.004	0.423	8.65	24.35	211.68	244.68
2	SD2	0.036	0.146	0.477	0.30	975.11	238.67	1214.09
3	SD3	0.877	0.187	0.450	7.46	1250.78	225.18	1483.41
4	SD4	0.005	0.214	0.369	0.04	1434.64	184.70	1619.38
5	SD5	0.597	0.125	0.531	5.07	837.40	265.68	1108.16
6	SD6	1.158	0.146	0.261	9.84	975.11	130.70	1115.65
7	SD7	0.011	0.194	0.612	0.09	1296.68	306.16	1602.93
8	SD8	1.298	0.029	0.423	11.03	194.26	211.68	416.98
9	ID1	0.002	0.072	0.127	0.02	483.72	63.26	547.00
10	ID2	0.009	0.054	0.127	0.07	363.44	63.26	426.77
11	ID3	0.002	0.062	0.094	0.01	418.15	47.19	465.35
12	ID4	0.242	0.025	0.114	2.06	166.59	56.83	225.48
13	ID5	0.175	0.054	0.127	1.49	363.44	63.26	428.19
14	ID6	0.075	0.023	0.069	0.64	155.60	34.33	190.58
15	ID7	0.009	0.036	0.088	0.07	243.10	43.98	287.15
16	ID8	0.042	0.022	0.101	0.36	144.68	50.40	195.43
17	ID9	0.242	0.069	0.120	2.06	461.86	60.04	523.96
18	ID10	0.142	0.058	0.133	1.21	385.30	66.47	452.98
19	ID11	0.309	0.040	0.082	2.63	265.02	40.76	308.40
20	ID12	0.276	0.043	0.152	2.34	286.88	76.11	365.33
21	ID13	0.006	0.043	0.114	0.05	286.88	56.83	343.76
22	ID14	0.009	0.040	0.120	0.07	265.02	60.04	325.13
23	ID15	0.175	0.020	0.127	1.49	133.75	63.26	198.49
24	ID16	0.276	0.040	0.114	2.34	265.02	56.83	324.19
25	ID17	0.175	0.036	0.127	1.49	243.10	63.26	307.85
26	ID18	0.075	0.033	0.127	0.64	221.24	63.26	285.14
27	ID19	0.142	0.069	0.127	1.21	461.86	63.26	526.33
28	ID20	0.000	0.012	0.107	0.00	79.04	53.61	132.66
29	ID21	0.109	0.001	0.101	0.92	8.27	50.40	59.60
30	ID22	0.910	0.049	0.114	7.74	330.59	56.83	395.15
Avearge±S.D.		0.28 ±0.068	0.064 ±0.010	0.201 ±0.028	2.379 ±0.58	434.029 ±69.047	100.930 ±14.162	537.34 ±79.63

Pb = 0.004 mg/kg/day, Cd = 0.001 mg/kg/day, and Cr = 0.003 mg/kg/day [24]. Figure 6 compares the CDI_nc_a values for Pb, Cd, and Cr concentrations in all drug samples (syrups and injections) with their respective safe limits. The results indicate that all values are within the safe limits [24]. Similarly, Figure 7 compares the CDI values for carcinogenic risk ($CDIc_a$) in all drug samples under study with the established safe limits, showing that they also fall within acceptable ranges [24].

Also, the values of HQ and HI in the present study samples were smaller than the safe limit of 1, as established globally by the EPA [28]. Figure 8 compares the results of HI with the safe limit. While Figures 9 compare the results of TCR with the safe limit.-On the other hand, the range of safe limits of cancer risk (CR) and total cancer risk (TCR) for heavy metals, according to US EPA reports, was from 10^{-6} to 10^{-4} [29, 30]. From Table 4 it is found that some, such as CR and TCR of risk values, were numerically higher than1000, but they remain within the EPA acceptable range (10^{-6} to 10^{-4}). This indicates that, despite the high values in some samples, the overall carcinogenic risk for newborns from these drugs is considered acceptable.

Statistically, a Pearson Correlation calculates the correlation and p-value between three heavy metals (Pb, Cd, and Cr), these results are given in Table 5, it is noted that the value is not significant. Pearson correlation of Pb, Cd, and Cr, together with the Positive Pearson correlation analysis of Pb with Cd and Cr, drugs can be seen as ores of which one mineral is the host of several elements, including the metals. Positive correlations may imply a similar source of contamination and/or a common absorption and/or accumulation pattern in the newborns, while low or negative correlations may imply independent sources, or differences regarding the absorption, distribution, and metabolism of each of the metals. Familiarity with these trends would facilitate the discernment of possible toxicological implications and quality control.

The results presented in Table 6 show the comparison of the concentrations of Pb, Cd, and Cr in drug samples that were used by children from Iraq and other countries. It is found that Pb concentration was lower than in Turkey and higher than Iran and Bangladesh. While Cd concentration was higher than Bangladesh and lower than Iran and Turkey. Whereas, Cr concentration was higher than Nigeria and Bangladesh, but lower than Turkey.

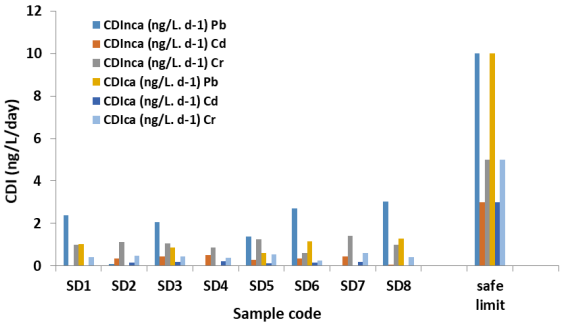

Fig. 6. Comparison of CDI (nca and ca) the samples syrups drugs of the present study and safe limit.

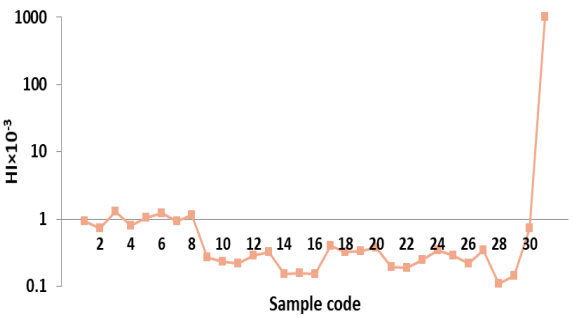

Fig. 8. Comparison of HI in drugs samples between the samples of the present study and safe limit.

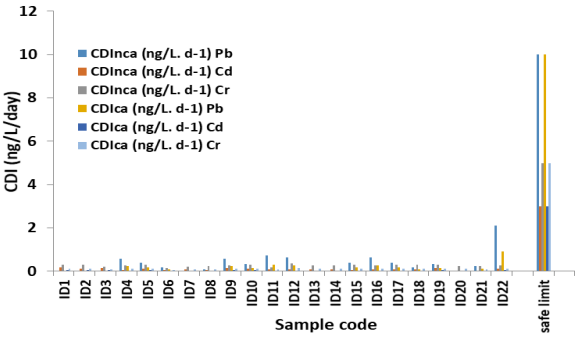

Fig. 7. Comparison of CDI (nca and ca) the samples injections drugs of the present study and safe limit.

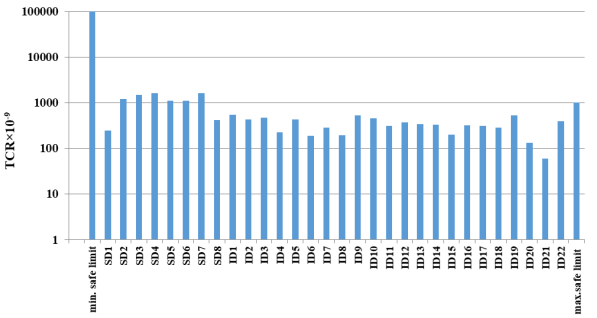

Fig. 9. Comparison of TCR in drugs samples between the samples of the present study and safe limit.

Table 5. Correlation and p-value between Pb, Cd and Cr in all samples in the present study.

Heavy metals		**Pb**	**Cd**	**Cr**
Pb	Correlation	1.00	-0.02924	-0.02644
	p-value	0.5	0 .000490	0.107403
Cd	Correlation	-0.02924	1.00	0.316026
	p-value	0 .000490	0.5	<0 .00001.
Cr	Correlation	-0.02644	0.316026	1.00
	p-value	0.107403	<0 .00001.	0.5

Table 6. Comparison of the average values of heavy metals in pediatric drugs with previous studies from other countries.

	Concentrations (mg/L)			
Country	**Pb**	**Cd**	**Cr**	**Reference**
Iran	1.69	0.89	-----	[31]
Nigeria	-----	-----	0.9	[32]
Turkey	3.4	5	4	[33]
Bangladesh	<0.1	<0.1	0.7	[34]
Iraq	1.7	0.42	1.23	Present study

4. CONCLUSIONS

The present work estimated the concentrations of Pb, Cd, and Cr, and their health risk parameters (non-carcinogenic and carcinogenic) in two types of drugs: syrups and injections used by newborns in Al-Najaf Governorate, Iraq. The concentrations of Pb, Cd, and Cr in all drug samples in the present study were lower than the drug standards set by the U.S. Food and Drug Administration. Also, the results showed that the non-carcinogenic and carcinogenic results were low risk. It can be concluded that most samples of drugs in Al-Najaf Governorate were within the safe limits, but elevated Pb levels in certain injections samples highlight the need for strict quality control and ongoing monitoring.

5. ACKNOWLEDGEMENTS

We are grateful to the University of Kufa and individuals for their invaluable support in completing this work.

6. ETHICAL STATEMENT

The ethical statement is not required as the experiments were conducted on drug samples only.

7. CONFLICT OF INTEREST

There is no conflict of interest.

8. REFERENCES

1. A.A. Abojassim and R.R. Munim. Hazards of heavy metal on human health (Chapter 4). In: Research Trends in Multidisciplinary (vol 14). R. Jayakumar (Ed.). *AkiNik Publications, New Delhi* pp. 195 (2020).
2. V. Saxena. Water quality, air pollution, and climate change: Investigating the environmental impacts of industrialization and urbanization. *Water Air Soil Pollution* 236(2): 73-80 (2025).
3. V. Kumar, A. Sharma, and A. Cerda (Eds.). Heavy Metals in the Environment: Impact, Assessment, and Remediation. *Elsevier, Amsterdam, Netherland* (2020).
4. M. Blackwood (Ed.). Mold, mycotoxins, heavy metals, and parasites in chronic illness. *Independently Published* (2025).
5. E.C. Bair. A narrative review of toxic heavy metal content of infant and toddler foods and evaluation of United States policy. *Frontiers in Nutrition* 9: 919913 (2022).
6. E. Parente. Inorganic Impurities (Elemental

Impurities) Chapter 14. In: Specification of Drug Substances and Products. C.M. Riley, T.W. Rosanske, and G.L. Reid (Eds.). *Elsevier* pp. 439-459 (2025).

7. D. Lledó, G. Grindlay, R. Serrano, L. Gras, and J.M. Sansano. Imidazolium-based task-specific ionic liquid for selective Ag, Cu, Pd and Pt determination by means of dispersive liquid-liquid microextraction and inductively coupled plasma optical emission spectrometry. *Spectrochimica Acta Part B: Atomic Spectroscopy* 204: 106672 (2023).
8. C. Giacomello. Children whose parents use drugs: Promising practices and recommendations. *Council of Europe, Strasbourg, France* (2022). https://rm.coe.int/2021-ppg-27-isbn-children-whose-parents-use-drugs-promising-practices-/1680a602ae
9. P. Nilesh, P. Sandeep, H. Dave. Regulatory Submission Templates for Elemental Impurities, Genotoxic Impurities, and Nitrosamine Impurities of Pharmaceutical Drug Substances. *Asian Journal of Pharmaceutical Research and Health Care* 16(4): 366-377 (2024).
10. D.J. Lawi, W.S. Abdulwhaab, and A.A. Abojassim. Health risk study of heavy metals from consumption of drugs (solid and liquid) samples derived from medicinal plants in Iraq. *Biological Trace Element Research* 201(7): 3528-3540 (2023).
11. Y. Yu, J. Xiang, Z. Meng, K.V. Jarnda, Q. Liu, and P. Ding. Residues of veterinary drugs and heavy metal contamination in livestock and poultry meat from Hunan Province, China. *Food Additives & Contaminants: Part B* 17(4): 360-370 (2024).
12. N.A. Bustami, C.K. Tan, Y.Z. Lee, R. Zaman, Y.B. Ho, and F. Amini. Evaluating Health Risks of Heavy Metals in Chinese Herbal Medicines Used by Pregnant and Postpartum Women in Kuala Lumpur, Malaysia. *Malaysia. EnvironmentAsia* 1: 15-22 (2025).
13. D.A. Skoog, F.J. Holler, and S.R. Crouch (Eds.). Principles of Instrumental Analysis (7th Edition). *Cengage learning*, *United States* (2018).
14. Z.L. He, X.E. Yang, and P.J. Stoffella. Trace elements in agroecosystems and impacts on the environment. *Journal of Trace elements in Medicine and Biology* 19(2-3): 125-140 (2005).
15. D.B. Hibbert (Ed.). Quality Assurance in The Analytical Chemistry Laboratory (1st Edition). *Oxford University Press, New York* (2007).
16. USEPA (United States Environmental Protection Agency). Microwave assisted acid digestion of siliceous and organically based matrices. EPA method 3052, (1996). https://19january2017snapshot.epa.gov/sites/production/files/2015-12/documents/3052.pdf
17. B.H. Ali and A.A. Abojassim. Comparative assessment of heavy metals in breast milk and canned milk consumed by Newborns in Al-Najaf governorate, Iraq. *Comparative Clinical Pathology* in press (2025). https://doi.org/10.1007/s00580-025-03705-7
18. X. Liu, Q. Song, Y. Tang, W. Li, J. Xu, J. Wu, F. Wang and P.C. Brooke. Human Health Risk Assessment of Heavy Metals in the Soil-Vegetable System: A Multi-Medium Analysis. *The Science of the Total Environment* 463-464C: 530–540 (2013).
19. K. Sharafi, M. Yunesian, R.N. Nodehi, A.H. Mahvi, and M. Pirsaheb. A systematic literature review for some toxic metals in widely consumed rice types (domestic and imported) in Iran: Human health risk assessment, uncertainty and sensitivity analysis. *Ecotoxicology and Environmental Safety* 176: 64-75 (2019).
20. Pediatric Associates: Dosage Chart. Online document (2025). https://www.pediatricassociatesnyc.com/dosing-chart
21. A.I. Umar, Y. Sarkingobir, A. Faruk, M. Dikko, and H.W. Adamu. Extent of some heavy metals in cough syrups abused in Sokoto, Nigeria. *Chulalongkorn Medical Journal* 67(4): 251-256 (2024).
22. B.H. Ali and A.A. Abojassim. Health Risks Assessment from Heavy Metals in Care Products Materials for Newborns in Iraq. *International Journal of Environmental Analytical Chemistry* in press (2025). https://doi.org/10.1080/03067319.2025.2463992
23. M. de Onis. The WHO Child Growth Standards (Chapter 4.1). In: Pediatric Nutrition in Practice. B. Koletzko, J. Bhatia, Z.A. Bhutta, P. Cooper, M. Makrides, R. Uauy, and W. Wang (Eds.). *Karger Publishers* pp. 278-294 (2015).
24. U.S. Environmental Protection Agency. Baseline Human Health Risk Assessment for the Standard Mine Site, Gunnison County. Syracuse Research Corporation, Colorado (2008). https://semspub.epa.gov/work/08/1081025.pdf
25. Y. Fakhri, A. Mohseni-Bandpei, G.O. Conti, M. Ferrante, A. Cristaldi, A.K. Jeihooni, M.K. Dehkordi, H. Rasoulzadeh, A. Alinejad, S.M. Mohseni, M. Sarkhosh, H. Keramati, B. Moradi, N. Amanidaz, and Z. Baninameh. Systematic review and health risk assessment of arsenic and lead in the fished shrimps from the Persian Gulf. *Food and Chemical Toxicology* 113: 278-286. (2018).

26. U.S. Environmental Protection Agency. Baseline Human Health Risk Assessment for the Standard Mine Site Gunnison County, Colorado. *Syracuse Research Corporation* (2008). https://archive.epa.gov/hsrb/web/pdf/iris-2003-acrolein.pdf
27. U.S. Food and Drug Administration. FDA's Testing of Cosmetics for Arsenic, Cadmium, Chromium, Cobalt, Lead, Mercury, and Nickel Content. *U.S. Food and Drug Administration* (2022). https://www.fda.gov/cosmetics/potential-contaminants-cosmetics/fdas-testing-cosmetics-arsenic-cadmium-chromium-cobalt-lead-mercury-and-nickel-content
28. United States Environmental Protection Agency. Calculating Upper Confidence Limits for Exposure Point Concentrations at Hazardous Waste Sites. *Office of Emergency and Remedial Response, U.S. Environmental Protection Agency, Washington, DC*, 20460, (2002). https://nepis.epa.gov/Exe/ZyPURL.cgi?Dockey=P100CYCE.TXT
29. R. Kavlock and D. Dix. Computational Toxicology as Implemented by The US EPA: Providing High Throughput Decision Support Tools for Screening and Assessing Chemical Exposure, Hazard and Risk. *Journal of Toxicology and Environmental Health Part B* 13(2-4): 197-217 (2010).
30. United States Environmental Protection Agency. Guidance Manual for Assessing Human Health Risks from Chemically Contaminated Fish and Shellfish. Office of *Water Regulations and Standards (OoWRa), Washington*, *D.C., United States* (1989). https://nepis.epa.gov/Exe/ZyNET.exe/40001CR2.TXT?ZyActionD=ZyDocument&Client=EPA&Index=1986+Thru+1990&Docs=&Query=&Time=&EndTime=&SearchMethod=1&TocRestrict=n&Toc=&TocEntry=&QField=&QFieldYear=&QFieldMonth=&QFieldDay=&IntQFieldOp=0&ExtQFieldOp=0&XmlQuery=&File=D%3A%5Czyfiles%5CIndex%20Data%5C86thru90%5CTxt%5C00000017%5C40001CR2.txt&User=ANONYMOUS&Password=anonymous&SortMethod=h%7C-&MaximumDocuments=1&FuzzyDegree=0&ImageQuality=r75g8/r75g8/x150y150g16/i425&Display=hpfr&DefSeekPage=x&SearchBack=ZyActionL&Back=ZyActionS&BackDesc=Results%20page&MaximumPages=1&ZyEntry=1&SeekPage=x&ZyPURL
31. G.O. Olutona and J. Mulungi. Heavy Metals in Over-the-Counter Pediatric Drugs Locally Produced in Uganda: A Stare at Manganese, Lead, and Cadmium: Heavy metals in OTC pediatric drugs. *Iranian Journal of Pharmaceutical Sciences* 18(3): 235-243 (2022).
32. J.K. Nduka and O.E. Orisakwe. Heavy metal hazards of pediatric syrup administration in Nigeria: a look at chromium, nickel and manganese. *International Journal of Environmental Research and Public Health* 6(7): 1972-1979 (2009).
33. S. Şahin and V.A. Türksoy. The evaluation of potential toxic metal levels of various drugs used in *children. Journal of Health Science and Medical Research* 7(1): 39-46 (2024).
34. M.M. Hossain, S. Nahar, T.R. Choudhury, M. Shahriar, N. Uddin, A.F.M.M. Islam, A. Sarker, and P. Saha. Studies of heavy metal contents and microbial profile in selected pediatric oral liquid preparations available in Bangladesh. *Journal of Pharmaceutical Research International* 21(4):1-15 (2018).

Proceedings of the Pakistan Academy of Sciences: A Physical and Computational Sciences 62(3): 221-233 (2025)

ISSN (Print): 2518-4245; ISSN (Online): 2518-4253
http://doi.org/10.53560/PPASA(62-3)701

Pakistan Academy of Sciences

Research Article

Formaldehyde Pollution in Ahvaz, Iran: Spatiotemporal Trends and Health Risks

Faezeh Borhani[1*], Mohammad Hashemzadeh[1], Samira Andam[2], and Seyed Mohsen Mousavi[3]

[1]Department of Environmental Engineering, Faculty of Civil and Environmental Engineering, Tarbiat Modares University, Tehran 1411713116, Iran

[2]Department of Life Science Engineering, Faculty of New Sciences and Technologies, University of Tehran, Tehran 143951561, Iran

[3]Department of Environmental Planning and Design, Shahid Beheshti University, Tehran 1983969411, Tehran, Iran

Abstract: We present a satellite-driven, four-year assessment of formaldehyde (HCHO) over Ahvaz that quantifies its spatiotemporal variability, meteorological controls, and health risk. Using Sentinel-5P/TROPOMI (2019–2022) together with MERRA-2/GLDAS/AIRS fields, we relate HCHO to co-pollutants (CO, NO_2, SO_2) and meteorology (precipitation, temperature, wind speed, relative humidity, dew point) and map hotspots via IDW; health risks are evaluated with RAIS. HCHO correlates positively with temperature ($r = 0.92$) and negatively with relative humidity ($r = -0.84$) and precipitation ($r = -0.65$); the wind-speed link is moderately positive ($r = 0.46$), with primary co-pollutants are weak (CO: $r \approx 0.08$; NO_2: $r \approx -0.02$). Interannually, 2020 shows the highest HCHO and 2021 the lowest (annual mean ≈8% lower in 2021), with persistent hotspots along the southeastern industrial corridor. IUR-based lifetime inhalation cancer risk peaks in 2020 at ~506 expected excess cases citywide and is lowest in 2021 at ~468. These quantitative results highlight temperature-driven photochemistry and moisture-related removal as key controls on HCHO and motivate strengthened air-quality management to mitigate exposure and protect public health in Ahvaz.

Keywords: Formaldehyde (HCHO), Air Pollutants, Meteorological Conditions, Sentinel-5P, Spatiotemporal, Health Risk Assessment.

1. INTRODUCTION

Ahvaz has been identified as a critical area for air quality research due to its high levels of various pollutants, including Formaldehyde (HCHO), ozone (O_3), nitrogen dioxide (NO_2), and sulfur dioxide (SO_2), and carbon monoxide (CO). The city's geographical and climatic conditions exacerbate pollution levels, leading to severe health impacts among residents. Notably, studies have shown that exposure to these pollutants correlates with increased hospital admissions for cardiovascular diseases and respiratory issues [1-3]. Statistical data indicate that, following Tehran and Isfahan, Ahvaz ranks third in terms of air pollution levels in Iran, and this condition is on a continuous upward trajectory. Consequently, it is essential to examine the trends of air pollutants in Ahvaz city. HCHO represents a significant member of the aldehyde family, prevalent in both indoor and outdoor atmospheric environments. This compound is critical for assessing atmospheric oxidation capacity due to its toxic, irritating, and flammable properties [4, 5]. Epidemiological studies investigating the health impacts of HCHO have led the U.S. National Toxicology Program and the International Agency for Research on Cancer to classify this gas as a potential contributor to leukemia [6]. HCHO is primarily emitted from anthropogenic activities such as vehicular emissions, industrial processes,

Received: June 2025; Revised: August 2025; Accepted: September 2025
* Corresponding Author: Faezeh Borhani <f.borhani@modares.ac.ir>

and the use of certain household products. In urban environments like Ahvaz, traffic-related emissions are significant contributors to ambient HCHO levels. Furthermore, photochemical reactions can lead to secondary formation of HCHO from other pollutants, complicating efforts to manage air quality.

Existing research indicates that meteorological parameters and precursor pollutants substantially influence variations in atmospheric pollutant concentrations, as well as the assessment of associated health risks across different months and seasons [7-9]. Borhani *et al.* [10] conducted a pivotal study investigating the effects of fine particulate matter ($PM_{2.5}$) on air quality and public health in Tehran, Iran, over a ten-year period from 2011 to 2020. The research analyzed $PM_{2.5}$ concentrations, the Air Quality Index (AQI), and hospital admissions associated with chronic obstructive pulmonary disease (COPD) linked to $PM_{2.5}$ exposure. The results revealed that reductions in $PM_{2.5}$ levels can yield significant health benefits. Another study examined both indoor and outdoor concentrations of BTEX compounds in Tehran, emphasizing how building characteristics can influence exposure levels. This research suggests that urban planning and building design could mitigate exposure risks to these toxic pollutants [11]. Dehghani *et al.* [12] conducted an evaluation of HCHO concentrations in the ambient air of Tehran, revealing significant levels that may pose health risks. The results underscore the necessity for immediate interventions to regulate emissions from both industrial and vehicular sources to safeguard public health. Hedayatzadeh and Hassanzadeh [13] examined benzene, toluene, ethylbenzene, and xylene (BTEX) compounds in Ahvaz's urban atmosphere, assessing their prevalence, sources, and health risks. Their study underscored the health threats posed by these VOCs, which contribute to air pollution. The findings emphasizes the need for effective air quality management in urban areas like Ahvaz, highlighting the importance of monitoring BTEX levels to mitigate health risks and guide policy on emissions and traffic.

While the relationship between HCHO and various atmospheric variables has been explored, fewer studies have undertaken a comprehensive assessment that simultaneously considers precursor pollutants and a full suite of meteorological conditions . This is particularly true for specific, under-examined urban hotspots, where such detailed analyses are crucial for developing effective, localized mitigation strategies. Ahvaz, despite its status as one of Iran's most critical air pollution centers, has been notably overlooked in existing research. This study addresses this significant gap by conducting a multi-faceted analysis of HCHO's spatiotemporal behavior in Ahvaz from 2019 to 2022 and systematically correlating it with key atmospheric variables. Building upon this essential groundwork, the paper's primary contribution is the quantification of direct public health consequences using the RAIS framework. This approach not only characterizes the pollutant's dynamics in a high-risk environment but also translates these findings into tangible human health impacts, with results presented at both urban and district scales.

2. MATERIALS AND METHODS

2.1. Study Area

Ahvaz ($31^{\circ}30'N$ and $48^{\circ}65'E$) serves as the capital of Khuzestan province in southwestern Iran, is divided into eight districts (Figure 1 and Table 1). The city is situated on both banks of the Karun River and is characterized by a low range of sandstone hills. Covering an area of 318 square kilometers, Ahvaz ranks among the largest cities in Iran, holding the third position in terms of size, following Tehran and Mashhad. Positioned within the Khuzestan plains, the city is approximately 12 meters above sea level. The average annual precipitation in Ahvaz ranges from 220 to 250 mm, with minimum temperatures recorded at 5

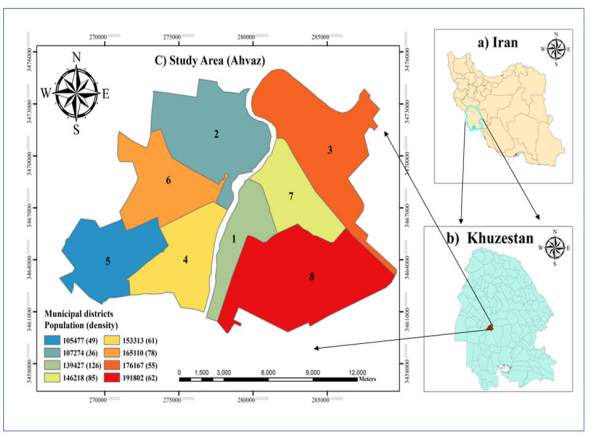

Fig. 1. The location of the study area, (a) Iran, (b) Khuzestan province, (c) Ahvaz city.

Table 1. Population and area of Ahvaz city by Municipal districts.

Municipal districts	Land use	Area (Hectare)	Population (People)	Population density
1	Including the central and historical parts of the city	1103	139427	126
2	Residential and commercial areas with access to urban facilities	2913	107274	36
3	Including industrial and economic areas	3181	176167	55
4	Residential areas with a focus on infrastructure development	2527	153313	61
5	Includes new neighborhoods and housing projects	2155	105477	49
6	Cultural and recreational areas	2111	165110	78
7	Marginal and less developed regions	1719	146218	85
8	Including special areas and large urban projects	3098	191802	62
Total		19494	1184788	

C and maximum temperatures exceeding 40 °C. The average relative humidity typically fluctuates between 14% and 58%, while the average annual wind speed is approximately 38 kilometers per hour. Given its geographical and industrial significance, Ahvaz plays a crucial role in the economic and industrial landscape of the country.

2.2. Datasets and Preparation

2.2.1. Sentinel-5P (TROPOMI) data retrieval and preparation

Spatio-temporal maps of HCHO concentrations and other air pollutants (CO, NO_2, O_3, SO_2) are instrumental in identifying emission hotspots and assessing the effectiveness of pollution mitigation strategies over time. (The units for HCHO, CO, NO_2, and SO_2 are given as vertical column density (VCD) in mol m^{-2}, while O_3 is measured as total column density in Dobson Units (DU). This study analyses the average daily total air pollutants column density obtained from the Sentinel-5P satellite, specifically utilizing the TROPOMI (Tropospheric Monitoring Instrument Sentinel-5 Precursor) HCHO monitoring instrument, accessible through the Google Earth Engine (GEE) cloud platform [14]. We used Level-2 OFFL products and retained only pixels with (qa_value ≥ 0.5.) The data spans from January 1, 2019, to December 31, 2022, covering a four-year period. TROPOMI operates with a spectral resolution ranging from 0.25 to 0.55 nanometre (nm) and provides global daily coverage with a spatial resolution of 5.5 × 3.5 km, (commonly reported as ~3.5 × 5.5 km at nadir). Following the acquisition and importation of the data into Quantum GIS (QGIS), the Inverse Distance Weighting (IDW) method was employed to generate monthly HCHO (total column) maps [15].

In addition, for subsequent health risk assessment (RAIS), HCHO needs to be expressed as volumetric concentration (µg m^{-3}). Therefore, the satellite-retrieved VCD of HCHO (VCD, mol m^{-2}) was converted to volumetric concentration using the following relation:

$$Concentration(original)_{\left(\frac{\mu g}{m^3}\right)} = \frac{C_{\left(\frac{mol}{m^2}\right)} \times Molar\ mass\ \left(\frac{g}{mol}\right)}{H(m)} \times 10^6 \quad (1)$$

Where, C denotes the HCHO ($mol.m^{-2}$) and the molar mass of HCHO is 30.026 $g.mol^{-1}$. In general, the denominator H represents the planetary boundary layer height (PBLH). In this study, for simplicity, we assume H = 1000 (m), which is a reasonable approximation.

2.2.2. Data collection of meteorological parameters using the NASA Giovanni

Meteorological parameter (i.e., total precipitation rate (PR), surface air temperature (T), relative humidity (RH), surface wind speed (WS), dew point temperature (DWP)) data were sourced from the MERRA-2, GLDAS, and AIRS satellite models through the Giovanni platform (Table 2). The Giovanni platform functions as an online interactive geographic visualization tool, facilitated by NASA's Goddard Earth Science Data and Information Service (GES DISC) [16, 17].

Table 2. Summary of meteorological parameters used in this study.

No.	Parameter	Unit	Source	Temporal Resolution	Spatial Resolution	Begin Date	End Date	Abbreviation Name
1	Total precipitation rate	$\frac{kgr}{m^2 s}$	GLDAS Model	Monthly	1°×1°	01/01/2000	31/12/2023	GLDAS_NOAH10_M v2.1
2	Surface air temperature	K	MERRA-2 Reanalysis	Monthly	0.5°×0.625°	01/01/1980	29/02/2024	M2TMNXFLX v5.12.4
3	Relative Humidity at Surface (Daytime/Ascending, AIRS-only)	Percent (%)	AIRS	Monthly	1°×1°	01/09/2002	29/02/2024	AIRS3STM v7.0
4	Surface wind speed	$\frac{m}{s}$	MERRA-2 Reanalysis	Monthly	0.5°×0.625°	01/01/1980	29/02/2024	M2TMNXFLX v5.12.4
5	2-meter dew point temperature	K	MERRA-2 Reanalysis	Monthly	0.5°×0.625°	01/01/1980	29/02/2024	M2TMNXSLV v5.12.4

MERRA-2: Modern-Era Retrospective Analysis and Research and Application-version 2 product, GLDAS: Global Land Data Assimilation System, AIRS: Atmospheric Infrared Sounder.

2.2.3. Health risk assessment

The RAIS is a comprehensive tool developed under the supervision of the U.S. Department of Energy (DOE) since 1996. It serves as a resource for assessing environmental risks, particularly concerning pollutants like HCHO. The system focuses on various dimensions of exposure, including contact duration, application duration, and contact frequency, which are critical for evaluating how individuals interact with hazardous substances [18]. In RAIS terminology, CDI (Chronic Daily Intake) denotes a dose normalized by body weight and time (typically μg ·kg^{-1}·day^{-1}).

To assess CDI of a pollutant, RAIS utilizes specific formulas based on the type of exposure. The CDI can be calculated in two primary ways: Contact CDI: This is expressed in $\frac{\mu g}{m^3}$ and considers the duration and frequency of exposure (Equation 2). In practice, Eq. (2) provides a time-averaged ambient concentration used later as the concentration term in the IUR-based risk (Eq. 4).

Inhalation CDI: For inhalation exposure, the pollutant concentration in the air is measured in μg/m³. This approach specifically addresses the risks associated with airborne pollutants (Equation 3). In Eq. (3), CDI is a dose-based quantity (mg·kg^{-1}·day^{-1}) that uses breathing rate and body weight.

$$CDI_{(\frac{\mu g}{m^3})} = \frac{C_{(\frac{\mu g}{m^3})} \times ED_{(days)}}{AT_{(days)}} \quad (2)$$

$$CDI_{(\frac{\mu g}{kg-day})} = \frac{C_{(\frac{\mu g}{m^3})} \times ED_{(days)} \times BR_{(\frac{m^3}{day})}}{BW_{(kg)} \times AT_{(days)}} \quad (3)$$

Where, *C* and *ED* are the concentration and exposure duration, *AT* is the average human lifespan (typically considered to be 70 years for cancer risk assessments), *BR* is the breathing rate, and *BW* is the average body weight (often considered to be around 70 kg (approximately 154 lbs) for adults).

2.2.3.1. Cancer risk assessment

Cancer risk assessment involves evaluating the likelihood of developing cancer based on various factors, including exposure to carcinogens. The methodology typically incorporates concepts such as cancer slope factors and respiratory risk units, which are often linear and suggest that there is no safe threshold for exposure-meaning even the lowest concentration of a carcinogen can increase cancer risk.

The following equation is used to calculate the cancer risk associated with exposure to a specific carcinogen.

$$Risk\ (unitless) = CDI\ \left(\frac{\mu g}{m^3}\right) \times IUR\ \left(\frac{\mu g}{m^3}\right)^{-1} \quad (4)$$

$$Risk\ (unitless) = CDI\ \left(\frac{\mu g}{kg.day}\right) \times CSF\ \left(\frac{\mu g}{kg.day}\right)^{-1} \quad (5)$$

The Inhalation Unit Risk (IUR) is a measure of the potency of the carcinogen. It represents the upper-bound probability of an individual developing cancer as a result of continuous exposure to the carcinogen at a concentration of 1 $\frac{\mu g}{m^3}$ in air over a lifetime. The IUR is expressed as the inverse of the concentration $\left(\frac{\mu g}{m^3}\right)^{-1}$. Also, Cancer Slope Factor (CSF) is a toxicological measure that quantifies the risk of cancer associated with exposure to a carcinogen. It is expressed in units of risk per unit of exposure $(\frac{\mu g}{kg.day})^{-1}$. The CSF indicates the increase in cancer risk per unit of CDI and is specific to each carcinogen [19, 20].

2.2.4. Matrix heatmap of data

Heatmaps function as a highly effective visualization instrument that is particularly useful for representing data organized in a matrix format. This technique employs variations in color to illustrate different values within the dataset. In the context of this study, this visualization method was specifically applied to clarify the relationship between concentrations of HCHO, other air pollutants (CO, NO_2, O_3, SO_2) and various meteorological parameters observed from the years 2019 to 2022. The heatmaps utilized in this research were created through the use of the seaborn heatmap functionality available in Python, which relies on the capabilities of the NumPy library to facilitate the data processing and visualization [21].

3. RESULTS AND DISCUSSION

The monthly average of air pollutants concentrations

Table 3. The monthly average HCHO in Ahvaz City (VCD and converted volumetric).

Year		Winter			Spring			Summer			Autumn		
		Jan	**Feb**	**Mar**	**Apr**	**May**	**Jun**	**Jul**	**Aug**	**Sep**	**Oct**	**Nov**	**Dec**
2019	$\frac{mol}{m^2}$	0.00005	0.0001178	0.000104	0.00014	0.000178	0.000226	0.00023	0.000258	0.000193	0.000188	0.000164	0.000087
	$\frac{\mu g}{m^3}$	0.0017612	0.0041484	0.0036634	0.0049174	0.0062616	0.0079538	0.0081077	0.0090884	0.0068093	0.0066223	0.0057635	0.0030646
2020	$\frac{mol}{m^2}$	0.0000886	0.0000868	0.0001208	0.000138	0.000194	0.000206	0.00027	0.000229	0.000263	0.00019	0.000151	0.000083
	$\frac{\mu g}{m^3}$	0.0031209	0.0030575	0.0042552	0.0048434	0.0068336	0.0072588	0.0095213	0.0080813	0.0092479	0.0067101	0.0053309	0.0029237
2021	$\frac{mol}{m^2}$	0.0001243	0.000087	0.0000848	0.000148	0.000203	0.000198	0.000216	0.00023	0.000179	0.00014	0.000144	0.000116
	$\frac{\mu g}{m^3}$	0.0043798	0.0030646	0.0029871	0.0052193	0.0071436	0.0069728	0.0076209	0.0081183	0.00629154	0.0049188	0.0050773	0.0040731
2022	$\frac{mol}{m^2}$	0.000074	0.0000901	0.0000855	0.00012	0.000144	0.000196	0.000246	0.00028	0.000236	0.000184	0.00015	0.000101
	$\frac{\mu g}{m^3}$	0.0026066	0.0031737	0.0030117	0.0042129	0.0050837	0.0069171	0.0086551	0.0098782	0.0083106	0.0064919	0.0052894	0.0035535

and meteorological variables from 2019 to 2022 in Ahvaz city is presented in Appendix, Table A.

3.1. Temporal and Spatial Variation of the HCHO and other Air Pollutants (CO, NO_2, O_3, SO_2)

This study examines the atmospheric pollutants concentrations in Ahvaz city. The measured HCHO concentrations throughout the four-year study period consistently fall below the standard parts per billion (ppb) threshold and remain within acceptable limits across all months (Table 3). Figure 2 shows the spatial distribution of the average annual values of the Sentinel-5P total column density of HCHO ($\frac{mol}{m^2}$) in Ahvaz city from January 1, 2019 to December 31, 2022.

The maximum and minimum monthly average values of total HCHO were recorded in August at 0.000249583 $\frac{mol}{m^2}$ and in January at 0.000084235 $\frac{mol}{m^2}$ respectively (Table 3). Overall, HCHO emissions exhibit seasonal variability, with concentrations generally higher in summer than in winter [22]. In unpolluted outdoor air, HCHO concentrations are typically below 1 ppb, whereas urban environments have reported concentrations ranging from 1 to 25 ppb [23, 24]. This study has indicated that regions 3, 6, 7, and 8 experience the highest levels of HCHO emissions. This situation raises significant public health concerns, necessitating targeted interventions to improve air quality in these areas. The high emissions can be attributed to factors such as urbanization, industrial activities, and traffic density, which are prevalent in these regions (Table 1).

The total CO concentration reached its peak in region 8 during the period from 2019 to 2021, while region 1 exhibited the highest level in 2022 (Figure 3(a-c)). In Ahvaz, the maximum average CO concentration was recorded in August, whereas the minimum was noted in November (Figure 3(d)). The highest average concentration of NO_2 in Ahvaz was recorded in January, while the lowest concentration occurred in April. These findings underscore the significance of seasonal changes on air quality in Ahvaz. The data indicates that both CO and NO_2 levels are influenced by meteorological conditions, traffic patterns, and seasonal activities. The total O_3 concentration is greatest in regions 2,

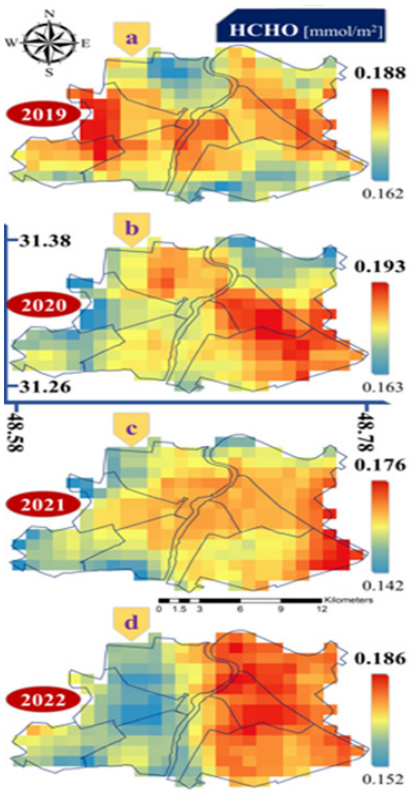

Fig. 2. The spatial distribution of the average annual concentrations of HCHO in Ahvaz, Iran from 2019 to 2022.

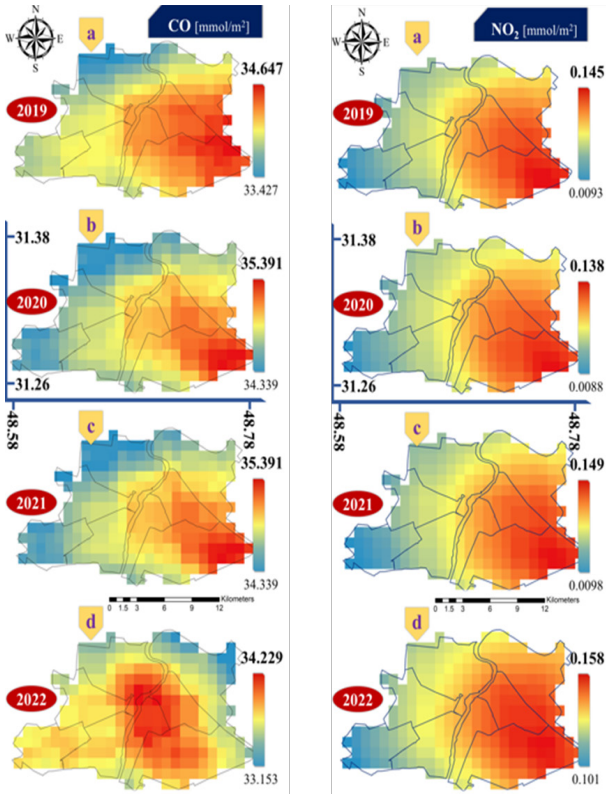

Fig. 3. The spatial distribution of the average annual concentrations of CO and NO_2 in Ahvaz, Iran from 2019 to 2022.

5, and 6, while the highest concentration of SO_2 is observed in region 8 (Figure 4). Figure 4 shows persistent spatial gradients: O_3 remains higher over the northwest–central districts and lower toward the southeast in all four years, with a slight citywide increase from 2019 to 2022. In contrast, SO_2 displays stronger spatial contrasts with recurrent hotspots in the eastern/southeastern industrial corridor (notably region 8) and comparatively lower values in the northwest. Year-to-year variability is larger for SO_2 than for O_3, consistent with episodic emission/stack operations. These patterns suggest regionally driven photochemistry and NO_x titration for O_3, versus more local combustion/industrial sources for SO_2.

3.2. Statistical Associations between HCHO, Meteorology, and Co-Pollutants

Figure 5 summarizes the co-variation between meteorology and pollutants. The HCHO-temperature linkage is very strong (r = 0.92; see also Figure. 6(a)), consistent with temperature-driven VOC emissions, faster photochemistry, and a deeper daytime boundary layer that sustains secondary carbonyl formation; this pattern matches earlier satellite evidence for warm-season enhancement [25, 26]. In contrast, relative humidity shows a pronounced negative association with HCHO (r = -0.84; Figure 6(b)): higher RH generally promotes wet removal/aqueous uptake and reduces actinic flux, both of which diminish HCHO [27]. A similar damping appears for precipitation (PP) (r = -0.65), reflecting washout and cloud shielding [27].

Wind acts in two ways. The HCHO-WS correlation is moderately positive (r = 0.46), implying that stronger winds can deepen/mix the boundary layer and transport VOC-NO_x precursors that maintain secondary HCHO. At the same time, WS-NO_2/SO_2 correlations are negative (-0.35 and -0.70), evidencing efficient dispersion of primary combustion pollutants [28]. The modest/negative HCHO-O_3 correlation (≈ -0.23) is compatible with local NO_x titration of O_3 in traffic-influenced areas, which can decouple O_3 from HCHO despite shared photochemical drivers.

Finally, the small HCHO correlations with CO (0.08) and NO_2 (-0.02) indicate that satellite columns of primary pollutants do not always track a secondary product at monthly scales, owing to differences in sources, chemistry, and mixing height. Overall, temperature favor higher HCHO, whereas humidity and precipitation suppress it, yielding the coherent pattern evident in Figure 5.
For completeness, Figure 6 makes these links explicit in the time domain: Figure 6(a) shows monthly HCHO and surface-air temperature (2019-2022) evolving in phase, with co-located summer maxima (typically July-August) and winter minima

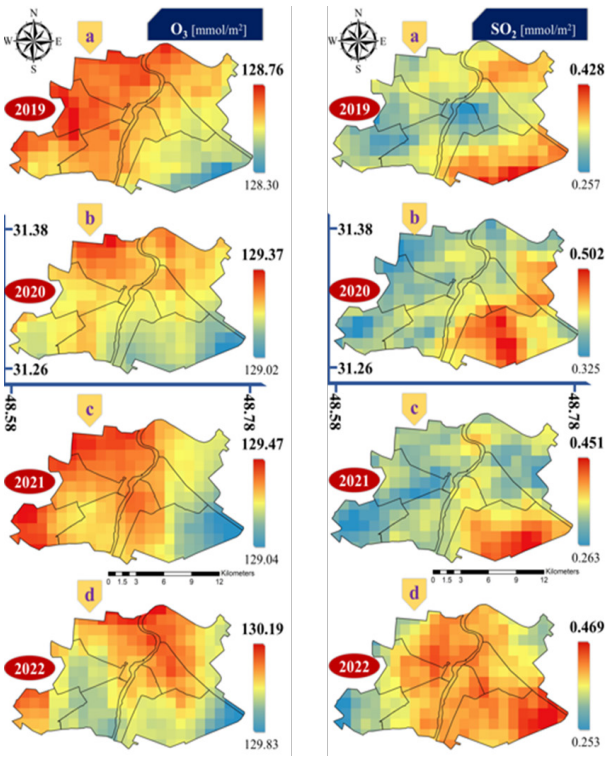

Fig. 4. The spatial distribution of the average annual concentrations of O_3 and SO_2 in Ahvaz, Iran from 2019 to 2022.

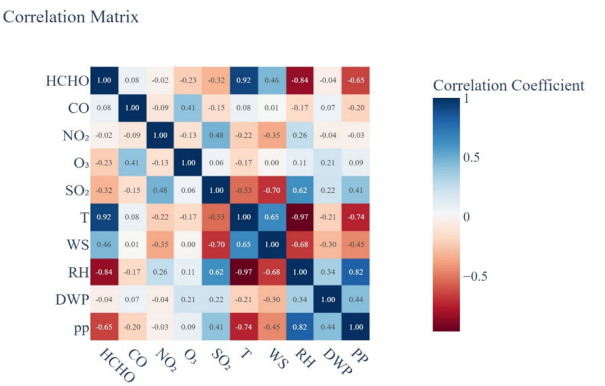

Fig. 5. Heatmap and summary of Spearman's rank coefficient for correlations between monthly average HCHO, other air pollutants (CO, NO_2, O_3, SO_2) and Meteorological parameters (T, WS, RH, DWP, PP) in Ahvaz, Iran, from 2019 to 2022.

(November-January). Figure 6(b) displays the anti-phase behavior with RH, where cool-season humidity peaks and summer troughs mirror the negative correlation noted above. Together, Figures 5 and 6 reinforce that temperature-driven photochemistry and VOC emissions elevate HCHO, while humidity/precipitation primarily act via removal and reduced photolysis.

3.3. Result of Health Risk Assessment

According to the 2015 census data from the Iran Statistics Center, the population of Ahvaz city was 1,184,788 individuals [29]. The values for contact risk and respiratory risk from 2019 to 2022 are presented in Table 4; for context, population-scaled counts (risk × city population) are also reported.

The findings indicate that respiratory risk is consistently ~462 times higher than contact risk across all years, reflecting inhalation as the dominant exposure pathway. Citywide expected cases vary from ~468 (2021) to ~506 (2020), closely tracking the annual mean HCHO (highest in 2020, lowest in 2021). These interannual differences are consistent with the concentration patterns reported in Section 3.2. The reported risks are unitless lifetime cancer probabilities per individual (IUR applied to the annual-mean EC under the assumption of chronic exposure). The accompanying counts represent the expected number of excess cases obtained by scaling the risk by the city population.

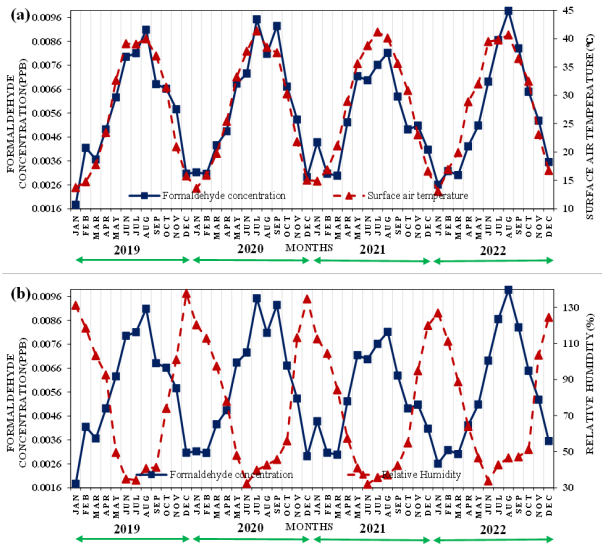

Fig. 6. Comparison of monthly average of HCHO concentrations and (a) Surface air temperature and (b) Relative Humidity, from 2019 to 2022.

4. CONCLUSIONS

This study quantified 2019-2022 spatiotemporal variability of HCHO over Ahvaz using Sentinel-5P/TROPOMI, examined its associations with meteorological drivers (PP, WS, T, RH, DWP) and co-pollutants (CO, NO_2, O_3, SO_2), and evaluated health risks via RAIS.

- We find marked seasonal and spatial variability in HCHO, SO_2, NO_2, O_3, and CO. Temperature shows a strong positive link with HCHO, while relative humidity and precipitation are negatively associated, consistent with enhanced photochemistry at higher T and wet removal/cloud shielding at higher RH/PP; these patterns agree with prior studies [30, 31].
- Spatial contrasts persist across years: O_3 concentrations/columns are generally higher in the western–northwestern districts, whereas SO_2 exhibits recurrent hotspots in Region 8, reflecting localized industrial/combustion influences versus regionally driven photochemistry for O_3.
- Health risk: inhalation (respiratory) lifetime cancer risk clearly exceeds contact risk in all years. The highest respiratory risk occurs in 2020 and the lowest in 2021, mirroring the corresponding annual mean HCHO.

Table 4. Annual risk assessment of HCHO in Ahvaz city from 2019 to 2022.

Year	Total annual concentration	Average annual concentration	Annual contact risk	Annual respiratory risk	Risk person per year (population of Ahvaz 1,184,788)	
					Annual contact risk/population	Annual respiratory risk/population
2019	0.001935	0.00016125	8.861E-07	0.00040897	1.05	484.5
2020	0.0020209	0.00016841	9.254E-07	0.00042711	1.10	506.03
2021	0.0018699	0.00015583	8.5628E-07	0.0003952	1.01	468.23
2022	0.0019073	0.00015894	8.734E-07	0.00040311	1.03	477.6

It is worth noting, these results carry uncertainties arising from satellite retrieval and processing (QA/cloud screening and spatial resolution), the conversion from VCD to volumetric concentration (dependence on boundary-layer height), and toxicity parameters/assumptions in RAIS (IUR/CSF ranges and chronic-exposure assumptions). Accordingly, risk values should be interpreted as indicative magnitudes rather than exact counts. The findings underscore the necessity for effective air quality management and monitoring systems in Ahvaz city. Addressing these pollution challenges is crucial for improving living conditions and safeguarding public health against the backdrop of industrialization and environmental factors.

5. Appendix

Table A presents monthly average of HCHO, other air pollutants (CO, NO_2, O_3, SO_2) and meteorological parameters recorded from 2019 to 2022 in Ahvaz, Iran.

6. ACKNOWLEDGEMENTS

Special thanks are extended to the Remote Sensing Laboratory, Faculty of Civil and Environmental Engineering, Tarbiat Modares University, Iran, for their effective assistance in providing the database for this study.

7. ETHICAL STATEMENT

The authors declare that they agree with the publication of this paper in this journal.

8. CONFLICT OF INTEREST

The authors declare that they have no known competing financial interests or personal relationships that could have appeared to influence the work reported in this paper.

9. REFERENCES

1. A. Bhatnagar. Environmental cardiology: studying mechanistic links between pollution and heart disease. *Circulation Research* 99(7): 692-705 (2006).
2. Y. Zhang, Y. Yang, X. He, P. Yang, T. Zong, P. Sun, R. Sun, T. Yu, and Z. Jiang. The cellular function and molecular mechanism of formaldehyde in cardiovascular disease and heart development. *Journal of Cellular and Molecular Medicine* 25(12): 5358-5371 (2021).
3. S.H. Borsi, G. Goudarzi, G. Sarizadeh, M. Dastoorpoor, S. Geravandi, H.A. Shahriyari, Z.A. Mohammadi, and M.J. Mohammadi. Health endpoint of exposure to criteria air pollutants in ambient air of on a populated in Ahvaz City, Iran. *Frontiers in Public Health* 10: 869656 (2022).
4. C. Hak, I. Pundt, S. Trick, C. Kern, U. Platt, J. Dommen, C. Ordóñez, A.S. Prévôt, W. Junkermann, C. Astorga-Lloréns, and B.R. Larsen. Intercomparison of four different in-situ techniques for ambient formaldehyde measurements in urban air. *Atmospheric Chemistry and Physics* 5(11): 2881-2900 (2005).
5. F.M. Onyije and O.G. Avwioro. Excruciating effect of formaldehyde exposure to students in gross anatomy dissection laboratory. *The International Journal of Occupational and Environmental Medicine* 3(2): 92-95 (2012).
6. Y. Zhang, X. Liu, C. McHale, R. Li, L. Zhang, Y. Wu, X. Ye, X. Yang, and S. Ding. Bone marrow injury induced via oxidative stress in mice by inhalation exposure to formaldehyde. *Plos One* 8(9): e74974 (2013).
7. M. Delikhoon, M. Fazlzadeh, A. Sorooshian, A.N. Baghani, M. Golaki, Q. Ashournejad, and A. Barkhordari. Characteristics and health effects of formaldehyde and acetaldehyde in an urban area in Iran. *Environmental Pollution* 242(Part A): 938-951 (2018).
8. A.H. Khoshakhlagh, M. Mohammadzadeh, P. Sicard, and U. Bamel. Human exposure to formaldehyde and health risk assessment: a 46-year systematic literature review. *Environmental Geochemistry and Health* 46(6): 206 (2024).
9. S.M. Mousavi, N.M. Dinan, S. Ansarifard, G. Darvishi, F. Borhani, and A. Naghibi. Assessing the impact of global carbon dioxide changes on atmospheric fluctuations in Iran through satellite data analysis. *Journal of Water and Climate Change* 15(6): 2774-2791 (2024).
10. F. Borhani, M.S. Motlagh, A.H. Ehsani, and Y. Rashidi. Evaluation of short-lived atmospheric fine particles in Tehran, Iran. *Arabian Journal of Geosciences* 15(16): 1398 (2022).
11. M. Hadei, P.K. Hopke, M. Rafiee, N. Rastkari, M. Yarahmadi, M. Kermani, and A. Shahsavani. Indoor and outdoor concentrations of BTEX and formaldehyde in Tehran, Iran: effects of building characteristics and health risk assessment. *Environmental Science and Pollution Research* 25(27): 27423-27437 (2018).

12. M.H. Dehghani, M. Salari, K. Naddafi, S. Nazmara, E. Ahmadi, and P. Kumar. Evaluation of formaldehyde concentration in the ambient air of a most populated Iranian city, Tehran. *Air Quality, Atmosphere & Health* 10(6): 763-772 (2017).
13. F. Hedayatzade and N. Hassanzadeh. Occurrence, probable source, and health risk assessment of benzene, toluene, ethylbenzene, and xylene compounds in ambient urban atmosphere in Ahvaz, Iran. *Archives of Hygiene Sciences* 9(2): 152-167 (2020).
14. F. Borhani, M.S.Motlagh, A.H. Ehsani, Y. Rashidi, M. Ghahremanloo, M. Amani, and A. Moghimi. Current status and future forecast of short-lived climate-forced ozone in Tehran, Iran, derived from ground-based and satellite observations. *Water, Air, & Soil Pollution* 234(2): 134 (2023).
15. F. Borhani, A.H. Ehsani, S.L. McGuirk, M.S. Motlagh, S.M. Mousavi, Y. Rashidi, and S.M. Mirmazloumi. Examining and predicting the influence of climatic and terrestrial factors on the seasonal distribution of ozone column depth over Tehran province using satellite observations. *Acta Geophysica* 72(2): 1191-1226 (2024).
16. GIOVANNI: NASA's Goddard Earth Sciences Data and Information Services Center. *NASA: Earthdata* (2022). https://giovanni.gsfc.nasa.gov/giovanni/
17. F. Borhani, A.A. Pourezzat, and A.H. Ehsani. Spatial distribution of Particulate Matter in Iran from Internal factors to the role of western adjacent countries from political governance to Environmental Governance. *Earth Systems and Environment* 8(1): 135-164 (2024).
18. F. Borhani and A. Noorpoor. Cancer risk assessment Benzene, Toluene, Ethylbenzene and Xylene (BTEX) in the production of insulation bituminous. *Environmental Energy and Economic Research* 1(3): 311-320 (2017).
19. U.S. EPA. Exposure Factors Handbook (1997, Final Report). *U.S. Environmental Protection Agency, Washington, DC*, EPA/600/P-95/002F a-c, (1997). https://cfpub.epa.gov/ncea/efp/recordisplay.cfm?deid=12464
20. U.S. EPA. Exposure Factors Handbook 2011 Edition (Final Report). *U.S. Environmental Protection Agency, Washington, DC*, EPA/600/R-09/052F, (2011). https://cfpub.epa.gov/ncea/efp/recordisplay.cfm?deid=236252
21. A.H. Sial, S.Y.S. Rashdi, and A.H. Khan. Comparative analysis of data visualization libraries Matplotlib and Seaborn in Python. *International Journal of Advanced Trends in Computer Science and Engineering* 10(1): 277-281 (2021).
22. L.A.J. Bastien, N.J. Brown, and R.A. Harley. Contributions to local-and regional-scale formaldehyde concentrations. *Atmospheric Chemistry and Physics* 19(13): 8363-8381 (2019).
23. G.P. Ayers, R.W. Gillett, H. Granek, C. De Serves, and R.A. Cox. Formaldehyde production in clean marine air. *Geophysical Research Letters* 24(4): 401-404 (1997).
24. K. Müller. Determination of aldehydes and ketones in the atmosphere - A comparative long time study at an urban and a rural site in eastern Germany. *Chemosphere* 35(9): 2093-2106 (1997).
25. Y. Zhang, R. Li, Q. Min, H. Bo, Y. Fu, Y. Wang, and Z. Gao. The controlling factors of atmospheric formaldehyde (HCHO) in Amazon as seen from satellite. *Earth and Space Science* 6(6): 959-971 (2019).
26. T. Liu, Y. Lin, J. Chen, G. Chen, C. Yang, L. Xu, M. Li, X. Fan, Y. Chen, L. Yin, Y. Chen, X. Ji, Z. Lin, F. Zhang, H. Wang, and Y. Hong. Seasonal characteristics of atmospheric formaldehyde (HCHO) in a coastal city of southeast China: Formation mechanism and photochemical effects. *Atmospheric Chemistry and Physics* 2022: 1-28 (2022). https://doi.org/10.5194/acp-2022-292
27. F. Vichi, C. Bassani, A. Ianniello, G. Esposito, M. Montagnoli, and A. Imperiali. Formaldehyde Continuous Monitoring at a Rural Station North of Rome: Appraisal of Local Sources Contribution and Meteorological Drivers. *Atmosphere* 14(12): 1833 (2023).
28. M. Hu, Y. Wang, S. Wang, M. Jiao, G. Huang, and B. Xia. Spatial-temporal heterogeneity of air pollution and its relationship with meteorological factors in the Pearl River Delta, China. *Atmospheric Environment* 254: 118415 (2021).
29. S.K. Kuhpar, G. Janbazghobadi, and S. Motevali. Spatial Analysis of Bioclimatic Vulnerability of heat wave hazard in Ahwaz city Pilot. *Journal of Climate Research* 1400(48): 85-98 (2022).
30. J. Kuttippurath, K. Abbhishek, G.S. Gopikrishnan, and M. Pathak. Investigation of long–term trends and major sources of atmospheric HCHO over India. *Environmental Challenges* 7: 100477 (2022).
31. S. Dhankar and B. Pani. Spatio-temporal analysis of formaldehyde and its association with atmospheric and environmental variables over the Southeast Asian region using satellite data. *Environmental Monitoring and Assessment* 197(2): 185 (2025).

Appendix

Table A. Monthly average of formaldehyde (HCHO), other air pollutants (CO, NO_2, O_3, SO_2) and meteorological parameters recorded from 2019 to 2022 in Ahvaz, Iran.

Year	Month	HCHO ($\frac{mol}{m^2}$)	Other air pollutants				Meteorological Parameters				
			CO ($\frac{mol}{m^2}$)	NO_2 ($\frac{mol}{m^2}$)	O_3 ($\frac{mol}{m^2}$)	SO_2 ($\frac{mol}{m^2}$)	T (°C)	WS ($\frac{m}{s}$)	RH (%)	DWP (°C)	PP ($\frac{kgr}{m^2 s}$)
2019	Jan	0.00005	0.033714	0.00012	0.113483	0.000219	13.7373	5.3063	131.1563	6.5750	0.0258
	Feb	0.0001178	0.035167	0.000184	0.124667	0.00031	14.7604	5.0131	118.5313	5.4111	0.0128
	Mar	0.000104	0.035087	0.000106	0.140444	0.000192	17.7945	5.4235	103.2500	6.6703	0.0264
	Apr	0.0001396	0.036577	0.000129	0.136647	0.000291	23.4250	5.1949	92.6406	10.1673	0.0092
	May	0.0001778	0.035143	0.000121	0.134667	0.000315	32.6782	5.0413	49.5156	10.9966	0.0007
	Jun	0.0002258	0.034067	0.000161	0.128571	0.000301	39.1134	6.3854	34.8828	6.7054	0.0000
	Jul	0.0002302	0.033379	0.000109	0.129361	0.000153	39.0319	7.7749	34.1953	4.0256	0.0001
	Aug	0.000258	0.035539	0.000136	0.129	0.000381	39.9686	5.9878	40.7266	6.1979	0.0000
	Sep	0.0001933	0.032179	0.000117	0.122714	0.000265	36.9697	6.2034	41.2656	2.8213	0.0000
	Oct	0.000188	0.032423	0.000113	0.12273	0.000414	31.4266	4.5068	74.0313	7.8402	0.0154
	Nov	0.0001636	0.033214	0.000165	0.127	0.000536	20.9432	3.5398	101.0938	6.1633	0.0117
	Dec	0.000087	0.0322	0.000149	0.132618	0.000868	15.7801	4.3359	137.7500	7.8929	0.0270
2020	Jan	0.0000886	0.035613	0.000134	0.142514	0.000716	13.6067	4.5294	120.3438	4.6372	0.0145
	Feb	0.0000868	0.035037	0.000113	0.136364	0.000485	15.9229	5.0808	112.8750	4.7152	0.0299
	Mar	0.0001208	0.03644	0.000112	0.138971	0.000497	19.7665	4.9384	97.4688	7.8149	0.0253
	Apr	0.0001375	0.037138	0.000096	0.14	0.000362	25.4150	5.7123	77.8594	9.6308	0.0084
	May	0.000194	0.037371	0.000115	0.130865	0.00031	33.2430	5.5274	47.9297	6.1069	0.0007
	Jun	0.0002061	0.033455	0.000102	0.123714	0.000167	37.7906	7.6587	32.3203	2.1011	0.0000
	Jul	0.0002703	0.034625	0.000114	0.125135	0.000336	41.3702	5.7505	39.6719	6.9508	0.0000
	Aug	0.0002294	0.032375	0.000159	0.123857	0.00026	38.4803	6.7521	42.6563	3.7184	0.0000
	Sep	0.0002625	0.0345	0.000137	0.12325	0.000503	37.5153	4.9809	45.6250	5.0284	0.0001
	Oct	0.0001905	0.035471	0.000152	0.118135	0.000363	30.2534	4.3010	55.9531	-2.4697	0.0000
	Nov	0.0001513	0.033192	0.000117	0.122343	0.000439	21.8479	4.7806	113.1875	9.4163	0.0471
	Dec	0.000083	0.033731	0.000102	0.127486	0.00059	15.0287	4.2652	134.6875	7.3165	0.0211

2021	Jan	0.000124	0.035931	0.000235	0.126784	0.000806	14.8778	4.0707	112.5625	3.2985	0.0042
	Feb	0.000087	0.034407	0.000133	0.128394	0.000475	16.8723	4.6399	104.5000	4.3241	0.0134
	Mar	8.48E-05	0.036633	0.0001	0.132649	0.000196	21.0888	5.3366	84.3438	4.6515	0.0058
	Apr	0.000148	0.0362	0.000112	0.134	0.00031	28.9377	5.2291	57.3828	4.0214	0.0011
	May	0.000203	0.03529	0.000134	0.135973	0.000281	35.6096	5.9196	40.9922	2.5787	0.0006
	Jun	0.000198	0.032452	0.000112	0.128382	0.000229	38.7664	7.7936	31.9453	-1.0558	0.0004
	Jul	0.000216	0.034162	0.000121	0.130595	0.000267	41.1648	6.7086	35.6875	4.6762	0.0003
	Aug	0.00023	0.038242	0.000125	0.130757	0.000321	40.1211	5.4004	37.1172	5.7986	0.0001
	Sep	0.000179	0.034882	0.000129	0.127314	0.000236	35.6297	6.2035	42.2734	1.7389	0.0000
	Oct	0.00014	0.032771	0.000119	0.123081	0.000224	30.8433	5.4585	54.7813	0.1899	0.0008
	Nov	0.000144	0.032618	0.000127	0.127278	0.000436	23.0375	4.5013	94.8594	6.5484	0.0073
	Dec	0.000116	0.033304	0.000127	0.127441	0.000643	16.6429	5.0100	119.9063	5.4328	0.0216
2022	Jan	0.000074	0.033407	0.000159	0.129944	0.00081	13.0508	4.1429	126.9063	2.5020	0.0133
	Feb	9.01E-05	0.033929	0.000167	0.132647	0.00039	16.9183	5.0328	111.2188	3.7435	0.0129
	Mar	8.55E-05	0.035591	0.0001	0.134081	0.000205	19.9233	5.4765	88.7344	1.0220	0.0092
	Apr	0.00012	0.034333	0.000135	0.140571	0.000246	28.8860	4.9800	63.9063	1.1829	0.0059
	May	0.000144	0.033387	0.000101	0.129054	0.000136	31.9898	6.8086	46.5703	0.7040	0.0008
	Jun	0.000196	0.034844	0.000134	0.132471	0.000269	39.4897	6.6747	33.7188	1.0517	0.0001
	Jul	0.000246	0.035677	0.000129	0.131083	0.000299	39.7620	6.4188	42.7578	4.8379	0.0024
	Aug	0.00028	0.035606	0.000149	0.131361	0.00041	40.6584	5.1017	46.5547	7.7839	0.0004
	Sep	0.000236	0.033824	0.000135	0.127306	0.000498	36.4741	4.8781	47.1172	2.8872	0.0000
	Oct	0.000184	0.033367	0.000103	0.121649	0.000497	32.4669	4.2601	51.2188	2.0484	0.0006
	Nov	0.00015	0.02944	0.000141	0.129571	0.000357	23.0908	4.6627	103.4688	8.8915	0.0132
	Dec	0.000101	0.031133	0.000163	0.130686	0.000718	16.7387	4.4562	124.4375	5.9849	0.0220

Proceedings of the Pakistan Academy of Sciences: A Physical and Computational Sciences 62(3): 235-246 (2025)

ISSN (Print): 2518-4245; ISSN (Online): 2518-4253
http://doi.org/10.53560/PPASA(62-3)702

Pakistan Academy of Sciences

Research Article

Synthesis, Characterization, and Adsorptive Performance of Ag-Doped ZnO Nanoparticles for Melanoidin Removal

Mehwish Qaseem[1], Saeed Ahmad[2], Muhammad Yasir Khan[1]*, Muhammad Wasim Akhtar[3], Muhammad Furqan Ali[1], Muhammad Saquib Ali[1], Shakeel Ahmed[1], Shahid Bhutto[4], and Mehwish Altaf[1]

[1]Department of Chemical Engineering, University of Karachi, Karachi, Pakistan
[2]Department of Chemical Skills, Yanbu Technical Institute, Yanbu, Saudi Arabia
[3]Department of Metallurgy & Material Engineering, Mehran University of Engineering and Technology, Jamshoro, Sindh, Pakistan
[4]Centre of Environmental Studies, Pakistan Council of Scientific & Industrial Research (PCSIR), Karachi Complex, Karachi, Pakistan

Abstract: Melanoidin, a complex polymer compound formed through Maillard reactions during fermentation, constitutes a significant fraction of distillery wastewater and cannot be treated using standard treatment methods. Silver doped zinc oxide nanoparticles (AgZnONPs) were synthesized, characterized, and used in this work as potential adsorbent to remediate melanoidin from aqueous solutions. The as-synthesized nanoparticles were evaluated using X-ray diffraction (XRD), UV-visible spectroscopy, field-emission scanning electron microscopy (FE-SEM) with energy-dispersive X-ray spectroscopy (EDX), and Fourier-transform infrared spectroscopy (FTIR). Adsorption experiments were performed under varying operational parameters, including solution pH, mass of adsorbent, initial melanoidin concentration, and time of contact. Under optimal conditions, pH 7, 0.5 g/L adsorbent, 200 mg/L of adsorbate concentration, and 90 min contact duration, a maximum removal efficiency of 92% was achieved. The enhanced adsorption performance aligns with the Langmuir isotherm approach, demonstrating monolayer adsorption with a 50 mg/g maximum adsorption capacity. It adheres to pseudo-second-order kinetics, providing strong evidence of chemisorption with a rate-limiting mechanism and predominant process. These results illustrate the potential of AgZnONPs as a robust and efficient adsorbent material for the treatment of melanoidin-rich distillery effluents.

Keywords: Melanoidin, Silver-doped Zinc Oxide, Adsorption, Nanoparticles, Wastewater Treatment, Kinetic Modelling.

1. INTRODUCTION

Melanoidin molecules pose a challenge to the distillery industry because of their color and complex nature. In addition to its high biological oxygen demand (BOD) and chemical oxygen demand (COD), the alcohol industry faces several challenges, as previously described by Lin *et al*. [1]. Melanoidin molecules produce this color by reacting with sugar polymers and amino acids via the Maillard reaction [2]. The dark brown color of wastewater creates serious problems for carrier water bodies because it reduces the concentration of dissolved oxygen in water [3]. These compounds may also accumulate in aquatic species, potentially affecting their general health, growth, metabolism, and reproduction [4]. When melanoidin-rich wastewater is disposed off on land, it can disturb the nutritional balance and microbial activity, which are essential for plant and soil health, hindering seed germination due to chemical toxicity and decreased soil alkalinity [5].

Received: July 2025; Revised: August 2025; Accepted: September 2025
* Corresponding Author: Muhammad Yasir Khan <myasir@uok.edu.pk>

Conventional treatment techniques, such as biological and chemical methods, are generally ineffective for melanoidin degradation because of their complex molecular structures and high stability [6-7]. Advanced oxidation processes, such as photocatalytic degradation, have demonstrated up to a 90% removal efficiency [8]. However, their large-scale industrial application is hampered by catalyst deactivation, limited activity under visible light, high energy demand, and challenges in catalyst recovery and reuse [9]. Advanced technologies can significantly enhance the physical, chemical, and biological properties of distillery wastewater, including melanoidin degradation [10]. Among the advanced technologies explored, adsorption has emerged as a highly effective and economically viable approach owing to its ease of use, low energy requirements, and capacity to eliminate a variety of organic contaminants, including color-imparting molecules [11]. The use of nanomaterial-based adsorbents has further enhanced the efficacy of the adsorption process because of their variable surface chemical composition, large area of surface and reactivity [12]. Zinc oxide (ZnO) is amongst the mostly utilized metal oxides (MOs) owing to its high surface area, convenient synthesis, cost-effectiveness, and environmental compatibility. Thus, it has been widely considered by researchers seeking exceptional optical, chemical, physical, and electrical properties to enhance manufacturing and technical applications [13]. Abdelfattah and El-Shamy showed that ZnO has superior adsorption, photocatalytic activity under ultraviolet light, and structural stability compared to other MOs, including titanium dioxide (TiO_2) and iron oxide (Fe_2O_3) [14]. Nevertheless, the broad bandgap of ZnO (3.2 eV) hinders its activity under visible light, limiting its practical application in wastewater treatment. To get through these restrictions, doping ZnO with metal ions, especially silver, is a commonly investigated methodology to enhance its optical, electrical, and adsorption qualities [15]. It has been demonstrated that adding Ag increases the surface reactivity and electron mobility, while also tuning the bandgap, both of which are essential for enhancing the photocatalytic and adsorption performances [16]. Prior research has shown that Ag-doped ZnO nanostructures are exceptionally effective in adsorbing and degrading a range of organic contaminants, including pigments, phenolic compounds, and pharmaceutical residues [17-19]. Despite these promising outcomes, few investigations have been conducted on the adsorptive elimination of melanoidin using Ag-doped ZnO nanostructures. Furthermore, published reports lack a thorough examination of crucial parameters like impact of solution pH, and comprehensive kinetic and equilibrium evaluations. These discrepancies highlight the need for systematic research to elucidate the adsorption behavior of AgZnONPs toward melanoidin and to provide a mechanistic understanding that can inform the development of effective treatment plans.

In this study, AgZnONPs were synthesized using a co-precipitation technique, and their adsorption performance was examined in melanoidin solution (MS). Moreover, to gain more insight into the fundamental adsorption principle and processes, adsorption data were simulated and validated using kinetic and isothermal models, as depicted in Figure 1.

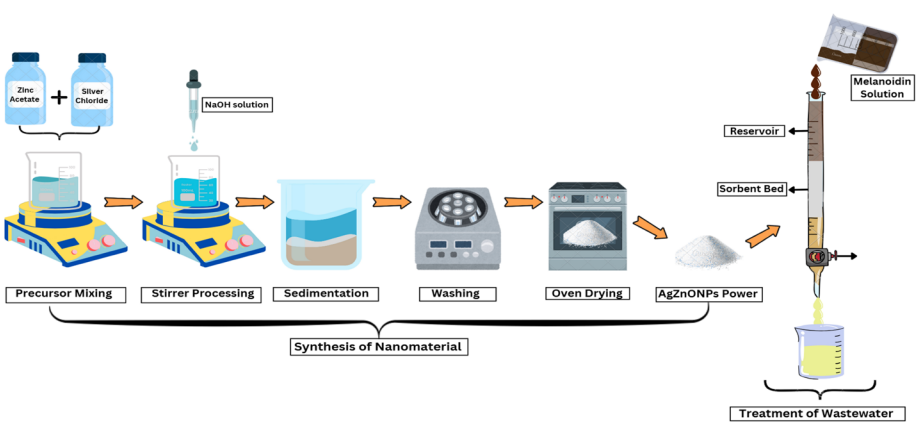

Fig. 1. Overall schematic representation of the synthesis of AgZnONPs and treatment of MS using the adsorption method.

2. MATERIALS AND METHODS

The reagents and chemicals used were extremely pure and of analytical quality. Zinc acetate (Zn $(CH_3CO_2)_2$), methanol (CH_3OH), sodium hydroxide (NaOH), Silver chloride (AgCl), glucose ($C_6H1_2O_6$), glycine ($C_2H_5NO_2$), and sodium bicarbonate ($NaHCO_3$) were bought from Sigma-Aldrich and utilized in their pure states. In this study, various analytical techniques were used to characterize the synthesized AgZnONPs. Crystallinity and phase composition were assessed using a Malvern Panalytical X'Pert3 spectrometer. TESCAN VEGA 4th generation instruments equipped with tungsten filament electron sources and EDS systems were used to examine the morphology and particle size of the AgZnONPs. To study the functional groups and characteristic bonds fourier-transform infrared spectroscopy (FTIR) analysis was executed using IR Prestige 21 (Shimadzu spectrophotometer). UV-visible spectroscopy was performed using a Shimadzu UV-1800 spectrometer.

2.1. Synthesis of Melanoidin Solution

The procedure discussed by Watcharenwong *et al*. [20] was executed to produce synthetic melanoidins. One hundred milliliters of distilled water were used to dissolve the reaction mixture containing 4500 mg of glucose, 1880 mg of glycine, and 420 mg of sodium carbonate. The prepared solution was oven dried for 7 h at 95 °C to promote melanoidin production. The substance was then cooled and freeze-dried for further examination. The molecular weight of the resulting melanoidin was calculated to be between 10,000 and 15,000 Da [21].

2.2. Synthesis of AgZnONPs

AgZnONPs were made via the co-precipitation technique. Zinc acetate was dissolved in 200 mL methanol (0.02 mol/L) and vigorously stirred at 500 rpm for 60 minutes at 55-60 °C. To add silver as a dopant, 17.48 mg of AgCl (1 atomic %) was added to the above solution. The separate solutions were made by mixing (3 g) $NaOH.H_2O$ then added to 50 mL of methanol, and the mixture was stirred for 60 min. Subsequently, 30 mL of NaOH/methanol solution was incorporated dropwise to the zinc acetate/methanol solution and agitated for 40 min. Subsequently, 200 mL of DI water was added to the solution and heated at 85 °C for 1 h with continuous mixing. The synthesized precipitate of AgZnONPs was centrifuged to obtain a colloid and repeatedly washed with methanol at least three times to remove residual oxidants. After centrifugation, the products were oven-dried and crushed in a mortar to obtain the AgZnONP powder. The reaction scheme for AgZnONP synthesis is shown in Figure 2.

2.3. Adsorption Experiments

The melanoidin removal from distillery wastewater was assessed through column adsorption experiments and the efficacy of AgZnONPs as an adsorbent. A column filled with AgZnONPs was used to pass MS at concentrations ranging from 50 to 500 mg/L, with an adsorbent dose from 0.1 to 1 g/L. Controlled flow conditions were employed in the column, and an effluent sample was collected at the outlet. Melanoidin concentrations in both the influent and effluent were measured using UV-UV-visible spectroscopy at a maximum wavelength of 291 nm. The removal percentage of melanoidin was calculated using the standard formula [22].

$$R\% = \frac{C_o - C_t}{C_o} \times 100$$

Where,

C_o is the initial concentration of MS (mg/L) at t = 0

C_t is the concentration of MS (mg/L) at time t (min).

2.4. Isotherms and Kinetics Studies

Kinetic experiments employing pseudo first-order and pseudo second-order models were conducted to elucidate the adsorption behavior of melanoidin on the produced nanoparticles [23]. These two models facilitate the assessment of adsorption rate

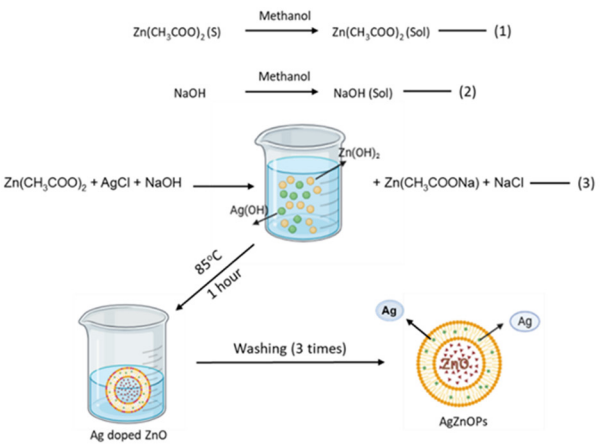

Fig. 2. Reaction scheme of synthesis of AgZnONPs.

and illustrate whether the process is influenced by chemical or physical interactions. Of these two, the model displaying the highest correlation with the experimental data revealed the primary mechanism. Furthermore, the Langmuir and Freundlich models were used in isothermal investigations to assess the adsorption equilibrium [24]. The Freundlich model takes multilayer adsorption on heterogeneous surfaces into account, while the Langmuir model assumes monolayer adsorption on a homogeneous surface. The adsorption mechanism, surface characteristics of the adsorbent, and process efficiency could be better understood when the data were fitted to these models.

3. RESULTS AND DISCUSSION

3.1. Structural Evaluation of AgZnONPs

The stimulated AgZnONPs were inspected using different analytical techniques. By using X-ray diffraction (XRD) analysis, the nanoparticles' crystalline structure and phase integrating were verified. while the FTIR spectra revealed the characteristic vibrations of both doped and undoped Zn-O bonds. Additionally, the SEM images showed particle size dispersion and morphology. Optical studies were performed using a UV-Vis spectrophotometer.

3.1.1. SEM analysis of AgZnONPs

SEM analysis was carried out to examine the structural traits and morphological characteristics of the synthesized AgZnONPs. Figure 3(a) shows that the cylindrical structures were shaped, confirming the presence of nanoparticles. In Figure 3(b), a similar view of the AgZnONPs is presented at a magnification of 25 K, providing a more detailed structural view than that in Figure 3(a) at a magnification of 5 k [25]. Both images demonstrated a compact structure and good grain size. Figure 3(c) shows a detailed elemental analysis of the AgZnONPs using energy-dispersive X-ray spectroscopy (EDX) analysis. The distinct peaks related to Ag, Zn, and O suggest that Ag was effectively integrated into the ZnO crystal structure [26]. The elemental maps of the AgZnONP samples were analyzed separately. The four highlighted elements, Zn, O, C, and Ag, are shown in Figure. 4.

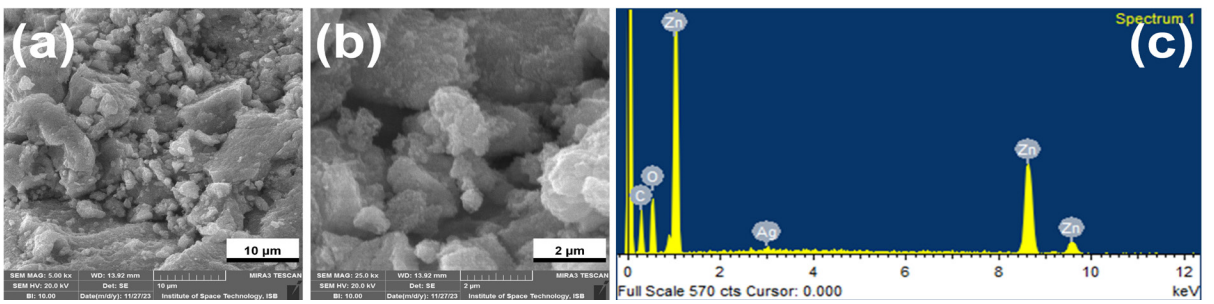

Fig. 3. FESEM images of AgZnONPs: (a) with top view at 5 K magnification, (b) top view at 25 K magnification, and (c) EDX analysis of AgZnONPs.

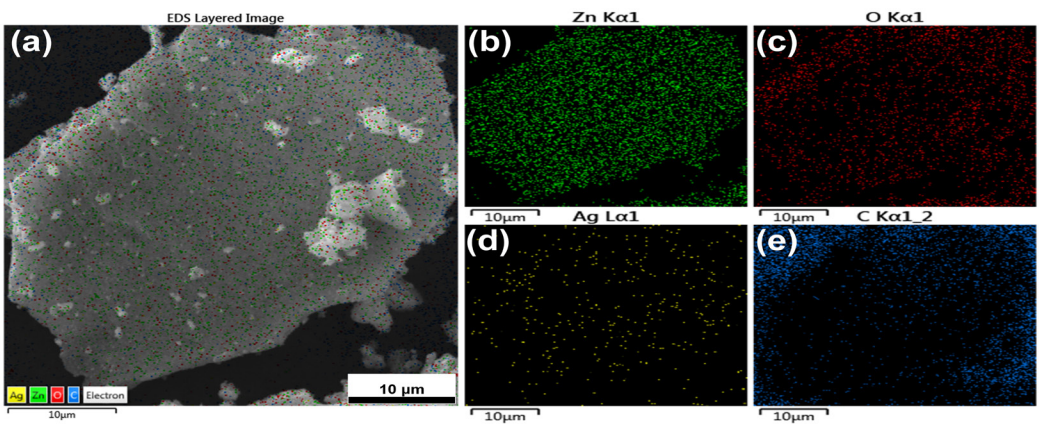

Fig. 4. FESEM images with (a) overall elemental mapping of AgZnONPs, (b) zinc h**ighlighted in green, (c) oxygen** highlighted in red, (d) Ag highlighted in yellow, and (e) carbon highlighted in blue.

3.1.2. X-ray Diffraction analysis of AgZnOPs

The XRD spectra of AgZnONP powder was obtained to confirm its structural properties. The XRD images reveal pure ZnO and AgZnONP diffraction peaks, as shown in Figure 5. The peaks ideally align with the hexagonal/wurtzite structure characterized by the space group P63mc (JCPDS No. 00-036-1451) [27]. It is evident that the 2θ values at 31.6°, 34.3°, and 36.1°, which represent the crystal planes (100), (101), and (101), respectively, make up the pattern of pure ZnO. In contrast, the diffraction peaks for AgZnONPs exhibited at 2θ = 31.7°, 34.4°, and 36.2°, corresponding to the change compared to undoped ZnO nanoparticles (ZnONPs) [28]. A prominent shift and higher values of the diffraction peaks of AgZnONPs are clearly visible in the figure, verifying the structural alteration in AgZnONPs as Ag+ ions are integrated into the ZnO Crystal lattice.

3.1.3. UV-VIS Spectroscopy of undoped ZnONPs and AgZnOPs

Figure 6 displays the UV-visible absorption spectra of the undoped AgZnOPs (red line) and ZnONPs (black line). The absorption edge of the undoped ZnONPs appeared at 396 nm with a lower intensity than that of the AgZnONPs at 411 nm. In the visible spectrum, silver doping increases the absorption intensity, accompanied by a noticeable increase in surface plasmon resonance (SPR), which is explained by the surface plasmon resonance (SPR) effect produced by silver nanoparticles [29]. The electronic band structure is changed and a red shift is indicated by the bandgap energy decreasing from 3.12 eV for undoped ZnONPs to 3.07 eV for AgZnONPs [30]. The effective integration of Ag into the matrix of ZnO was confirmed by the increase in optical absorption and change in bandgap energy.

3.1.4. FTIR of undoped ZnONPs and AgZnONPs

The undoped ZnONPs and AgZnONPs' FTIR spectra were captured in order to investigate the functional groups, vibrational modes, and bonding characteristics of the samples. Both materials exhibited distinctive absorption bands in the FTIR spectra, as shown in Figure 7, with significant variations observed upon silver doping. The

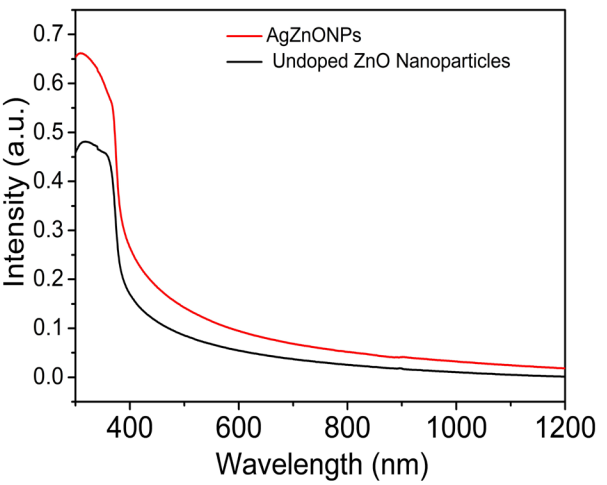

Fig. 6. UV-visible absorption spectrum of undoped ZnONPs and AgZnONPs.

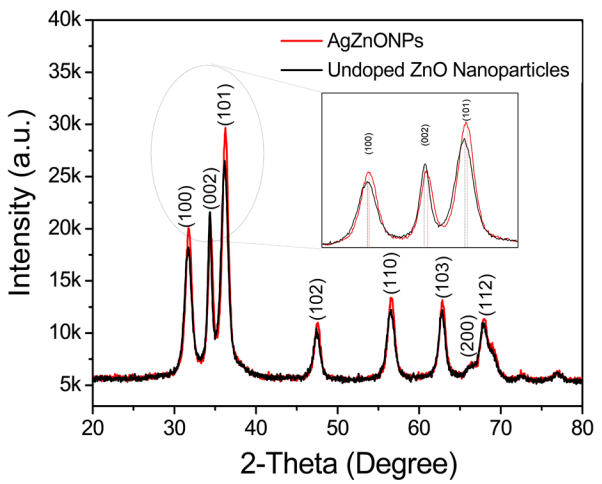

Fig. 5. XRD analysis of AgZnONPs (inset: higher magnification results of the main peaks).

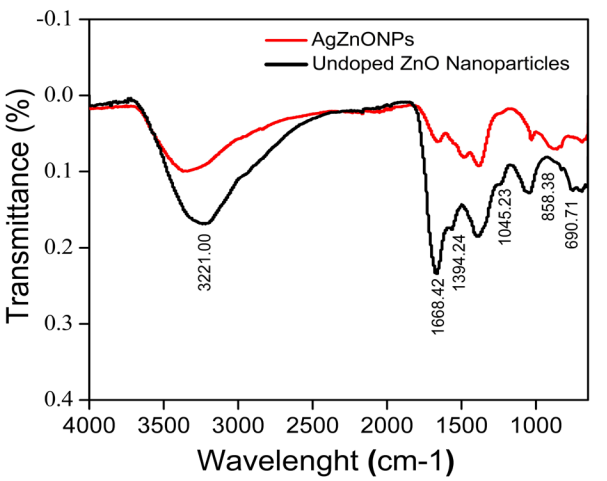

Fig. 7. FTIR spectra of undoped ZnONPs and AgZnONPs.

presence of surface-adsorbed moisture or hydroxyl groups is likely the cause of the broad absorption bands observed in both spectra at around 3000-3600 cm^{-1} and 1600 cm^{-1}, respectively. These bands were attributed to vibrations caused by O-H stretching and H-O-H bending. Additionally, both samples depict bands at about 1394 cm^{-1} and 1045 cm^{-1}, which are tentatively attributed to C-O stretching vibrations that may be caused by adsorbed ambient CO_2 [31]. The distinctive stretching vibration of the Zn-O lattice in undoped ZnO was detected at 690.71 cm^{-1}. The metal-oxide bond (ZnO) is associated with a band between 400 and 750 cm^{-1} [32-34]. The peaks in the Ag-doped ZnO spectrum are slightly moved to a lower wavenumber (688.69 cm^{-1}), suggesting that the addition of Ag ions has caused a little expansion of the ZnO lattice or a change in the strength of the Zn-O bond [35, 36]. Most prominently, the FTIR spectrum of Ag-doped ZnO shows a novel absorption peak at 858.38 cm^{-1} that is absent from the undoped ZnO spectrum. This new peak was ascribed to the stretching vibration of Ag inclusion [37].

3.2. Adsorption Studies

Adsorption performance tests are crucial for ensuring the efficacy of the adsorption method, selecting the most effective material, and optimizing the adsorption process for treating MS.

3.2.1. Effect of pH, contact time, adsorbate concentration, adsorbent dosage

The impact of pH on the AgZnONPs based MS degrading efficiency is depicted in Figure 8(a). The pH range of 3 - 10 was evaluated at a constant adsorbent concentration of 0.5 g/L. At pH 7, the removal efficiency reached a maximum of 92%, representing a considerable increase from 50% at pH 3, indicating that melanoidin adsorption improved under near-neutral conditions [38]. Figure 8(b) shows a diagram of the melanoidin removal efficiency as a function of contact time, with a constant adsorbent concentration of 0.5 g/L. The contact time was varied from 10 min to 120 min. The figure shows that when the contact duration was extended from 10 to 90 minutes, the melanoidin removal efficiency increased quickly from 40% to 92%. After 90 minutes, equilibrium was reached, and the highest color removal efficiency was 92% [39]. Similarly, Figure 9(a) shows how the concentration of melanoidin affects the AgZnONPs ability to absorb. The range of melanoidin values was 50 - 500 mg/L. The 45 mg/g of adsorption capacity at 50 mg/L was elevated to

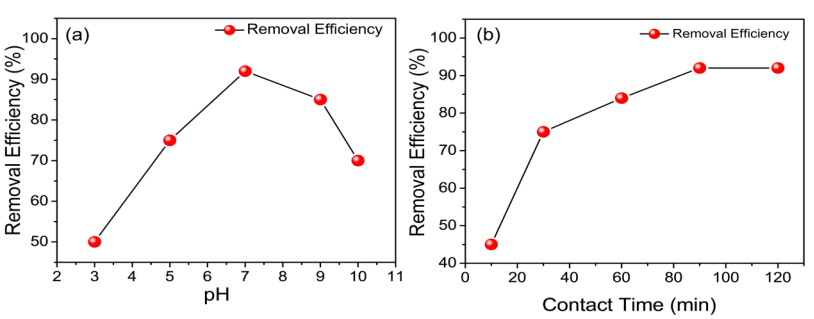

Fig. 8. Adsorption performance analysis: (a) effect of pH on melanoidin removal and (b) effect of contact time on melanoidin removal.

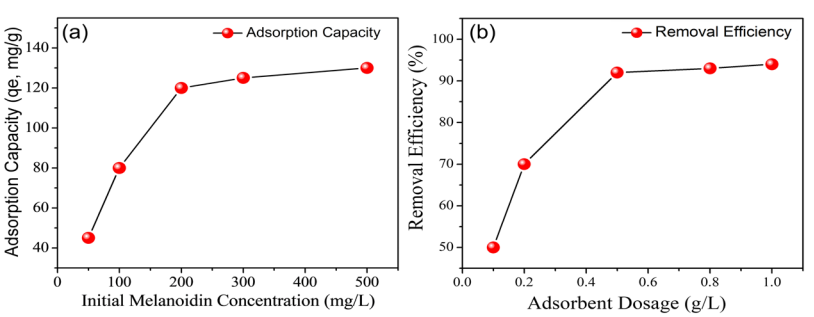

Fig. 9. Adsorption performance analysis: (a) initial melanoidin concentration effect on adsorption capacity and (b) adsorbent dosage effect on melanoidin removal efficiency.

120 mg/g at a concentration of 200 mg/L. When the concentration exceeded 200 mg/L, the adsorption capacity steadily increased to 130 mg/g at 500 mg/L [40]. Figure 9(b) demonstrates the dosage effect on the remediation of MS. The result indicates that the remediation efficacy increases from 50% to 92% if the dosage of AgZnONPs is increased from 0.1 g/L to 0.5 g/L. The consequent pattern is ascribed to the expanded accessibility of active adsorption sites with a maximum adsorbent concentration, resulting in improved pollutant removal until the sites approach saturation [41]. After the dosage was raised over 0.5 g/L, only marginal changes were observed, ranging from 93% to 94% for dosages of 0.8 g/L to 1 g/L.

3.3. Isothermal Analysis

The adsorption isotherms after treatment with MS were studied to evaluate the basic understanding and optimize the sorption process of AgZnONPs. The isothermal models, which were tested using the Langmuir isotherm and Freundlich isotherm are exhibited in Figure 10(a) and Figure 10(b), respectively. The values of the correlation coefficients were in the high range for the Langmuir model ($R^2 = 0.995$) and low range for the Freundlich model ($R^2 = 0.982$). There are no interactions between adsorbed molecules in the Langmuir model, which is a single-layer homogeneous adsorption model. In contrast, the Freundlich model describes multilayered and heterogeneous adsorption phenomena. An excellent fit is provided by the Langmuir model for melanoidin adsorption on the AgZnONPs surface [42]. The specific constant values for both models are listed in Table 1.

3.4. Kinetics Analysis

Adsorption kinetics were evaluated using practical data after treating MS with AgZnONPs to obtain basic information on the rate, mechanism, and efficiency of pollutant removal during the adsorption process. The pseudo-second-order and pseudo-first-order kinetic models are displayed in Figure 11(a) and 10(b), respectively. The kinetic results presented in Table 2 show that the pseudo-second-order kinetic model had a better coefficient

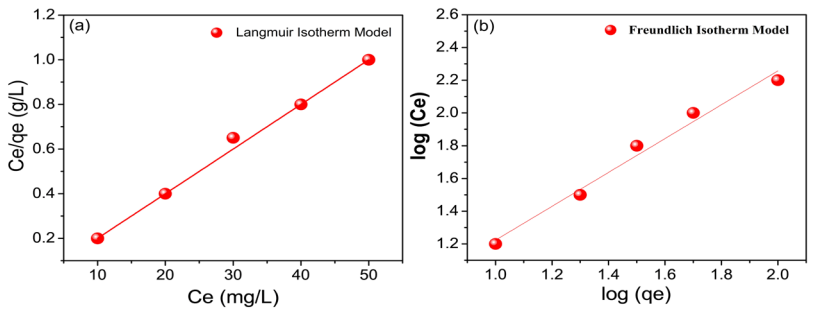

Fig. 10. Adsorption isotherm analysis: (a) Langmuir isotherm model and (b) Freundlich isotherm model.

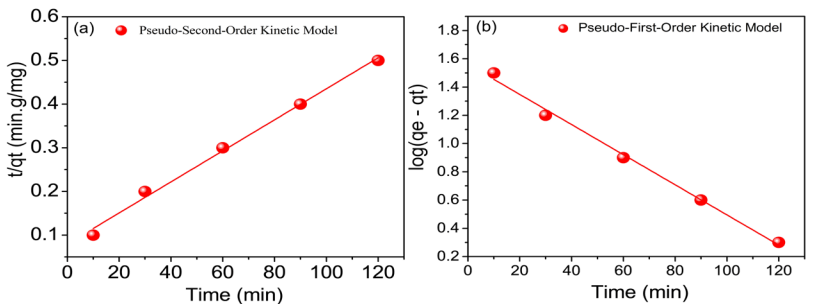

Fig. 11. Adsorption kinetics analysis: (a) pseudo second-order kinetic model and (b) pseudo first-order kinetic model.

Table 1. Linear equations of isotherm models and their constants.

Isotherm models	Linear form	Plots	Constants
Langmuir	$\frac{C_e}{q_e} = \frac{C_e}{q_m} + \frac{1}{K_l q_m}$	$\frac{C_e}{q_e} Vs\ C_e$	q_m = 50mg/g R^2= 0.995
Freundlich	$\log q_e = \log K_f + \left(\frac{1}{n}\right) log C_e$	$log q_e Vs \log C_e$	n=1 R^2=0.982

Table 2. Linear form of Kinetic models and the values of their constants.

Kinetic models	Linear form	Plots	Constants
Pseudo-first order	$\log(q_e - q_t) = logq_e - (K_1/2.303)t$	$\log(q_e - q_t)\ vs\ t$	$k_1 = 0.010$ $R^2 = 0.988$
Pseudo-second order	$\frac{t}{q_t} = \left(\frac{1}{K_2 q_e^2}\right) + (\frac{t}{q_e})$	$\frac{t}{q_t} vs\ t$	$K_2 = 0.00018$ $R^2 = 0.994$

value (R^2 = 0.994) than the pseudo-first-order kinetic model (R^2 = 0.988). Figure 11(a) shows that chemisorption is the speed-limiting step, and this adaptation suggests that chemical interactions between melanoidin and AgZnONPs dominate the adsorption process. The kinetic results indicated that the pseudo-second-order model was more favorable than the pseudo-first-order model for this process [43].

3.5. Melanoidin Removal by AgZnONPs

The AgZnONP-based removal of melanoidin was quantified by changes in the UV-Visible spectrum, as shown in Figure 12. The untreated MS exhibited a prominent absorbance peak at 291 nm, which can be ascribed to the presence of conjugated systems and aromatic moieties capable of absorbing light within the 200–400 nm range [44]. The absorbance at this π→π* wavelength is primarily associated with electronic transitions involving C=C and C=O bonds linked to the aromatic structures [45]. A clear decrease in absorbance intensity was observed after adsorption treatment, suggesting that melanoidin and the adsorbent material interacted well. The

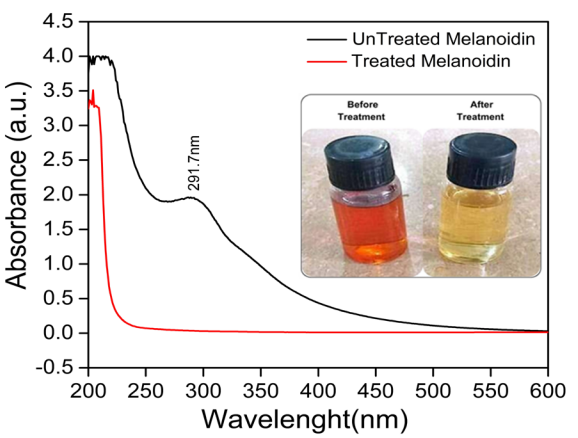

Fig. 12. UV-Visible analysis of untreated and treated MS using AgZnONPs.(Inset: Photographic comparison of MS before and after treatment with AgZnONPs).

results indicate that AgZnONPs treatment of MS results in chromophoric groups in the solution, which leads surface complexation, hydrogen bonding, and electrostatic attraction to cause melanoidin to engage with the nanoparticles, resulting in the reduction of larger aggregates of melanoidin into smaller fragments with distinct UV absorption properties [46-48]. The changes can also be seen through a pictorial comparison of before and after treatment with MS. The inset of Figure 11 clearly shows the color change from dark brown to light yellow for concentrated MS.

3.6. Comparison with other adsorbents

To approximate the interpretation of the as-synthesized AgZnONPs with other reported adsorbents such as activated carbon, Fe-impregnated activated carbon, and oxides of metals for the removal of MS, a comparative assessment is demonstrated in Table 3. These results clearly shows that nanomaterials such as graphene oxide nanosheets exhibited significantly increased theoretical adsorption capacities, with a value of 18,310 mg/g. Although the values are promising, it is essential to note that this performance was accomplished under highly acidic conditions, with a pH of 2, which poses multiple challenges for practical applications. Activated carbon is highly effective, as demonstrated by the 85.6 percent removal efficacy of melanoidin; however, it has several drawbacks, including waste generation, limited reusability, high cost, and sustainability concerns. Similarly, the TiO_2-ZnO composite showed an 86% removal rate; however, using metal oxides as composites makes them costly and limited for large-scale industrial applications. Unlike conventional adsorbents, AgZnONPs overcome these limitations through nanoscale dispersion and the presence of Ag^+ ions, which increase the pollutant binding affinity and electron transmission. Finally, this study exhibits a tantalizing blend with

Table 3. Comparison of adsorbents from previous literature studies.

S. No.	Adsorbent	Max. Adsorption Capacity (mg/g)	Removal Efficiency (%)	Optimal pH	Contact Time (min)	Reference
1	Graphene Oxide Nanosheets	18,310	-	2	120	[49]
2	Chitin Nanofibers	131	-	-	-	[50]
3	Fe-impregnated Activated Carbon	-	85.6	-	75	[51]
4	Coal Fly Ash	281.34	84	6	120	[52]
5	Mesoporous Activated Carbon	23.71	-	-	-	[53]
6	TiO_2-ZnO/AC Composite	-	86	-	-	[54]
7	AgZnONPs	50	92	7	90	This Study

a high removal efficiency (92%) and a respectable adsorption capacity (130 mg/g) under a neutral pH of 7. This functional advantage distinguishes AgZnONPs from other conventional and advanced adsorbents, making them promising nano-material for distillery wastewater treatment.

4. CONCLUSIONS

In summary, AgZnONPs were successfully synthesized using a cost-effective solution process and efficiently used for the adsorption-based removal of MS. The synthesized AgZnONPs were examined using FESEM, XRD, UV-VIS spectroscopy, and FTIR spectroscopy. The structural properties of AgZnONPs were confirmed along with the confirmation of the doping of Ag in ZnO nanoparticles. In addition, MS was treated with AgZnONPs, which resulted in a clear light-yellow solution. UV-Vis absorption spectroscopy confirmed the removal of melanoidin from the treated MS. The AgZnONP-based treatment resulted in an extraordinary adsorption capacity with a maximum removal efficiency of 92%, the best pH value of the treated solution was 7, the initial melanoidin concentration was 200 mg/L for maximum removal efficiency, and the adsorbent dosage of AgZnONPs was 0.5 g/L. In addition, the adsorption performance confirmed that the Langmuir isotherm and pseudo second-order kinetics were feasible and that single-layered sorption and chemisorption mechanisms were feasible. These results highlight the potential of AgZnONPs for the treatment of MS in industrial-scale operations. In order to increase the practical application of AgZnONPs and make it possible for their industrial use to treat distillery effluent, future research should concentrate on their regeneration and reusability.

5. ACKNOWLEDGEMENTS

This study was financially supported by the Higher Education Commission of Pakistan through its National Research Program for Universities (NRPU-7617,2017) and a Deans Research Grant from the Dean of Science and Engineering at the University of Karachi.

6. CONFLICT OF INTEREST

The authors declare no conflict of interest.

7. REFERENCES

1. J.C.-T. Lin, Y.-S. Liu, and W.-K. Wang. A full-scale study of high-rate anaerobic bioreactors for whiskey distillery wastewater treatment with size fractionation and metagenomic analysis of granular sludge. *Bioresource Technology* 306: 123032 (2020).
2. B. Hu, L. Li, Y. Hu, D. Zhao, Y. Li, M. Yang, A. Jia, S. Chen, B. Li, and X. Zhang. Development of a novel Maillard reaction-based time-temperature indicator for monitoring the fluorescent AGE content in reheated foods. *RSC Advances* 10(18): 10402-10411 (2020).
3. M. Murata. Browning and pigmentation in food through the Maillard reaction. *Glycoconjugate Journal* 38(3): 283-294 (2021).
4. S. Tripathi, K. Singh, A.K. Singh, A. Mishra, and R. Chandra. Organo-metallic pollutants of distillery effluent and their toxicity on freshwater fish and germinating Zea mays seeds. *International Journal of Environmental Science and Technology* 19(3): 2021-2036 (2022).
5. M.S.I. Afrad, M.B. Monir, M.E. Haque, A.A. Barau, and M.M. Haque. Impact of industrial effluent on water, soil and rice production in Bangladesh: A

case of Turag River bank. *Journal of Environmental Health Science and Engineering* 18(2): 825-836 (2020).
6. S. Ratna, S. Rastogi, and R. Kumar. Current trends for distillery wastewater management and its emerging applications for sustainable environment. *Journal of Environmental Management* 290: 112544 (2021).
7. R. Patel, R. Gaur, T. Verma, and R. Singh. Challenges of distillery effluent treatment and its bioremediation using microorganism: A review. *Current World Environment* 18(2): 446-459 (2023).
8. L.-N. Ho, S.-A. Ong, S.-H. Thor, and K.-L. Yap. Feasibility of UVA photocatalytic post-treatment of molasses wastewater: Effects on melanoidins removal, mineralization and oxidation of ammoniacal-nitrogen. *Chemical Engineering and Processing: Process Intensification* 196: 109681 (2024).
9. M. Binazadeh, J. Rasouli, S. Sabbaghi, S.M. Mousavi, S.A. Hashemi, and C.W. Lai. An overview of photocatalytic membrane degradation development. *Materials* 16(9): 3526 (2023).
10. Y. Li, Q. Zhang, S. Xiao, Q. Yang, L. Wang, and J. Hao. Review of melanoidins as by-product from thermal hydrolysis of sludge: Properties, hazards, and removal. *Processes* 12(1): 135 (2024).
11. L. Kheddo, L. Rhyman, M.I. Elzagheid, P. Jeetah, and P. Ramasami. Adsorption of synthetic dyed wastewater using activated carbon from rice husk. *SN Applied Sciences* 2(12): 2170 (2020).
12. J. Naser, Z. Ahmed, and E. Ali. Nanomaterials usage as adsorbents for the pollutants removal from wastewater: A review. *Materials Today: Proceedings* 42(5): 2590-2596 (2021).
13. V.S. Kadam, S.S. Wagh, C.V. Jagtap, S.M. Sutar, and R. Mane. Comparative studies on synthesis and photocatalytic activity of ZnO nanoparticles. *ACS Omega* 8(9): 7779-7790 (2023).
14. A. Abdelfattah and A. El-Shamy. A comparative study for optimizing photocatalytic activity of TiO_2-based composites with ZrO_2, ZnO, Ta_2O_5, SnO, Fe_2O_3, and CuO additives. *Scientific Reports* 14(1): 1 (2024).
15. U. Alalawi, U. Romman, K.M. Saleh, S.T. Shafa, and M.U. Khalid. Ag-doped MnO_2 nanowires integrated with graphitic carbon nitride for enhanced photocatalytic applications for wastewater treatment. *Current Applied Physics* 60: 32-39 (2024).
16. W. Xie, B. Li, X. Wu, D. Han, and Y. Zhang. Surface modification of ZnO with Ag improves its photocatalytic efficiency and photostability. *Journal of Photochemistry and Photobiology A: Chemistry* 215: 53-58 (2010).
17. S.K. Noukelag, L.C. Razanamahandry, S.K.O. Ntwampe, C.J. Arendse, and M. Maaza. Industrial dye removal using bio-synthesized Ag-doped ZnO nanoparticles. *Environmental Nanotechnology, Monitoring & Management* 16: 100463 (2021).
18. M. Nandasana, R. Kamat, R. Mishra, P. Ghosh, and S. Patil. Green synthesis of silver and copper-doped zinc oxide nanoflowers for photocatalytic and antibacterial applications. *Vacuum* 212: 111130 (2025).
19. S. Nagasundari, K. Muthu, K. Kaviyarasu, A. Farraj, and R.M. Alkufeidy. Current trends of silver-doped zinc oxide nanowires photocatalytic degradation for energy and environmental application. *Journal of Environmental Chemical Engineering* 23: 100931 (2021).
20. K. Watcharenwong, A. Kongka, C. Kaeokan, C. Chokejaroenrat, and C. Sakulthaew. Decolorization of melanoidin using sonoFenton and photoFenton processes. *Waste* 1(2): 455-467 (2023).
21. K. Brudzynski and D. Miotto. The recognition of high molecular weight melanoidins as the main components responsible for radical-scavenging capacity of unheated and heat-treated Canadian honeys. *Food Chemistry* 125(2): 570-575 (2011).
22. A.L. Jembere and M.B. Genet. Comparative adsorptive performance of adsorbents developed from sugar industrial wastes for the removal of melanoidin pigment from molasses distillery spent wash. *Water Resources and Industry* 26: 100165 (2021).
23. E.D. Revellame, D.L.B. Fortela, W. Sharp, R. Hernandez, and M.E. Zappi. Adsorption kinetic modeling using pseudo-first order and pseudo-second order rate laws: A review. *Cleaner Engineering and Technology* 1: 100032 (2020).
24. M.H. Rahman, M. Marufuzzaman, M.A. Rahman, and M.I.H. Mondal. Adsorption kinetics and mechanisms of nano chitosan coated cotton fiber for the removal of heavy metals from industrial effluents. Heliyon 11(1): e42932 (2025).
25. J.H. Mahamud, A.B. Gemta, A.K. Hordofa, G.A. Argaw, U. Sherefedin, M. Ahmed, T.F. Hurrisa, and T. Gurumurthi. Green synthesis and characterization of silver-doped ZnO nanoparticles using tobacco leaf extract: A novel hydrothermal approach for antibacterial and antifungal applications. *AIP Advances* 15(4): 045030 (2025).
26. S. Hussain, A. Fiaz, A. Almohammedi, and A. Waqar. Optimizing photocatalytic performance

with Ag-doped ZnO nanoparticles: Synthesis and characterization. *Heliyon* 10(15): e35725 (2024).

27. O.A. Zelekew, S.G. Aragaw, F.K. Sabir, D.M. Andoshe, A.D. Duma, D.-H. Kuo, X. Chen, T.D. Desissa, B.B. Tesfamariam, G.B. Feyisa, H. Abdullah, E.T. Bekele, and F.G. Aga. Green synthesis of Co-doped ZnO via the accumulation of cobalt ion onto Eichhornia crassipes plant tissue and the photocatalytic degradation efficiency under visible light. *Materials Research Express* 8(2): 025010 (2021).
28. K. Raza, A. Sayeed, M. Naaz, M. Muaz, S. Rahaman, F. Sama, K. Pandey, and A. Ahmad. Green synthesis of ZnO nanoparticles and Ag-doped ZnO nanocomposite utilizing Sansevieria trifasciata for high-performance asymmetric supercapacitors. *ACS Omega* 9(30): 32444-32458 (2024).
29. M. Karimi-Nazarabad and E. Goharshadi. Ag and Ni doped graphitic carbon nitride coated on wood as a highly porous and efficient photo absorber in interfacial solar steam generation. *Journal of Porous Materials* 30(6): 1835-1845 (2023).
30. R. Radičić, D. Maletić, D. Blažeka, J. Car, and N. Krstulović. Synthesis of silver, gold, and platinum doped zinc oxide nanoparticles by pulsed laser ablation in water. *Nanomaterials* 12(19): 3484 (2022).
31. Z.N. Kayani, F. Manzoor, A. Zafar, M. Mahmood, M. Rasheed, and M. Anwar. Impact of Ag doping on structural, optical, morphological, and photoluminescent properties of ZnO nanoparticles. *Optical and Quantum Electronics* 52(7): 344 (2020).
32. M.B. Islam, M.J. Haque, N.M. Shehab, and M.S. Rahman. Synthesis and characterization (optical and antibacterial) of Ag-doped ZnO nanoparticles. *Open Ceramics* 14: 100370 (2023).
33. N. Ahmed, Z. Khalil, Z. Farooq, K.-U. Haq, S. Shahid, R. Ramiza, P. Ahmad, K.W. Qadir, R. Khan, and Q. Zafar. Structural, optical, and magnetic properties of pure and NiFe-codoped zinc oxide nanoparticles synthesized by a sol-gel autocombustion method. *ACS Omega* 9(1): 137-148 (2023).
34. N. Sedky, A. Afify, A. Almohammedi, E.M.M. Ibrahim, and A.M. Ali. Structural, optical, photoluminescence and magnetic investigation of doped and co-doped ZnO nanoparticles. *Optical and Quantum Electronics* 55: 456 (2023).
35. M. Busilă, V. Mușat, P. Alexandru, C. Romanitan, O. Brîncoveanu, V. Tucureăneanu, I. Mihalache, A.-V. Iancu, and V. Dediu. Antibacterial and photocatalytic activity of ZnO/Au and ZnO/Ag nanocomposites. *International Journal of Molecular Sciences* 24(23): 16939 (2023).
36. T.M. Irine and A. Rathika. Synthesis of silver (Ag) doped zinc oxide nanoparticles as efficient photocatalytic activity for degradation of methylene blue dye. *Journal of Advanced Scientific Research* 13(2): 129-134 (2022).
37. M.A. Kareem, I. Bello, H. Shittu, and P. Sivaprakash. Synthesis, characterization, and photocatalytic application of silver doped zinc oxide nanoparticles. *Cleaner Materials* 3: 100041 (2022).
38. L. Ashwini, L. Saravanan, M. Sabari, M. Astalakshmi, and N. Kanagathara. Effect of Cu doping with varying pH on photocatalytic activity of ZnO nanoparticles for the removal of organic pollutants. *Inorganic Chemistry Communications* 155: 111137 (2023).
39. N. Medoiuni, C. Guillard, F. Dappozze, L. Khrouz, S. Parola, C. Colbeau-Justin, A.B.H. Amara, H.B. Rhaiem, N. Jaffrezic-Renault, and P. Namour. Impact of structural defects on the photocatalytic properties of ZnO. *Journal of Hazardous Materials Advances* 6: 100081 (2022).
40. K. Akpomie and J. Conradie. Synthesis, characterization, and regeneration of an inorganic-organic nanocomposite (ZnO@biomass) and its application in the capture of cationic dye. *Scientific Reports* 10(1): 14441 (2020).
41. S. Rizvi, A. Singh, and S.K. Gupta. A parametric study using Box-Behnken design for melanoidin removal via Cu-impregnated activated carbon prepared from waste leaves biomass. *Applied Water Science* 12(4): 81 (2022).
42. R. Syaifuddin, R. Wahdah, A. Abdullah, and A.R. Saidy. Sorption of phosphate onto surfactant-modified zeolite particles. International Journal of Sciences: *Basic and Applied Research* 61(1): 87-96 (2022).
43. L.Q. Vo, A.-T. Vu, T.D. Le, C.D. Huynh, and H.V. Tran. Fe_3O_4/graphene oxide/chitosan nanocomposite: A smart nanosorbent for lead(II) ion removal from contaminated water. *ACS Omega* 9(15): 17506-17517 (2024).
44. S. Singh, S. Nimse, D.E. Mathew, A. Dhimmar, H. Sahastrabudhe, A. Gajjar, V. Ghadge, P. Kumar, and P.B. Shinde. Microbial melanin: Recent advances in biosynthesis, extraction, characterization, and applications. *Biotechnology Advances* 53: 107773 (2021).
45. X. Huang, W. Ye, J. Zhuang, C. Hu, H. Dong, B. Lei, and Y. Liu. π-Conjugated structure enhances the UV absorption performance of carbon dots and

application in the design of light-colored sunglasses. *ACS Sustainable Chemistry & Engineering* 12(28): 10399-10408 (2024).

46. M. Han, H. Zhao, Z. Liu, J. Liu, X. Li, F. Hang, K. Li, and C. Xie. Color development characteristic and kinetic modeling of Maillard reaction in membrane-clarified sugarcane juice during vacuum evaporation process. *Foods* 14(12): 2136 (2025).
47. B.-H. Fan, Y.-S. Xiong, M.-X. Li, R. Jia, L.-S. Zhou, J.-Y. Tang, W. Li, Y.-W. Lan, H.-Q. Lu, and K. Li. Effective melanoidin adsorption of polyethyleneimine-functionalised molasses-based porous carbon: Adsorption behaviours and microscopic mechanisms. *Separation and Purification Technology* 310: 123016 (2022).
48. I. Šarić and I. Despotović. Hydrogen bonds as stability-controlling elements of spherical aggregates of ZnO nanoparticles: A joint experimental and theoretical approach. *Materials* 16(13): 4843 (2023).
49. S.M. Rafigh and A.R. Soleymani. Melanoidin removal from molasses wastewater using graphene oxide nanosheets. *Separation Science and Technology* 55(13): 2281-2293 (2020).
50. R. Dolphen and P. Thiravetyan. Adsorption of melanoidins by chitin nanofibers. *Chemical Engineering Journal* 166(3): 890-895 (2011).
51. S. Rizvi, L. Goswami, and S.K. Gupta. A holistic approach for melanoidin removal via Fe-impregnated activated carbon prepared from Mangifera indica leaves biomass. *Bioresource Technology Reports* 12: 100591 (2020).
52. S. Ahmed, I.N. Unar, H.A. Khan, G. Maitlo, R.B. Mahar, A.S. Jatoi, A.Q. Memon, and A.K. Shah. Experimental study and dynamic simulation of melanoidin adsorption from distillery effluent. *Environmental Science and Pollution Research* 27: 9619-9636 (2020).
53. K. Suwannahong, S. Wongcharee, J. Rioyo, C. Sirilamduan, and T. Kreetachart. Insight into molecular weight cut-off characteristics and reduction of melanoidin using microporous and mesoporous adsorbent. *Engineering and Applied Science Research* 49(1): 47-57 (2021).
54. B.O. Otieno, S.O. Apollo, B.E. Naidoo, and A. Ochieng. Photodecolorisation of melanoidins in vinasse with illuminated TiO_2-ZnO/activated carbon composite. *Journal of Environmental Science and Health, Part A* 52(7): 616-623 (2017).

Proceedings of the Pakistan Academy of Sciences: A Physical and Computational Sciences 62(3): 247-261 (2025)

ISSN (Print): 2518-4245; ISSN (Online): 2518-4253
http://doi.org/10.53560/PPASA(62-3)698

Pakistan Academy of Sciences

Research Article

Wind Energy Modelling and Machine Learning Approach to Study Wind Direction Effect

Muhammad Raza[1*], Adeel Tahir[2], Zeshan Iqbal[3], Zaheer Uddin[3], Ejaz Ahmed[4], Majid Hussain[5], Arif A. Azam[3], and Naeem Sadiq[5]

[1]Department of Physics, Karakoram International University, Gilgit-Baltistan, Pakistan
[2]Department of Physics, Federal Urdu University of Arts, Science & Technology, Karachi, Pakistan
[3]Department of Physics, University of Karachi, Karachi, Pakistan
[4]Department of Physics, Model College for Boys G-6/3, Islamabad, Pakistan
[5]Institute of Space Science & Technology, University of Karachi, Karachi, Pakistan

Abstract: Wind energy is one of the green renewable energy sources that is available everywhere. The wind-generated electrical energy is much less than the available wind potential. No windmill can even harness 50% of the available wind energy. A lot of research investigations are still needed to explore and harness the maximum energy from wind potential. This work is one of such series of research, in which we modeled wind speed using the Weibull distribution through a Python program that uses the least square method based on Python built-in functions and evaluated the shape and scale parameters of the distribution. The program also compares parameters calculated by other existing methods. The Python program based on the least square method fits the Weibull distribution well compared to the existing methods. The maximum value of scale parameters was found in June (more than 6.2), the corresponding value is also close in May, where it is more than 6.1; the other two months that follow June and May (July and September) have scale parameters near 5.7. It shows that the wind potential is maximum in June, and reasonable wind energy is available in May, July, and September. The effect of wind direction on the modelling of wind speed is also investigated. Perhaps it is the first study that involves wind direction in wind speed modelling. Two different Artificial Neural Network Architectures were studied with and without wind directions in the input. It was found that the results improve if wind direction is also taken in the list of input parameters. The Root Mean Square Error is the least (RMSE = 0.7224) for the model which includes wind direction in the input layer, the performance indicator (0.5219) is also the best for this architecture as compared to the other three.

Keywords: Weibull Distribution, Wind Energy Modelling, Python Programming, Least Squares Method, Machine Learning, Artificial Neural Networks (ANN), Wind Direction.

1. INTRODUCTION

Wind speed prediction through meteorological parameters is a critical area of research in renewable energy, particularly for assessing wind energy potential. The Weibull distribution has emerged as a widely adopted statistical model for characterizing wind speed data due to its flexibility in capturing the stochastic nature of wind patterns. Numerous studies have explored methods to estimate the Weibull parameters (shape k and scale c) and evaluate their accuracy, often leveraging computational tools and regional wind datasets. Elahi *et al.* [1] developed a Python library, *windz*, incorporating six methods, viz., Method of Moments (MoM), Empirical Method (EM), Energy Pattern Factor Method (EPFM), Maximum Likelihood Method (MLM), Modified Maximum Likelihood Method (MMLM), and Maximum Entropy Principle (MEP), to analyze wind speed data from three Pakistani cities

Received: July 2025; Revised: August 2025; Accepted: September 2025
* Corresponding Author: Muhammad Raza <raza.physics@kiu.edu.pk>

(Harnai, Jacobabad, Talagang) [1]. Their findings highlighted the Modified Maximum Likelihood Method (MMLM) as the most efficient, while the graphical method was deemed the least effective. Similarly, Zahid *et al.* [2] introduced a computer package for wind speed modelling, emphasizing the utility of MMLM and MLM through statistical error tests (Mean square, Chi-square, R-square). Regional Studies in Pakistan provided information on the viability of site-specific wind energy. Khan *et al.* [3] compared the coastal wind profiles of Gwadar and Pasni, revealing greater stability in the Gwadar (parameter of form k = 4 - 6), but greater wind energy density in Pasni. Khan *et al.* [3] also compared four methods (MoM, EM, EPFM, MLM) using Jiwani's wind data (1998 - 2007) and found that while all methods yielded nearly identical scale parameters (*c*), MLM provided the best agreement with measured mean wind speeds [4, 5]. However, in a separate study analyzing Ormara's data, Khan *et al.* [4] concluded that MoM, EMP, and MLM outperformed MMLM in estimating shape parameters (*k*), with differences within 0.3. These discrepancies underscore the context-dependent efficacy of parameter estimation methods.

Recent studies have proposed novel approaches to improve accuracy. Uddin and Sadiq [6] introduced the Method of Quartiles (MOQ), which calculates *k* and *c* using the first and third quartiles. This method has demonstrated lower values of the Akaike Information Criterion (AIC) and reduced overestimation of wind density compared to traditional methods, positioning MOQ as superior to cities such as Karachi, Hyderabad, and Quetta. Rajput *et al.* [7], through advanced computational efficiency, suggested a simplified gamma function formula for estimating scale parameters, achieving an error <0.2% and validating MLM as the most accurate method for Hyderabad wind potential. They classified Hyderabad as the most promising wind power site in Pakistan, followed by Karachi, due to consistent wind speeds that exceed the turbine cutting thresholds. On the other hand, cities like Peshawar and Lahore showed insignificant potential except for specific months. The integration of programming tools significantly enhanced validation processes.

Rehman *et al.* [8] developed a Python-based Newton-Gauss technique, showing minimum RMSE and AIC values for four cities, thus offering a robust alternative to established methods. These innovations highlight the growing role of computational tools in improving parameter estimation accuracy. They approved the Python programs to automate the estimation of parameters, emphasizing the importance of software in modern wind energy research.

Uddin *et al.* [9] employed a least squares method (LSM) to evaluate Lagrange multipliers for MEP, reaching better adjustments than classic MEP through Python-based error metrics (RMSE, Chi-Square). While the Weibull distribution is widely used, Sadiq [10] demonstrated that extreme (generalized) value distributions have better modeled continuous and seasonal winds of Karachi with 95% confidence. This discovery emphasizes the need to select a specific context model, particularly in coastal urban environments.

The forecast of wind speed evolved significantly with the integration of machine learning techniques (ML) and deep learning (DL), particularly when combined with weather parameters. Although probabilistic models such as the Weibull distribution remain fundamental, recent studies emphasize the role of data-oriented approaches to improve accuracy and address the stochastic nature of wind patterns in Machine Learning and Hybrid Models for Wind Speed Prediction. Artificial Neural Networks (ANNs) and Genetic Expression Programming (GEP) emerged as robust tools for short-term wind speed forecast. Ghorbani *et al.* [11] compared ANN, GEP, multiple linear regression (MLR), and the persistence method using autocorrelation functions to determine input delays for wind speed data per hour from Kersey, Colorado. Their findings revealed that ANN and GEP performed comparably, with MLR surpassing MLR and persistence. Similarly, Demolli *et al.* [12] demonstrated the transferability of ML models (for example, random forest, increased gradient) for long-term wind energy forecasting in geographical places, highlighting their usefulness in the pre-assessment of the feasibility of wind farms in undeveloped areas.

Hybrid models increase predictive accuracy. Zhu *et al.* [13] suggest an amalgamation of convolutional neural networks and a Multilayer Perceptron for the wind farm data. Hur [14] proposed a two-stage method using an Extended

Kalman filter to estimate, and then a neural network for short-term forecasting of the wind speed. These hybrid approaches illustrate practical applications in wind power systems. Li and Jin [15] have also developed a hybrid model that combines resource selection, machine learning, and multi-objective optimization. Its application to the wind speed data from Penglai, China, generated unique objective models. Advanced uncertainty modelling related to convective wind was addressed by Ehsan *et al.* [16] by comparing Quantile Regression Forests and Bayesian Additive Regression Trees for the tempest. The QRF stood out in points and PIS estimates, reducing systematic errors and supporting emergency preparation during the extreme climate.

Regional studies emphasize the adaptability of ML models to local weather conditions. Türkan *et al.* [17] predicted the wind speed to 30 m high using 10 m data in Türkiye, identifying Support Vector Machines (SVM) as the most accurate method. In Malaysia, Hanoon *et al.* [18] evaluated the regression of the Gaussian process (GPR), increased the trees (BT), and SVR in 14 stations, with GPR reaching higher accuracy, despite the challenges in the correlation force. These studies emphasize the importance of adapting models to regional wind regimes and integrating pre-processing techniques to improve performance.

While existing studies validate ML/DL models for wind speed forecasting, challenges persist in dealing with non-stationary data and incorporating various weather variables (e.g., temperature, humidity). Hanoon *et al.* [18] emphasized the need to integrate optimization algorithms to improve the correlation between the expected and observed values. These gaps present opportunities for new structures, such as the ANN-Weibull hybrid proposed in this study, which takes advantage of the meteorological parameters for probabilistic forecasting. Han *et al.* [19] proposed a hybrid model that integrated research and weather forecast simulations (WRF), decomposition of the empirical mode of the complete set (Ceemdan), and a bidirectional CNN LSTM network optimized by attention mechanisms.

Cadenas and Rivera [20] employed Autoregressive Integrated Moving Average (ARIMA) models to predict wind speed in Oaxaca, Mexico, incorporating wind direction along with temperature and moisture, and reported greater accuracy in the capture of seasonal wind variability. Similarly, Foley *et al.* [21] used Support Vector Machines (SVM) to predict the production of wind energy in Ireland, emphasizing the direction of the wind as a critical factor to resolve the dynamics of the coastal wind. Their work has shown that directional data reduced RMSE by 18% compared to the models excluding this variable.

Lydia *et al.* [22] developed a wind speed forecast system using SVM and K-Nearest Neighbors (K-NN) with inputs, including wind direction, but its structure lacked the nonlinear modelling capacity of the RNAs to deal with complex interactions between variables. Liu *et al.* [23] proposed a hybrid forecast model that combines transformations of Wavelets and Gradient reinforcement machines, but their approach did not explore ANS' potential to autonomously learn hierarchical characteristics from directional and temporal data. The absence of an ANN-based framework in these studies represents a difference in the literature, as ANS specifically suits non-linear relationships and sequential dependence, adapted to the sequential dependence contained in meteorological datasets. The task addresses this difference by developing an ANN-based model that integrates the air direction with temperature, humidity, and the precursor air speed values, using Python libraries such as TensorFlow and causes for implementation. Our approach not only creates fundamental insights of pre-studies but also introduces a novel application of ANNs to increase prediction accuracy in air speed modelling.

2. MATERIALS AND METHODS

Weibull Distribution is one of the most widely used distributions for modelling wind speed distributions. Shape (k) and a scale parameter (c) characterized this distribution through its cumulative distribution function (CDF) as:

$$F(v;k,c) = 1 - e^{-\left(\frac{v}{c}\right)^k} \quad (1)$$

Where $F(v;k,c)$ is a function that provides the cumulative probability of observing a particular wind speed, and v is the wind speed. The shape parameter determines the shape of the distribution (e.g., spread or skewness) through any of the $k < 1$ (high frequency of low wind speeds), $k = 1$

(represents exponential distribution; wind speeds are randomly and uniformly distributed over time), or $k > 1$ (high frequency of high wind speeds). The scale parameter (c) represents the characteristic wind speed, indicating the range or magnitude of wind speeds. Higher values of c signify stronger average wind speeds in the region being analyzed. The Probability Density Function (PDF) can be presented as [24]:

$$W(v;k,c) = \left(\frac{k}{c}\right)\left(\frac{v}{c}\right)^{k-1} \exp\left(-\left(\frac{v}{c}\right)^{k}\right) \quad (2)$$

Where $W(v;k,c)$ represents the likelihood of wind speed occurring at a specific value, showing how wind speeds are distributed over the random variable v (e.g., time, measurement). To estimate scale and shape parameters, different methods have been developed. The following methods are utilized in our study.

2.1. Method of Moments (MoM):

This method utilizes the mean and variance of the data to estimate the Weibull parameters [25]. The shape parameter k can be estimated by solving the following equation:

$$\sigma = c\left[\Gamma\left(1+\frac{2}{k}\right) - \Gamma^2\left(1+\frac{1}{k}\right)\right]^{\frac{1}{2}} \quad (3)$$

Where σ standard deviation of the wind speed data and Γ is the Gamma function. Once k is obtained, the scale parameter c is also calculated by using the following equation:

$$\bar{v} = c\Gamma\left(1+\frac{1}{k}\right) \quad (4)$$

2.2. Empirical Method (EM)

This method relies on empirical relationships derived from the mean and standard deviation of the wind speed data [26]. To estimate the shape parameter (k), the following empirical formula is used.

$$k = \left(\frac{\sigma}{\bar{v}}\right)^{-1.086} \quad (5)$$

Where, $\sigma / \bar{v} = C$, which is known as the coefficient of variation. Once k has been estimated, the scale parameter (c), also calculated through the relation:

$$c = \frac{\bar{v}}{\Gamma\left(1+\frac{1}{k}\right)} \quad (6)$$

We used Python to calculate Γ.

2.3. Maximum Likelihood Method (MLM)

The MLM estimates the parameters k and c by maximizing the likelihood function [27]. The optimization conditions can be used to find the values of k and c.

$$k = \left[\frac{\sum_{i=1}^{n} f_i v_i^k ln(v_i)}{\sum_{i=1}^{n} v_i^k} - \frac{\sum_{i=1}^{n} f_i l\, n(v_i)}{\sum_{i=1}^{n} f_i}\right]^{-1} \quad (7)$$

$$c = \left(\frac{1}{\sum_{i=1}^{n} f_i}\sum_{i=1}^{n} f_i v_i^k\right) \quad (8)$$

Where f_i represents the frequency or number of observations (e.g., recorded wind speed occurrences) in the i^{th} bin or interval.

2.4. Least Squares Method (LSM)

The least squares method is used by minimizing the square difference between recorded and fitted values [28]. It is an iterative method; the iteration stops once the termination criteria are reached. Python built-in library for least square fit was used to model the Weibull distribution. The program finds the new values of the probability distribution p (predicted) and compares them with the corresponding known values p (recorded). The sum of squares errors is calculated by the following formula.

$$SSE = \Sigma\{p(recorded) - p(predicted)\}^2 \quad (9)$$

The program determines the scale and shape parameters by minimizing SSE.

2.5. Neural Network Architecture

The Artificial Neural Network method is a machine learning technique that discovers the hidden relationship between an output variable and a set of input variables. It works on a pattern like the way our brain. It makes use of neurons that link output and

input variables through one or more hidden values in a hidden layer between the output and input variables [29]. In ANN methods, the data is divided into three parts; the main part consists of more than 50% of the data is used to train the network. Once the network is trained, the second part of the data is used for testing the trained network. Finally, the last part of the data is used to validate the network. An overall check is also carried out on the complete set of data. The goodness of the network is measured by a couple of statistics: the correlation coefficient, the Root Mean Square Error, and the Performance of the network. If the correlation coefficient in training, testing, validation, and overall check is significant, the network is considered reliable; further reliability check is done with the lowest value of RMSE, and performance coefficient.

In general, there are three layers, known as input, hidden, and output layers. The data is fed into input layers having one or more input parameters, and the values in the hidden layer are generated using random weights and input values fed to an activation function. The hidden layer then generates output values using an activation function. A comparison is made between generated output and recorded output; if the difference is insignificant, the network is considered as trained; otherwise, a backward feedback error analysis generates new weights in the input layer for new values generated for the hidden layer. The process continues till the network is well-trained. The neurons in the hidden layer may be varied for optimized results.

In the present study, the input variables were Temperature and Humidity, whereas the output variable was wind speed. A hidden layer with 10 neurons was used to train the network. To notice the influence of the wind direction on the wind speed. The wind direction is also incorporated in the input parameters. A precursor network is also trained in this study with the same parameters. One of the four ANN networks is shown in Figure 1.

2.6. Wind Energy Potential

Wind energy potential mainly depends on the wind speed of the potential site; the other factors on which it depends are the area swept by the wings of the wind turbine and the air density of the location. The air density varies from site to site and depends on the altitude and air temperature. If A is the area swept by the rotors in (m^2), ρ is the air density in (kg m^{-3}), and v is the wind speed in (m s^{-1}), the power in watts is given by the following formula [30]:

$$P = \frac{1}{2} A \rho \int_0^\infty v^3 f(v) dv = \frac{1}{3} A \rho \overline{v^3} \qquad (10)$$

Here $\overline{v^3}$ is the average value of the cube of the wind speed. To make this power independent of the area of the rotors, we find fractional power or power density (average power per unit area in (watts m^{-2}) and is given by:

$$p = \frac{P}{A} = \frac{1}{2} \rho \overline{v^3} \qquad (11)$$

Wind potential for Karachi City for each month from January to December was calculated using the above formula.

2.7. Statistical Errors for Validation of Designed Models

The validity of designed models has been checked by the Mean Absolute Error (MAE), Root Mean Square Error (RMSE), Chi-Square Test (χ^2), and Kolmogorov-Smirnov (KS) Test are calculated by using Equations (12) to (15) [31].

$$MABE = \left(\frac{1}{n}\right) \Sigma |v_i - \hat{v}_i| \qquad (12)$$

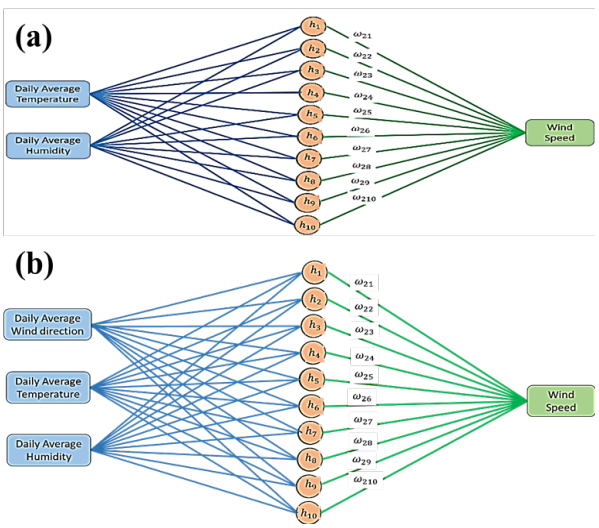

Fig. 1. The ANN architecture with (a)Temperature and Relative Humidity, (b) Temperature and Relative Humidity, and Wind direction in the input layer.

$$RMSE = \sqrt{\left[\left(\frac{1}{n}\right)\Sigma(v_i - \hat{v}_i)^2\right]} \quad (13)$$

$$\chi^2 = \Sigma\left[\frac{(f_i - \hat{f}_i)^2}{\hat{f}_i}\right] \quad (14)$$

and

$$KS = \max\left|F_i(v) - \hat{F}_i(v)\right| \quad (15)$$

3. RESULTS AND DISCUSSION

The demand for renewable energy has been increasing day by day. Different available Renewable potentials around the world have been exploited and harnessed to generate electricity. Wind is one of the renewable energies that has potential in almost every part of the world. Weibull distribution with two parameters is frequently used in modelling wind speed distributions. To estimate the parameters of the Weibull distribution, various techniques and methods have been developed. In this study, we used the method of least squares to calculate the parameters using a built-in Python function. A Python program was developed to carry out the calculations and to estimate the parameters. The built-in function works well if initial conditions are close to the real values of the distribution parameters, and the convergence becomes faster. To do so, we used the fact that most of the scale parameters are greater than 2, and the value of the shape parameter can be written as a function of the scale parameter. This formula was given as the input parameter.

The program also computes the parameters using the Method of Moments (MoM), the Empirical Method (EM), and the Maximum Likelihood Method (MLM) to compare the results. Table 1 gives the estimated values of the scale and shape parameters computed by these methods. Both the values of scale and shape parameters are higher for estimation by the least square method, except in one or two months. Hussain *et al.* [32] also studied the wind speed distribution of the coastal region of Karachi. They also used the maximum likelihood method for estimation of shape and scale parameters. The average value of the shape parameter for 10 m height wind data was 3.3; the corresponding average value in our study is 3.5. The PDF generated by the estimated values of the shape and scale parameters of the Weibull distribution is shown in Figures 2 and 3. The PDFs generated by the least square method are good representatives of wind speed distribution; these PDFs cover excellently the histograms generated by recorded wind speed data in almost all recorded data. In July, PDFs generated by all the methods coincide perfectly. Visually, it looks like the least method gives the best results. Now we have compared quantitatively the four different statistical errors that were computed to compare the performance of the methods used in this work for the calculations of the Weibull parameters and the generation of the PDF. Table 2 shows the values of errors (RMSE, MAE, Chi-Square, and Kolmogorov-Smirnov) from January to December. The least-square results give lower values of these statistical errors except for March, August, and October; however, the errors are not very far from each other. The Kolmogorov-Smirnov errors for the least square methods are lower except for March, August, and October.

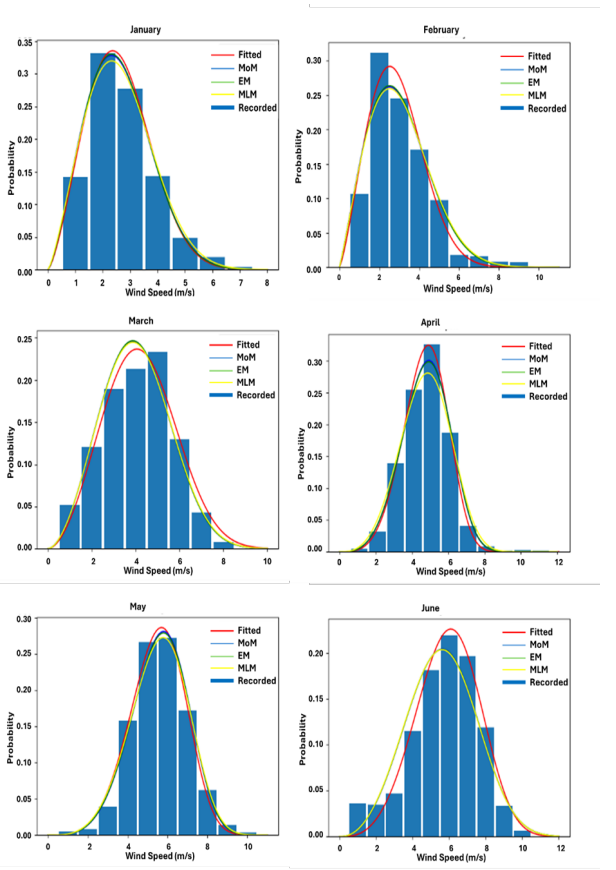

Fig. 2. Comparison of PDFs generated (Jan-June) with the determined values of shape and scale parameters using four estimation methods and the recorded wind speed distribution histogram.

Table 1. The shape and scale parameters of the Weibull distribution were calculated from four methods for January to December for Karachi city.

	k	c	k	c	k	c
	January		May		September	
Least square	2.4245	2.9378	4.5632	6.0117	5.3670	5.7775
MoM	2.3514	2.9291	4.5586	6.1212	5.4234	5.8488
EM	2.3661	2.9288	4.5253	6.1238	5.3751	5.8518
MLM	2.3110	2.9688	4.4140	6.1210	5.2400	5.8533
	February		June		October	
Least square	2.2954	3.2365	3.8950	6.5716	3.0384	4.2200
MoM	2.1081	3.3881	3.3063	6.2710	2.9189	4.0384
EM	2.1273	3.3882	3.3037	6.2712	2.9257	4.0380
MLM	2.1030	3.4152	3.2930	6.2634	2.9170	4.0502
	March		July		November	
Least square	2.8366	4.7310	4.9434	5.8680	2.3856	2.9270
MoM	2.8108	4.5184	4.9640	5.8698	2.4324	2.8296
EM	2.8195	4.5178	4.9229	5.8726	2.4437	2.8293
MLM	2.8040	4.5309	4.9460	5.8717	2.3910	2.8750
	April		August		December	
Least square	4.4608	5.1896	5.1021	5.2883	2.2782	2.8058
MoM	4.1712	5.2582	4.5405	5.2244	2.3243	2.7144
EM	4.1413	5.2604	4.5035	5.2269	2.3394	2.7141
MLM	3.8750	5.2578	4.5160	5.2252	2.3000	2.7599

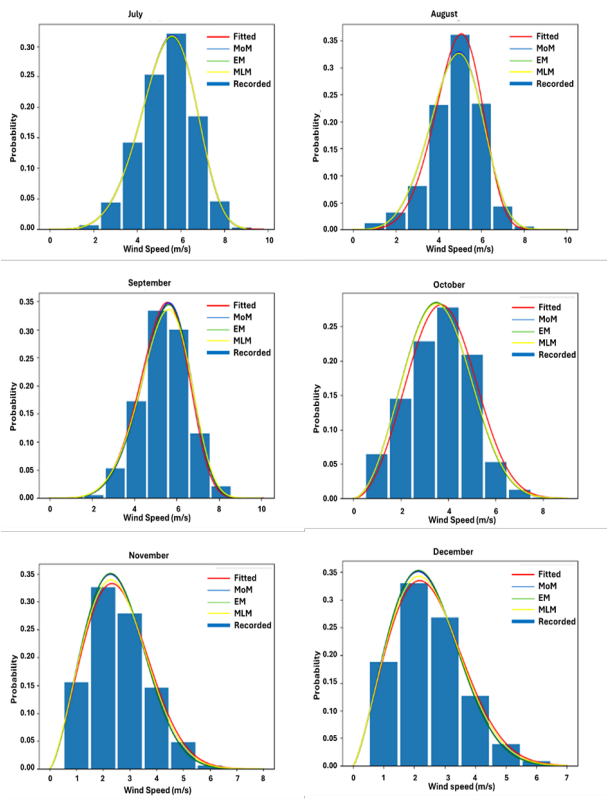

Fig. 3. Comparison of PDFs generated (July-Dec) with the determined values of shape and scale parameters using four estimation methods and the recorded wind speed distribution histogram.

Figure 4 shows the monthly wind potential for Karachi City. The wind potential was calculated using equation 11, for Karachi from January to December. The wind potential is maximum for June. From April to September, the wind speed is relatively high, so the wind potential is reasonably good for these months. In the months from October to March, wind speed is relatively low, so the wind potential compared to other months is low.

Wind modelling was done by many researchers in different studies by considering different meteorological parameters as input, but the wind direction was not considered in wind

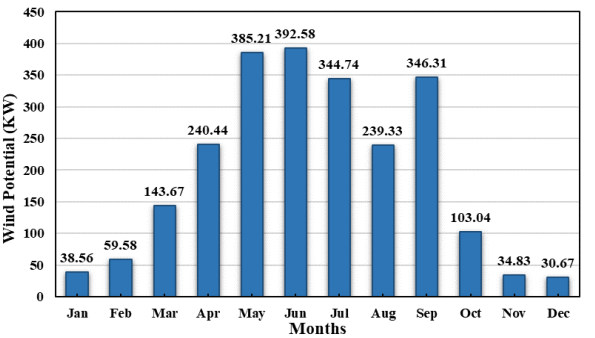

Fig. 4. Monthly wind potential in KW for Karachi city.

speed modelling. However, some researchers have used wind direction for wind energy analysis. Carta *et al.* [31] developed a joint probability distribution based on wind speed and wind direction for wind energy analysis [33]. Wang and Liu [34] used a finite mixture statistical distribution to assess wind energy potential using wind speed and wind direction data. They used a von Mises mixture distribution with various parameters for wind direction. Narain *et al.* [35] used the wake effect of wind turbines to investigate the effect of wind direction on wind energy potential. Mata *et al.* [36] studied the effect of wind direction on wind power output; they used three models for wind potential exploitation based on wind speed and wind direction shear. Models were based on blade elements and actuator disc representations.

We used an Artificial Neural Network to comprehend the effect of wind direction. We proposed two methods, one with temperature and humidity as input, and the second one as a precursor method. In each of the two methods, we further assessed each method with and without wind direction. All together four different ANN architectures were investigated in this work.

First, we consider the ANN architecture in which we modeled the wind speed distribution using temperature and moisture as input parameters. The results of the modelling are shown in the Figures. 5 and 6. Figure 5 depicts the regression analysis of the training, testing, validation, and overall performance of the model. Our results are not very promising as each R is less than 80%. Figure 6 portrays the comparison of the input wind speed distribution and the output generated by the ANN model. The conclusion made in Figure 5 is also verified by Figure 6; the overlap is not favorable. Ghorbani *et al.* [37] also used ANN to model wind speed distribution for Tabriz, Iran. The input parameters in ANN were Air temperature, air pressure, relative humidity, and precipitation. They used three different models having n, 2n, and 2n+1 neurons in the hidden layer. The coefficient of correlation for each of these models was above 95%. The wind pattern in Karachi does not show such promising results.

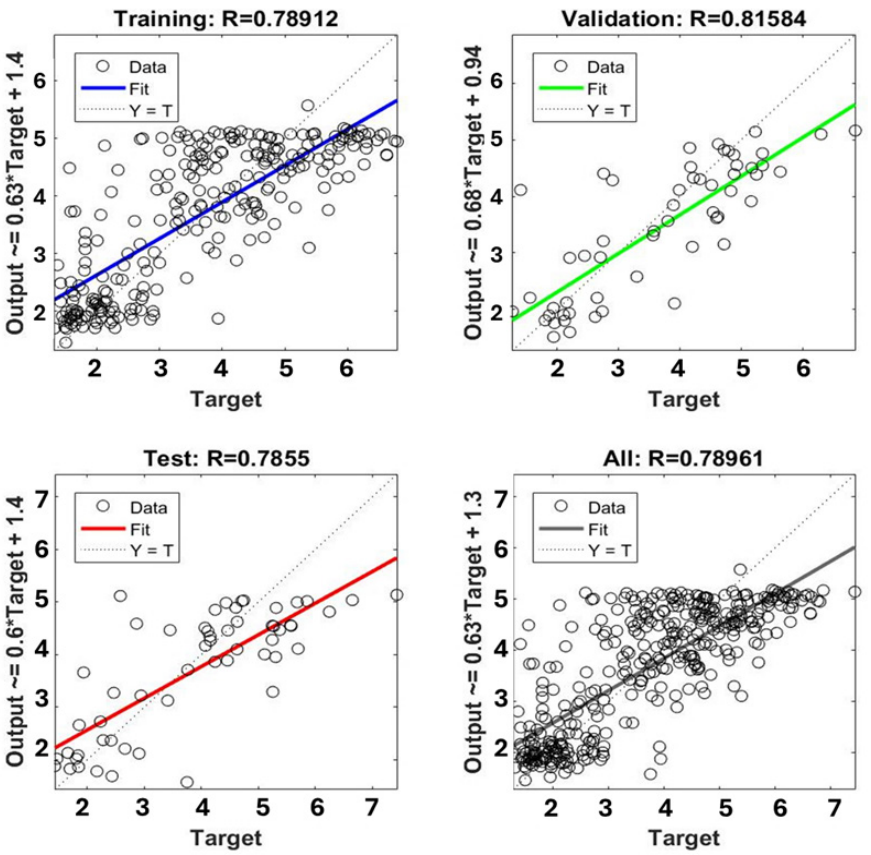

Fig. 5. Regression analysis of Testing, training, validation, and overall wind speed output, the input parameters are daily average temperature and relative humidity.

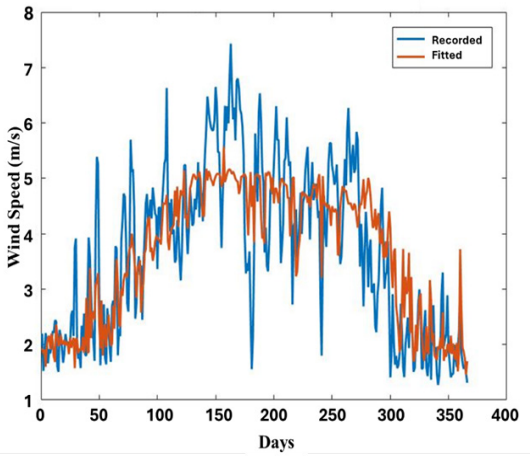

Fig. 6. Comparison of recorded and ANN modelled wind distributions by using daily temperature and relative humidity.

To investigate the impact of the wind direction in the ANN modelling, we added wind direction to the input parameters of the previous model. Figure 7 furnishes the R (correlation) values between the training (0.894), the test (0.839), and the validation phases (0.854). Figure 7 depicts a stronger correlation between the predicted and observed wind speeds compared to the previous model (R = 0.785-0.816). Figure 8 illustrates similar results as shown in Figure 4, i.e., the comparison of recorded and modeled values of wind speed. The overlapping of recorded and modeled values is relatively better in Figure 8 compared to that in Figure 6 and demonstrates optimized modelling results due to wind direction incorporation in the list of input parameters.

In the second ANN architecture, we employed precursor values of temperature and Humidity to predict wind speed. The model's performance shows a moderate correlation during training, testing, and validation phases, with an overall correlation of R = 0.798. However, the test and validation metrics reveal relatively weaker performance, with R = 0.702 for testing and R = 0.670 for validation, as illustrated in Figure 9, indicating that this network underperforms compared to earlier models. Figure 10 further authenticates the results shown in Figure 9. Figure 10 shows the comparison of the input

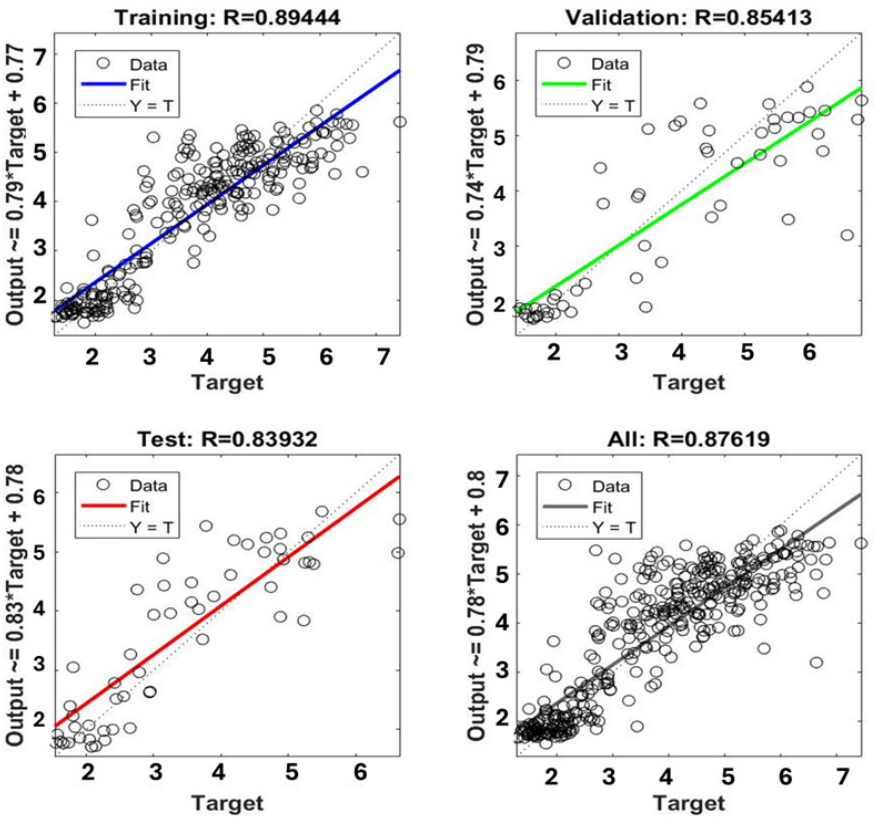

Fig. 7. Regression analysis of testing, training, validation, and overall wind speed output; the input parameters are daily average temperature, relative humidity, and wind direction.

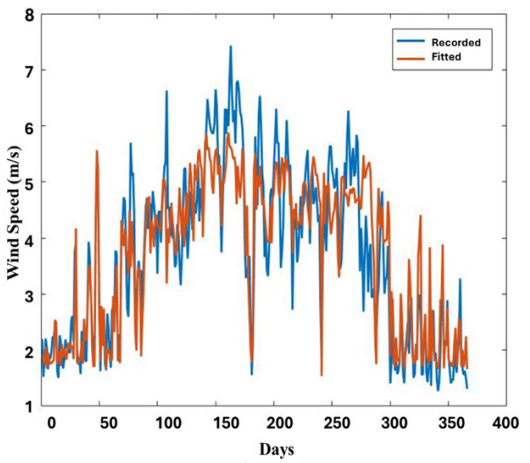

Fig. 8. Comparison of recorded and ANN modelled wind distributions by using daily temperature, relative humidity, and wind direction.

wind speed distribution and the output generated by the ANN model. Again, the results are not very promising as each R is less than 80%. The conclusion made in Figure 9 is also verified by Figure 10. Jamil and Zeeshan [38] studied wind speed modelling for wind speed data of Gujarat, India, using ANN. They also used precursor values of wind speed to predict current wind speed. The coefficient of correlation between predicted and recorded values of wind speed was found to be above 98%. Again, the wind speed pattern of Karachi does not show such high values for the correlation coefficient.

In the second case, the influence of wind direction in precursor modelling is depicted in Figures 11 and 10. We incorporated wind direction in the input list of the previous model. Figure 11 shows the R values for the training (R = 0.837), testing (R = 0.807), and validation (R = 0.803). This attests to a significant improvement in the correlation by the inception of wind direction in the input parameters. Figure 12 illustrates the comparison of recorded and modeled values of wind speed. By comparing Figures 10 and 12, it is obvious that the overlapping of recorded and modeled values is exceptionally better than in Figure 10. It further elucidates the improvement in the results due to the inclusion of wind direction in the list of input parameters.

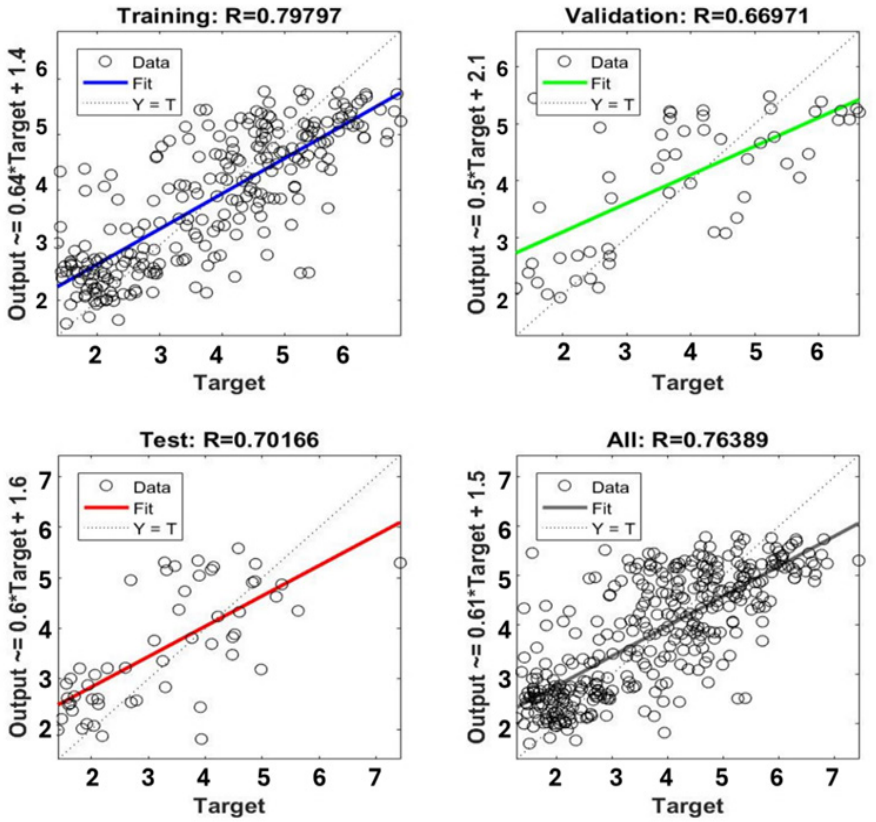

Fig. 9. Regression analysis of Testing, training, validation, and overall wind speed output, the input parameters are precursor values of daily average temperature and relative humidity.

The two cases scrutinized above for wind modelling with and without wind direction ascertain that wind direction is an important input parameter for wind speed forecasting. The addition of wind direction mitigates the Root Mean Square error and augments the performance of the modelling (see Table 2). Li and Shi [39] compared three different ANN models that are used to predict the wind speed of two sites in North Dakota. They used Back Propagation NN, Adaptive Linear Element NN, and Radial Basis Function NN. The RMSE values in the prediction of wind speed using three ANN models

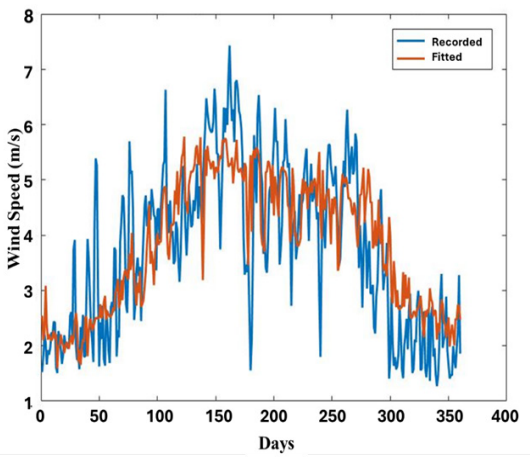

Fig. 10. Comparison of recorded and ANN modelled wind distributions by using precursor values of daily temperature and relative humidity.

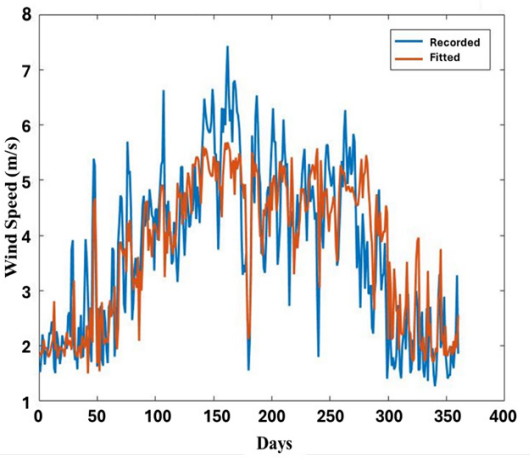

Fig. 12. Comparison of recorded and ANN modelled wind distributions, precursor values of daily temperature, relative humidity, and wind direction.

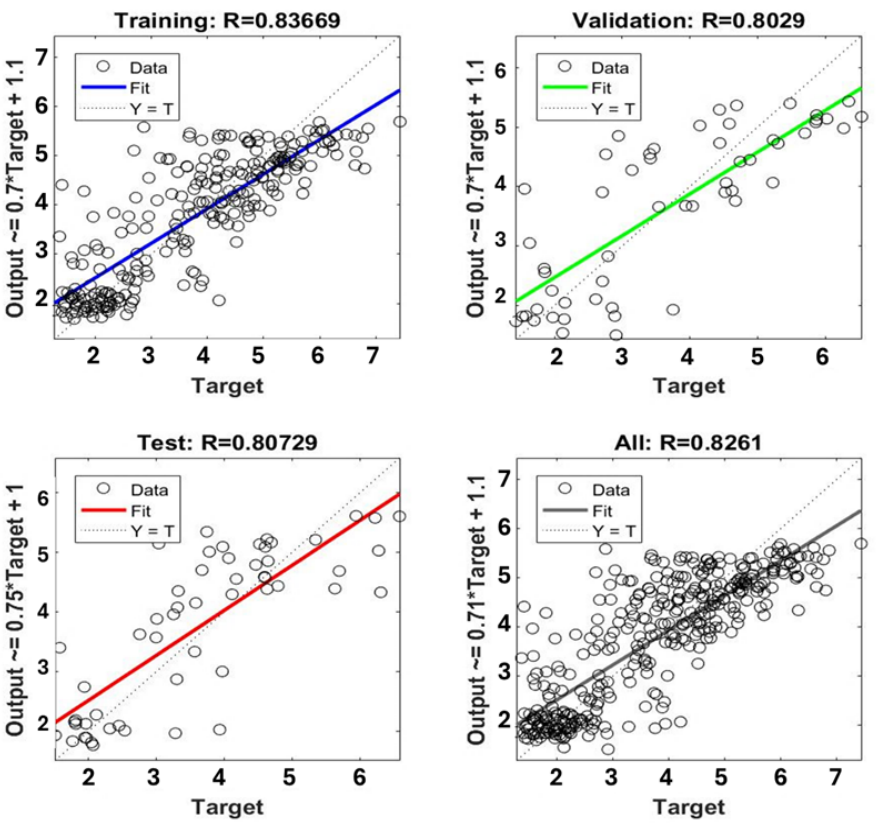

Fig. 11. Regression analysis of Testing, training, validation, and overall wind speed output. The input parameters are precursor values of daily average temperature, relative humidity, and wind direction.

Table 2. Four statistical errors were calculated in the PDFs generated by the shape and scale parameters of four estimation methods.

		Least square	MoM	EM	MLM			Least square	MoM	EM	MLM
January	RMSE	0.084	0.083	0.083	0.085	July	RMSE	0.07	0.07	0.071	0.07
	MABE	0.076	0.077	0.077	0.078		MABE	0.047	0.046	0.047	0.047
	Chi	0.082	0.076	0.078	0.072		Chi	0.088	0.091	0.085	0.088
	Kolmo-S	0.142	0.142	0.142	0.142		Kolmo-S	0.176	0.172	0.18	0.176
February	RMSE	0.073	0.095	0.093	0.096	August	RMSE	0.072	0.049	0.052	0.051
	MABE	0.05	0.054	0.053	0.054		MABE	0.058	0.041	0.042	0.041
	Chi	0.05	0.047	0.046	0.047		Chi	1.251	0.511	0.479	0.49
	Kolmo-S	0.15	0.27	0.261	0.277		Kolmo-S	0.13	0.091	0.106	0.101
March	RMSE	0.141	0.132	0.132	0.132	September	RMSE	0.057	0.06	0.058	0.051
	MABE	0.084	0.078	0.078	0.078		MABE	0.043	0.045	0.044	0.038
	Chi	0.133	0.127	0.128	0.127		Chi	0.289	0.306	0.28	0.219
	Kolmo-S	0.405	0.379	0.379	0.38		Kolmo-S	0.128	0.14	0.132	0.102
April	RMSE	0.058	0.068	0.069	0.073	October	RMSE	0.108	0.102	0.102	0.103
	MABE	0.039	0.04	0.04	0.041		MABE	0.072	0.065	0.065	0.065
	Chi	0.075	0.049	0.047	0.036		Chi	0.151	0.145	0.146	0.143
	Kolmo-S	0.129	0.207	0.212	0.225		Kolmo-S	0.282	0.278	0.277	0.279
May	RMSE	0.076	0.078	0.082	0.096	November	RMSE	0.085	0.084	0.085	0.084
	MABE	0.05	0.051	0.054	0.06		MABE	0.078	0.076	0.076	0.077
	Chi	0.036	0.037	0.041	0.057		Chi	1.501	1.821	1.85	1.62
	Kolmo-S	0.162	0.166	0.185	0.25		Kolmo-S	0.156	0.156	0.156	0.156
June	RMSE	0.161	0.19	0.191	0.193	December	RMSE	0.079	0.078	0.078	0.078
	MABE	0.092	0.121	0.121	0.122		MABE	0.073	0.072	0.072	0.072
	Chi	0.217	0.573	0.578	0.596		Chi	0.143	0.168	0.171	0.155
	Kolmo-S	0.497	0.508	0.51	0.521		Kolmo-S	0.142	0.142	0.142	0.142

were more than 1.25 in each case. However, the four different ANN architectures in this study show RMSE values between 0.72 and 0.96.

Table 3 quantifies the RMSE and performance values between different input configurations for wind speed prediction, reinforcing the critical role of wind direction in enhancing model accuracy. Notably, incorporating wind direction consistently reduces Mean Squared Error (MSE), a key indicator of prediction error, across both precursor-inclusive and precursor-exclusive models. For instance, without precursors, adding wind direction (T, H & D) lowers MSE by 21.5% (from 0.9204 to 0.7224). With precursors, including wind direction (T, H, D & Precursor), reduces MSE by 12.9% compared to the precursor-only model (from 0.9633 to 0.8388). Table 4 shows the statistical testing and respective significance level.

Table 3. Comparison of various ANN architectures.

Wind forecasting by	RMSE	Performance
Temperature & humidity	0.9204	0.8471
Temperature, humidity & wind direction	0.7224	0.5218
Precursor values of (Temperature & humidity)	0.9633	0.9280
Precursor values of Temperature, humidity) & wind direction	0.8388	0.7035

Table 4. Statistical testing and significance.

Dataset 1 Statistics		**Dataset 2 Statistics**	
Count	360	Count	360
Mean	3.7208	Mean	3.7264
Standard Deviation	1.2107	Standard Deviation	1.4881
Variance	1.4659	Variance	2.2145
T-Test results			
Difference Between Mean	-0.0057		
T-Statistics	-0.0561		
Degree of Freedom	718		
P-Value	0.1329		
Interpretation	The difference between means is not statistically significant ($p \geq 0.05$)		

4. CONCLUSIONS

A systematic investigation has been carried out to observe the impact of wind direction on wind speed modelling. The ANN was employed in modelling wind speed with two input parameters (temperature and humidity). In the second case, the precursor values of the input parameters were employed to forecast the current value of the wind speed. In the next step, input parameters were appended by an additional parameter, i.e., wind direction. In both cases, it was found that the results of ANN for training, testing, validation, and overall are significantly improved by the addition of wind direction with parameters temperature and humidity. Figures 7 and 11 depict the improved values of the correlation coefficient for all the categories. The best network in the forecasting of wind speed with three parameters (temperature, humidity, and wind direction) yields all correlation coefficients above 80%. This network has the lowest RMSE and improved performance. Wind speed is also modeled using the Weibull distribution. To find the scale and shape parameters, the least squares method is used with Python's built-in function. A Python program was developed to implement the algorithm, the program also computes both the parameters using three existing methods (method of moments, empirical method, and maximum likelihood method) to compare the result of the least square method. The modelling was carried out for each month of the year 2016, and in most of the months, the RMSE and Kolmogorov-Smirnov test values were optimized for the least square method. The PDFs drawn by the estimated values of shape and scale parameters for the four methods elucidate that the least square method's PDF explains well the histogram generated by the recorded values of wind speed. We conclude that the least square method using Python's built-in function gives reliable results for wind speed modelling. The addition of wind direction in the input parameters to forecast improves the ANN results.

5. CONFLICT OF INTEREST

The authors declare that there is no conflict of interest to submit/publish this research.

6. REFERENCES

1. Z. Elahi, W. Gull, and Z. Uddin. Weibull distribution parameter estimation using spreadsheets. *Spreadsheets in Education* 1: 1-12 (2023). https://sie.scholasticahq.com/article/72617
2. M. Zahid, A. Rajput, S. Rehman, M. Adeel, and Z. Uddin. A computer package to model wind speed distribution using six different methods including maximum entropy principle. *International Journal of Energy* 45(3-4): 207-218 (2024).
3. J.K. Khan, M. Shoaib, Z. Uddin, I.A. Siddiqui, A. Aijaz, A.A. Siddiqui, and E. Hussain. Comparison of wind energy potential for coastal locations: Pasni and Gwadar. *Journal of Basic & Applied Sciences* 11: 211-216 (2015).
4. J.K. Khan, F. Ahmed, Z. Uddin, S.T. Iqbal, S.U. Jilani, A.A. Siddiqui, and A. Aijaz. Determination of Weibull parameter by four numerical methods and prediction of wind speed in Jiwani (Balochistan). *Journal of Basic & Applied Sciences* 11: 62-68 (2015).
5. J.K. Khan, Z. Uddin, I.S. Tanweer, F. Ahmed, A. Aijaz, and S.U. Jilani. An analysis of wind speed distribution and comparison of five numerical

methods for estimating Weibull parameters at Ormara, Pakistan. *European Academic Research* II (11): 14007-14015 (2015).
6. Z. Uddin, and N. Sadiq. Method of quartile for determination of Weibull parameters and assessment of wind potential. *Kuwait Journal of Science* 50(3A): 105-119 (2023).
7. A.A. Rajput, M. Daniyal, M.M. Zahid, H. Nafees, M. Shafi, and Z. Uddin. New approach to calculate Weibull parameters and comparison of wind potential of five cities of Pakistan. *Advances in Energy Research* 8(2): 95 (2022).
8. S.U. Rehman, N. Sadiq, I. Tariq, M.M. Khan, M.M. Zahid, A.A. Rajput, and Z. Uddin. A new mathematical technique and its Python program to assess wind potential. *Beni-Suef University Journal of Basic and Applied Sciences* 13(1): 61 (2024).
9. Z. Uddin, M. B. Khan, M.H., Zaheer, W. Ahmad, and M.A., Qureshi. An alternate method of evaluating Lagrange multipliers of MEP. *SN Applied Sciences* 1: 224 (2019).
10. N. Sadiq. Seasonal and continual wind speed modelling for the coastal urban city, Karachi. *MAUSAM* 69(2): 289-296 (2018).
11. M.A. Ghorbani, R. Khatibi, M.H. FazeliFard, L. Naghipour, and O. Makarynskyy. Short-term wind speed predictions with machine learning techniques. *Meteorology and Atmospheric Physics* 128: 57-72 (2016).
12. H. Demolli, A.S. Dokuz, A. Ecemis and M. Gokcek. Wind power forecasting based on daily wind speed data using machine learning algorithms. *Energy Conversion and Management* 198: 111823 (2019).
13. Q. Zhu, J. Chen, L. Zhu, X. Duan, and Y. Liu. Wind speed prediction with spatio–temporal correlation: A deep learning approach. *Energies* 11(4): 705 (2018).
14. S.H. Hur. Short-term wind speed prediction using Extended Kalman filter and machine learning. *Energy Reports* 7: 1046-1054 (2021).
15. R. Li and Y. Jin. A wind speed interval prediction system based on multi-objective optimization for machine learning method. *Applied Energy* 228: 2207-2220 (2018).
16. B.M.A. Ehsan, F. Begum, S.J. Ilham, and R.S. Khan. Advanced wind speed prediction using convective weather variables through machine learning application. *Applied Computing and Geosciences* 1: 100002 (2019).
17. Y.S. Türkan, H.Y. Aydoğmuş, and H. Erdal. The prediction of the wind speed at different heights by machine learning methods. *An International Journal of Optimization and Control: Theories & Applications (IJOCTA)* 6(2): 179-187 (2016).
18. M.S. Hanoon, A.N. Ahmed, P. Kumar, A. Razzaq, N.A. Zaini, Y.F. Huang, M. Sherif, A. Sefelnasr, K.W. Chau, and A. El-Shafie. Wind speed prediction over Malaysia using various machine learning models: potential renewable energy source. *Engineering Applications of Computational Fluid Mechanics* 16(1): 1673-1689 (2022).
19. Y. Han, L. Mi, L. Shen, C. S. Cai, Y. Liu, K. Li, and G. Xu. A short-term wind speed prediction method utilizing novel hybrid deep learning algorithms to correct numerical weather forecasting. *Applied Energy* 312: 118777 (2022).
20. E. Cadenas and W. Rivera. Short-term wind speed forecasting in La Venta, Oaxaca, México, using artificial neural networks. *Renewable Energy* 35(1): 274-278 (2010).
21. A.M. Foley, P.G. Leahy, A. Marvuglia, and E.J. McKeogh. Current methods and advances in forecasting of wind power generation. *Renewable Energy* 37(1): 1-8 (2012).
22. M. Lydia, S.S. Kumar, A.I. Selvakumar, and E.P. Kumar. Linear and non-linear autoregressive models for short-term wind speed forecasting. *Energy Conversion and Management* 112: 115-124 (2016).
23. H. Liu, H.Q. Tian, and Y.F. Li. Comparison of two new ARIMA-ANN and ARIMA-Kalman hybrid methods for wind speed prediction. *Applied Energy* 98: 415-424 (2015).
24. W. Qamar, M. Hussain, M.B. Zaheer, J. Akram, N. Sadiq, and Z. Uddin. Prediction of sunspot numbers via Weibull distribution and deep learning. *Astrophysics and Space Science* 370(7): 68 (2025).
25. J. Merganič and H. Sterba. Characterisation of diameter distribution using the Weibull function: method of moments. *European Journal of Forest Research* 125(4): 427-439 (2006).
26. K. Mohammadi, O. Alavi, A. Mostafaeipour, N. Goudarzi, and M. Jalilvand. Assessing different parameters estimation methods of Weibull distribution to compute wind power density. *Energy Conversion and Management* 108: 322-335 (2016).
27. W.L. Hung and Y.C. Liu. Estimation of Weibull parameters using a fuzzy least-squares method. *International Journal of Uncertainty, Fuzziness and Knowledge-Based Systems* 12(05): 701-711 (2004).
28. P. Malik, A. Gehlot, R. Singh, L. R. Gupta, and A.K. Thakur. A review on ANN based model for solar radiation and wind speed prediction with real-time data. *Archives of Computational Methods in*

Engineering 29(5): 3183-3201 (2022).
29. A. Tahir, M. Ashraf, A. Razzak, S.M. Raza, and Z. Uddin. Temperature data of Hyderabad from the temperature of three neighboring cities using the ANN and the multiple regression methods. *Kuwait Journal of Science* 50(3A): 147-161 (2023).
30. W. Shepherd and L. Zhang (Eds.). Electricity Generation Using Wind Power. *World Scientific* (2017).
31. J.A. Carta, P. Ramirez, and C. Bueno. A joint probability density function of wind speed and direction for wind energy analysis. *Energy Conversion and Management* 49(6): 1309-1320 (2008).
32. M. A. Hussain, S. Abbas, M.R.K. Ansari, A. Zaffar, and B. Jan. Wind speed analysis of some coastal areas near Karachi. *Proceedings of the Pakistan Academy of Sciences* 51(1): 83-91 (2012).
33. M. Arashi, P. Nagar, and A. Bekker. Joint probabilistic modeling of wind speed and wind direction for wind energy analysis: A case study in humansdorp and noupoort. *Sustainability* 12(11): 4371 (2020).
34. Z. Wang and W. Liu. Wind energy potential assessment based on wind speed, its direction and power data. *Scientific Reports* 11(1): 16879 (2021).
35. A. Narain, S.K. Srivastava, and S.N. Singh. The impact of wind direction on wind farm power output calculation considering the wake effects of wind turbines. *Wind Engineering* 47(1): 74-85 (2023).
36. S.A. Mata, J.P. Martínez, J.B. Quesada, F.P. Larrañaga, N. Yadav, J.S. Chawla, V. Sivaram, and M.F. Howland. Modeling the effect of wind speed and direction shear on utility-scale wind turbine power production. *Wind Energy* 27(9): 873-899 (2024).
37. M.A. Ghorbani, R. Khatibi, B. Hosseini, and M. Bilgili. Relative importance of parameters affecting wind speed prediction using artificial neural networks. *Theoretical and Applied Climatology* 114(1): 107-114 (2013).
38. M. Jamil and M. Zeeshan. A comparative analysis of ANN and chaotic approach-based wind speed prediction in India. *Neural Computing and Applications* 31(10): 6807-6819 (2019).
39. G. Li and J. Shi. On comparing three artificial neural networks for wind speed forecasting. *Applied Energy* 87(7): 2313-2320 (2010).

Proceedings of the Pakistan Academy of Sciences: A Physical and Computational Sciences 62(3): 263-270 (2025)

ISSN (Print): 2518-4245; ISSN (Online): 2518-4253
http://doi.org/10.53560/PPASA(62-3)700

Pakistan Academy of Sciences

Research Article

Fekete-Szegö Inequality and Radius Estimate for Certain Subclasses of Analytic Functions of Complex Order Associated with the Sine Function

Aijaz Ahmed Bhatti[1*], Abdul Wasim Shaikh[1], Shujaat Ali Shah[2], and Sulaiman Awwal Akinwunmi[3]

[1]Institute of Mathematics and Computer Science, University of Sindh, Jamshoro, Pakistan
[2]Department of Mathematics and Statistics, Quaid-e-Awam University of Engineering, Science and Technology, Nawabshah, Pakistan
[3]Department of Mathematics and Statistics, Federal University of Kashere, Gombe, Nigeria

Abstract: In the present work, using suboridination techniques, we study certain subclasses of analytic univalent functions of complex order γ associated with the sine function. The sharp coefficient bounds and the sharp Fekete-Szegö inequality are obtained for these subclasses. Additionally, a sharp radius result is also derived for a certain subclass of Janowski starlike functions. These results generalize several known results as special cases and contribute to the broader theory of univalent functions.

Keywords: Analytic Functions, Coefficient Bounds, Fekete-Szegö Problem, Radius Problem, Sine Function, Subordination.

1. INTRODUCTION

In Geometric function theory (GFT) analytic functions and their geometric properties are regarded as core concepts. A key area of study within GFT is the class of univalent functions, which encompasses analytic functions. Many fields of mathematics and physics, including potential theory, fluid dynamics, and conformal mappings, rely heavily on these functions. where they are utilized to map the open unit disk onto domains with specific geometric structures [1]. Aleman and Constantin [2] proposed a significant connection between fluid dynamics and the theory of univalent functions. Specifically, the authors presented a straightforward technique that demonstrates how to explicitly solve the incompressible two-dimensional Euler equations using a univalent harmonic map. For the fundamental theory of univalent functions and a thorough understanding of the foundational concepts and key discoveries in the field, we direct the reader to previous studies [1, 3-5]. We will now review some fundamental definitions that are already familiar.

Let $\mathfrak{A}$ represent the family of analytic functions f defined in the open unit disk $\mathfrak{E} = \{\psi \in \mathbb{C}: |\psi| < 1\}$ that satisfying $f(0) = 0$, $f'(0) = 1$ and admit the following power series expansion:

$$f(\psi) = \psi + \sum_{n=2}^{\infty} a_n \psi^n. \tag{1}$$

A function $f \in \mathfrak{A}$ is said to be univalent in $\mathfrak{E}$ if it maps distinct points in $\mathfrak{E}$ to distinct points in its image, i.e., $f(\psi_1) = f(\psi_2)$ implies $\psi_1 = \psi_2$ for $\psi_1, \psi_2 \in \mathfrak{E}$. The class of all such univalent functions is denoted by $\mathcal{S}$. It is evident that an analytical function u for which $u(0) = 0$ and $|u(\psi)| < 1$ is called Schwartz function. Let g_1

Received: July 2025; Revised: August 2025; Accepted: September 2025
* Corresponding Author: Aijaz Ahmed Bhatti <aijaz.bhatti@usindh.edu.pk>

and g_2 be analytic in $\mathfrak{E}$. Then g_1 is subordinate to g_2, written as $g_1 \prec g_2$, if there exists a Schwartz function u, such that $g_1(\psi) = g_2(u(\psi))$.

Several important subclasses of univalent functions have been introduced and studied, from which the classes S^* and C, consisting of starlike and convex univalent functions respectively, are considered as the most extensively investigated subclasses of the class S of univalent functions in the open unit disk $\mathfrak{E} = \{\psi \in \mathbb{C}: |\psi| < 1\}$, and have been of major interest. Ma and Minda [6] introduced a class of analytic and univalent functions $\varphi(\psi)$ and proposed the following subclasses of analytic functions.

$$S^*(\varphi) = \left\{ f \in \mathfrak{A}: \frac{\psi f'(\psi)}{f(\psi)} \prec \varphi(\psi) \right\}, \qquad (2)$$

and

$$C(\varphi) = \left\{ f \in: \mathfrak{A}\ 1 + \frac{\psi f''(\psi)}{f'(\psi)} \prec \varphi(\psi) \right\}. \qquad (3)$$

Where $\varphi(\psi)$ is a univalent function with $\varphi(0) = 1$, $\varphi'(0) > 1$ and the region $\varphi(\mathfrak{E})$ is symmetric with respect to the real axis and star-shaped around the point $\varphi(0) = 1$.

An extension of equations (2) and (3), respectively, was provided by Ravichandran *et al.* [7], as follows:

$$S^*(\gamma, \varphi) = \left\{ f \in \mathfrak{A}: 1 + \frac{1}{\gamma}\left(\frac{\psi f'(\psi)}{f(\psi)} - 1\right) \prec \varphi(\psi) \right\},$$

and

$$C(\gamma, \varphi) = \left\{ f \in \mathfrak{A}: 1 + \frac{1}{\gamma}\left(\frac{\psi f''(\psi)}{f'(\psi)}\right) \prec \varphi(\psi) \right\}.$$

where $\gamma \in \mathbb{C} \setminus \{0\}$. Such functions are commonly referred to as Ma–Minda type functions of order γ , $(\gamma \in \mathbb{C} \setminus \{0\})$.

A central focus in this area is the investigation of the coefficient bounds and related inequalities for various subclasses of S, including results involving the Fekete-Szegö functional $|a_3 - \lambda a_2^2|$, for $0 < \lambda < 1$ [8], and the radius problems. We now provide a brief review of these investigations.

Finding bounds for function coefficients is a central problem in GFT, as it governs growth and distortion properties. The second coefficient, for instance, controls growth and distortion. Reformulated as the task of estimating a_n, the coefficient problem has been among the most challenging in the field. In 1916, Bieberbach [9] conjectured that for $f \in S$and has the form, given in equation (1), then then $|a_n| \leq n$, $(n \geq 2)$. The conjecture was finally settled in 1985 by Louis de Branges [10] confirming it for all $n \geq 2$. The Fekete-Szegö problem is a classical coefficient problem that seeks sharp bounds for linear combinations of coefficients, typically $|a_3 - \lambda a_2^2|$, offering detailed information on the geometric characteristics of subclasses of univalent functions. Many studies have since focused on these problems; some recent contributions can be seen in previous studies [11-15].

Finally, attention is given to the radius problems, where the aim is to determine the maximal radius for which functions belonging to a particular subclass of S preserve specific geometric properties such as starlikeness or convexity. If we consider certain transformations or geometric conditions that fail to maintain univalence, such as those within the unit disk. It naturally leads to the question of whether such transformations or conditions may uphold univalence in a smaller subdisk

$$\mathfrak{E}_0 = \{\psi: |\psi| < R < 1\} \subset \mathfrak{E}.$$

Problems of this nature are commonly referred to as "radius problems". The radius, R, represents the largest subdisk, $\mathfrak{E}_0$ within which specific transformations of a univalent function f or certain geometric conditions ensure univalence. The radius problems ensure the validity of certain geometric properties (such as starlikeness or convexity) within a disk of maximal size [16].

A key tool in such investigations is the well-known Carathéodory class $\mathcal{P}$, consisting of analytic functions p in $\mathfrak{E}$, and has the following form:

$$p(\psi) = 1 + \sum_{n=1}^{\infty} c_n \psi^n; \ (\psi \in \mathfrak{E}). \qquad (4)$$

With $Re(p(\psi)) > 0$. A significant portion on coefficient problems involves expressing coefficients of functions in a given class in terms of those with positive real part, using known inequalities for $\mathcal{P}$ to analyze them. To unify and extend the study of these and related subclasses, Ma–Minda [6] form of analytic functions are used, which offers a unified approach to several subclasses

of analytic functions through subordination techniques.

By following unified approach presented by Ma and Minda [6], several authors in recent years have proposed new subclasses of the class $\mathcal{S}$ of univalent functions by selecting specific forms of the analytic function $\varphi(\psi)$. Examples of such choices for $\varphi(\psi)$ include: $S^*[A_1, A_2] = S^*\left(\frac{1+A_1\psi}{1+A_2\psi}\right)$, $-1 \leq A_2 < A_1 \leq 1$, is a widely studied the Janowski subclass of starlike functions [17], and the class of starlike function of order $\propto$ deonted by $S^*(\propto) = S^*\left(\frac{1+(1-2\propto)\psi}{1-\psi}\right), 0 \leq \propto < 1$. Similarly the class of Janowski convex functions and the class of convex function of order $\propto$,respectively expressed as $C[A_1, A_2] = C\left(\frac{1+A_1\psi}{1+A_2\psi}\right)$ and $C(\propto) = C\left(\frac{1+(1-2\propto)\psi}{1-\psi}\right)$ In particular, $S^*(0) = S^*$ and $C(0) = C$ are the classical classes of starlike and convex functions, respectively. Cho *et al*. [18] introduced the class S^*_{sin} of analytic functions, defined as follows:

$$S^*_{sin} = \left\{ f \in \mathfrak{A}: \frac{\psi f'(\psi)}{f(\psi)} \prec 1 + sin\psi;\ (\psi \in \mathfrak{E}) \right\}.$$

In their work, authors conducted a comprehensive study on various radius problems associated with the class S^*_{sin} of analytic functions. Their analysis includes determining sharp bounds for radii associated with geometric properties such as starlikeness and convexity. Further contributions to this class can be found in the work of Arif *et al.* [19], where the authors obtained sharp coefficient bounds, investigated the Fekete-Szegö inequality, and examined the Hankel determinant of order three. Additional geometric properties of functions in the class S^*_{sin}, along with recent related developments, are discussed by Srivastava *et al*. [20] and Tang *et al*. [21]. Recently, Al-Shaikh *et al.* [22] introduced a class of starlike functions of complex order γ, denoted by $\mathcal{L}(m, n, \propto, \gamma)$ where $-1 < n < m \leq 1$, $0 \leq \propto \leq 1$, and $\gamma \in \mathbb{C} \setminus \{0\}$. This class comprises functions $f \in \mathfrak{A}$ that satisfy the subordination condition as follows:

$$1 + \frac{1}{\gamma}\left(\frac{\psi f'(\psi) + \propto \psi^2 f''(\psi)}{(1-\propto) f(\psi) + \propto \psi f'(\psi)} - 1\right) \prec \varphi_{Car}(m, n; \psi),$$

where $\varphi_{Car}(m, n; \psi)$ defines a cardioid domain, given by:

$$\varphi_{Car}(m, n; \psi) = \frac{2m\tau^2\psi^2 + (m-1)\tau\psi + 2}{2n\tau^2\psi^2 + (n-1)\tau\psi + 2},$$

with $\tau = \frac{1-\sqrt{5}}{2}$, and $\psi \in \mathfrak{E}$.

2. PROPOSED WORK

Based on the earlier works of Cho *et al.* [18], Arif *et al.* [19], and Al-Shaikh *et al.* [22], the present investigation introduces a new subclass $\mathfrak{R}_{sin}(\propto, \gamma; \varphi_{sin})$ of analyic functions of complex order γ.

Definition 1. If a function $f \in \mathfrak{A}$ has the form given in (1), then it belongs to the subclass $\mathfrak{R}_{sin}(\propto, \gamma; \varphi_{sin})$, provided the following conditions are satisfied:

$$1 + \frac{1}{\gamma}\left\{\frac{\psi f'(\psi) + \propto \psi^2 f''(\psi)}{(1-\propto) f(\psi) + \propto \psi f'(\psi)} - 1\right\} \prec \varphi_{sin}(\psi),$$

for $0 \leq \propto \leq 1, \gamma \in \mathbb{C} \setminus \{0\}$ and $\varphi_{sin}(\psi) = 1 + sin\psi;\ (\psi \in \mathfrak{E})$.

Equivalently, $f \in \mathfrak{R}_{sin}(\propto, \gamma; \varphi_{sin})$ if the image of

$$1 + \frac{1}{\gamma}\left\{\frac{\psi f'(\psi) + \propto \psi^2 f''(\psi)}{(1-\propto) f(\psi) + \propto \psi f'(\psi)} - 1\right\},$$

lies within the eight-shaped region φ_{sin} located in the right half-plane (see Figure 1 reported by Cho *et al.* [18]). Several known and newly defined subclasses emerge as special cases of Definition 1 by choosing particular values of the parameters $\propto$ and γ, as illustrated below:

(i) $\mathfrak{R}_{sin}(0, \gamma; \varphi_{sin}) \equiv \mathfrak{S}^*_{sin}(\gamma; \psi)$: A new subclass of starlike functions characterized by a complex parameter γ, related to the sine function.
(ii) $\mathfrak{R}_{sin}(0,1; \varphi_{sin}) \equiv S^*_{sin}$: A subclass of starlike functions associated with the sine function introduced by Cho *et al.* [18].
(iii) $\mathfrak{R}_{sin}(1, \gamma; \varphi_{sin}) \equiv \mathfrak{C}_{sin}(\gamma; \psi)$: A new subclass of convex functions of complex γ linked with the sine function.
(iv) $\mathfrak{R}_{sin}(1,1; \varphi_{sin}) \equiv C_{sin}$: A subclass of convex functions associated with the sine function introduced by Arif *et al.* [19].

3. SET OF LEMMAS

We begin by stating the following auxiliary results, that will be employed in deriving the main results.

Lemma 1. If $p \in \mathcal{P}$ and has the form given in (1), then

$$|c_n| \leq 2 \text{ for } n \geq 1, \tag{5}$$

and for any $v \in \mathbb{C}$,

$$\left|c_2 - vc_1^2\right| \leq 2\, max\{1, |2v - 1|\}. \tag{6}$$

The relation in equation (5) can be found in previously reported literature [23]. The inequality stated in equation (6) was established by Keogh and Merkes [24] and related discussion is given by Ma and Minda [6].

Lemma 2. [25] Let, $p \in \mathcal{P}(\alpha)$. Then for $|\psi| = r$, we have

$$\left|\frac{\psi p'(\psi)}{p(\psi)}\right| \leq \frac{2(1-\alpha)nr^n}{(1-r^n)(1+(1-2\alpha)r^n)}.$$

Lemma 3. [18] Let $1 - sin1 \leq a \leq 1 + sin1$ and $r_a = sin1 - |a-1|$. The following hold.

$\{\mathcal{W} \in \mathbb{C}: |\mathcal{W} - a| < r_a\} \subset \delta_{sin} \subset \{\mathcal{W} \in \mathbb{C}: |\mathcal{W} - 1| < sin1\}$.

Where $\delta_{sin} = \varphi_{sin}(\mathfrak{E})$.

4. MAIN RESULTS

In this section, we investigate the sharp bounds for the first two coefficients and obtain sharp estimates for the Fekete-Szegö inequality for functions belonging to the class $\mathfrak{R}_{sin}(\alpha, \gamma; \varphi_{sin})$. Additionally, a sharp $\mathfrak{S}^*_{sin}(\gamma; \psi)$ −radius result is also derived for a certain subclass of Janowski starlike functions. Known subclasses and their corresponding results are also discussed to emphasize the connection between the present work and previous studies.

4.1. Coefficint Problems

Theorem 1. If the function $f \in \mathfrak{R}_{sin}(\alpha, \gamma; \varphi_{sin})$, and be given by equation (1). Then,

$$|a_2| \leq \frac{|\gamma|}{(1+\alpha)},$$

$$|a_3| \leq \frac{|\gamma|}{2(1+2\alpha)}(1 + |\gamma - 1|).$$

These findings are sharp.

Proof. If $f \in \mathfrak{R}_{sin}(\alpha, \gamma; \varphi_{sin})$, then by defintion we have:

$$1 + \frac{1}{\gamma}\left\{\frac{\psi f'(\psi) + \alpha\psi^2 f''(\psi)}{(1-\alpha)f(\psi) + \alpha\psi f'(\psi)} - 1\right\} = 1 + sin(u(\psi)), \quad (7)$$

where $u(\psi)$ is a Schwarz function. Let, p be a function such that:

$$p(\psi) = \frac{1+u(\psi)}{1-u(\psi)} = 1 + c_1\psi + c_2\psi^2 + c_3\psi^3 + \cdots, \quad (8)$$

then $p(\psi) \in \mathcal{P}$. It follows that:

$$u(\psi) = \frac{p(\psi)-1}{p(\psi)+1} = \frac{c_1\psi + c_2\psi^2 + c_3\psi^3 + \cdots}{2 + c_1\psi + c_2\psi^2 + c_3\psi^3 + \cdots}.$$

Using equation (7), we obtain:

$$1 + \frac{1}{\gamma}\left\{\frac{\psi f'(\psi) + \alpha\psi^2 f''(\psi)}{(1-\alpha)f(\psi) + \alpha\psi f'(\psi)} - 1\right\}$$

$$= 1 + \frac{(1+\alpha)a_2}{\gamma}\psi + \frac{(2(1+2\alpha)a_3 - (1+\alpha)^2 a_2^2)}{\gamma}\psi^2$$

$$+ \frac{[3(1+\alpha)a_4 - 3(1+\alpha)(1+2\alpha)a_2a_3 + (1+\alpha)^3 a_2^3]}{\gamma}\psi^3 + \cdots \quad (9)$$

By expanding $u(\psi)$ into its series form and applying elementary calculations, we obtain:

$$1 + sin(u(\psi)) = 1 - u(\psi) + \frac{(u(\psi))^3}{3!} - \frac{(u(\psi))^5}{5!} + \cdots$$

$$= 1 + \frac{1}{2}c_1\psi + \left(\frac{c_2}{2} - \frac{c_1^2}{4}\right)\psi^2 + \left(\frac{5c_1^3}{48} + \frac{c_3}{2} - \frac{c_1c_2}{2}\right)\psi^3 + \cdots \quad (10)$$

From equations (9), and (10), we obtain

$$a_2 = \frac{\gamma}{(1+\alpha)}c_1, \quad (11)$$

and

$$a_3 = \frac{\gamma}{4(1+2\alpha)}c_2 + \frac{\gamma}{4(1+2\alpha)}c_1^2(\gamma - 1). \quad (12)$$

Applying the relation (5) in (11), we obtain the required result. Furthermore, rearranging equation (12) gives:

$$|a_3| = \frac{1}{4(1+2\alpha)}|\gamma c_2 + \gamma c_1^2(\gamma - 1)|.$$

Applying the triangle inequality together with equation (5) leads to the desired result. Sharpness of the bounds can be demonstrated by the following function, corresponding to particular values of the parameters α and γ.

$$f(\psi) = \psi\, exp\left(\int_0^{\psi} \frac{sint - 1}{t}dt\right)$$

$$= \psi + \psi^2 + \frac{\psi^3}{2} + \frac{\psi^4}{9} + \cdots. \quad (13)$$

Remark 1. For $\alpha = 0$ in Theorem 1, we obtain the following new result for the subclass $\mathfrak{S}^*_{sin}(\gamma; \psi)$.

Theorem 2. Let $f \in \mathfrak{S}^*_{sin}(\gamma;\psi)$ and be given by (1), then
$|a_2| \leq |\gamma|$, and $|a_3| \leq \frac{|\gamma|}{2}(1+|\gamma-1|)$.
These bounds are sharp.

Remark 2. For $\propto = 0$ and $\gamma = 1$ in Theorem 1, we obtain the following known result for the subclass S^*_{sin}, investigted by Cho *et al.* [18].

Theorem 3. Let $f \in S^*_{sin}$, be given by equation (1) Then,

$|a_2| \leq 1$, and $|a_3| \leq \frac{1}{2}$.
Equality in these bounds is attained by the function (13).

Remark 3. Setting $\propto = 1$ in Theorem 1 yields a new result for the subclass $\mathfrak{C}_{sin}(\gamma;\psi)$, as stated below:

Theorem 4. Let $f \in \mathfrak{C}_{sin}(\gamma;\psi)$ be given by (1) Then,

$|a_2| \leq \frac{|\gamma|}{2}$, and $|a_3| \leq \frac{|\gamma|}{6}(1+|\gamma-1|)$.
The bounds are sharp for $\gamma = 1$ and equality is attained by the function:

$$1+\frac{1}{\gamma}\left\{\frac{\psi f''(\psi)}{f'(\psi)}\right\} = 1+sin(\psi). \qquad (14)$$

Remark 4. For $\propto = 1$ and $\gamma = 1$ in Theorem 1, we obtain the following known result for the subclass C_{sin}, studied by Arif *et al.* [19].

Theorem 5. Let $f \in C_{sin}$, and be given by equation (1). Then,

$|a_2| \leq \frac{1}{2}$, and $|a_3| \leq \frac{1}{6}$.

Equality in these bounds are attained by the function described in equation (14).

4.2. Fekete-Szegö Problem

We now investigate the Fekete-Szegö functional for functions belonging to the subclass $\Re_{sin}(\propto,\gamma;\varphi_{sin})$

Theorem 6. If a function f of the form equation (1) belongs to $\Re_{sin}(\propto,\gamma;\varphi_{sin})$ then
$|a_3-\lambda a_2^2| \leq \frac{|\gamma|}{2(1+2\propto)} max\left\{1,\left|\frac{2\lambda(1+2\propto)-(2\gamma-1)(1+\propto)^2}{(1+\propto)^2}\right|\right\}$.
This result is sharp.

Proof. If $f \in \Re_{sin}(\propto,\gamma;\varphi_{sin})$, then from equations (11) and (12), we obtain: $a_3-\lambda a_2^2$

$$= \frac{\gamma}{4(1+2\propto)}\left\{c_2-c_1^2\left(\frac{\lambda(1+2\propto)-(\gamma-1)(1+\propto)^2}{(1+\propto)^2}\right)\right\}.$$

Let,

$$v = \left(\frac{\lambda(1+2\propto)-(\gamma-1)(1+\propto)^2}{(1+\propto)^2}\right).$$

Therefore:

$$|a_3-\lambda a_2^2| = \frac{|\gamma|}{4(1+2\propto)}|c_2-vc_1^2|,$$

from Lemma 1, equation (6), it follows that for v, we obtained the required result. for specific values of $\propto$ and Υ, equality is achieved by the function defined in equation (13).

Remark 5. A new result for the subclass $\mathfrak{S}^*_{sin}(\gamma;\psi)$ is obtained by setting $\propto = 0$ in Theorem 6, as follow:

Theorem 7. Let $f \in \mathfrak{S}^*_{sin}(\gamma;\psi)$ be given (1). Then

$$|a_3-\lambda a_2^2| \leq \frac{|\gamma|}{2} max\{1,|2\lambda-(2\gamma-1)|\}.$$

Equality is achieved for $\gamma = 1$ by the function given in equation (13).

Remark 6. The choice $\propto = 0$ and $\gamma = 1$ in Theorem 6 gives the result established earlier for the class S^*_{sin} by Arif *et al.* [19].

Theorem 8. Suppose $f \in S^*_{sin}$ is be given (1). Then

$$|a_3-\lambda a_2^2| \leq \frac{1}{2} max\{1,|2\lambda-1|\}.$$

The result attains the best possible bound.

Remark 7. A new result and its corresponding corollary for the subclass $\mathfrak{C}_{sin}(\gamma;\psi)$ are obtained by setting $\propto = 1$ and $\lambda = 1$ in Theorem 6, respectively, as follows:

Theorem 9. Let $f \in \mathfrak{C}_{sin}(\gamma;\psi)$ be given (1). Then

$$|a_3-\lambda a_2^2| \leq \frac{|\gamma|}{6} max\left\{1,\frac{1}{2}|3\lambda-2(2\gamma-1)|\right\}.$$

Corollary 1. If $f \in \mathfrak{C}_{sin}(\gamma;\psi)$ with series form (1),

$$|a_3-a_2^2| \leq \frac{|\gamma|}{6}.$$

The inequality becomes sharp for the specific case $\gamma = 1$.

Remark 8. By setting $\propto = 1$, $\gamma = 1$ and $\lambda = 1$ in Theorem 6, we obtain the following known result and corollary for the class C_{sin}, investigated Arif *et al*. [19].

Theorem 10. Let $f \in C_{sin}$ be given (1). Then

$$\left|a_3 - \lambda a_2^2\right| \leq \frac{1}{6}\, max\left\{1, \frac{1}{2}|3\lambda - 2|\right\}.$$

Corollary 2. If $f \in C_{sin}$ with series form (1), then $\left|a_3 - a_2^2\right| \leq \frac{1}{6}$.
This inequality is sharp.

4.3. Radius Problem

In order discuss about the findings in this section, we first highlight a few known classes as follows: Let for $-1 \leq A_2 < A_1 \leq 1$,

$$\mathcal{P}[A_1, A_2] = \left\{p(\psi) = 1 + \sum_{k=n}^{\infty} c_n\, \psi^n : p(\psi) \prec \frac{1 + A_1\psi}{1 + A_2\psi}\right\}$$

denoted by

$$\mathcal{P}(\propto) = \mathcal{P}[1 - 2\propto, -1] \; and \; \mathcal{P} = \mathcal{P}(0).$$

For $f \in \mathfrak{A}$, if $p(\psi) = \frac{\psi f(\psi)}{f'(\psi)}$, then $\mathcal{P}[A_1, A_2]$ is represented by $S^*[A_1, A_2]$ and $S^*(\propto) = S^*[1 - 2\propto, -1]$. For this class, Cho *et al.* [18], determined the S^*_{sin} −radii for the class of Janowski starlike functions and some other geometrically defined classes including the classes

$$\mathfrak{S}_n = \left\{f \in \mathfrak{A} : \frac{f(\psi)}{\psi} \in \mathcal{P}\right\},\; S^*[A_1, A_2] \quad \text{and}$$

$$\mathcal{C}\mathfrak{S}_n = \left\{f \in \mathfrak{A}: \frac{f(\psi)}{g(\psi)} \in \mathcal{P},\; g \in S^*(\propto)\right\}$$

these classes were considered by Ali *et al.* [26].

This section aims to determine the $\mathfrak{S}^*_{sin}(\gamma; \varphi_{sin})$ − radius result for the subclass $\mathfrak{S}_n$ of Janowski starlike functions .

Theorem 11. The sharp $\mathfrak{S}^*_{sin}(\gamma; \varphi_{sin})$ −radius for the subclass $\mathfrak{S}_n$ is defined as:

$$R_{\mathfrak{S}^*_{sin}(\gamma;\varphi_{sin})}(\mathfrak{S}_n) = \left(\frac{sin1}{\sqrt{|\gamma|^2 n^2 + sin^2(1) + |\gamma|n}}\right).$$

Proof. Let $f \in \mathfrak{S}_n$, define $h(\psi) = \frac{f(\psi)}{\psi}$, so that $h \in \mathcal{P}$. Then

$$\frac{\psi f'(\psi)}{f(\psi)} - 1 = \frac{\psi h'(\psi)}{h(\psi)}.$$

Now, from the definition of the class $\mathfrak{S}^*_{sin}(\gamma; \varphi_{sin})$, we consider the function:

$$\chi(\psi) = 1 + \frac{1}{\gamma}\left(\frac{\psi f'(\psi)}{f(\psi)} - 1\right) = 1 + \frac{1}{\gamma}\left(\frac{\psi h'(\psi)}{h(\psi)}\right).$$

From Lemma 2, since $h \in \mathcal{P}$, it follows that:

$$\left|\frac{\psi h'(\psi)}{h(\psi)}\right| \leq \frac{2nr^n}{1 - r^{2n}} \; for \; |\psi| = r.$$

Thus,

$$|\chi(\psi) - 1| \leq \frac{2nr^n}{|\gamma|(1 - r^{2n})}.$$

From Lemma 3, the image of the function $\varphi_{sin}(\psi) = 1 + sin\psi$ contains the open disk:

$$\delta_{sin} = \{\mathcal{W} \in \mathbb{C}: |\mathcal{W} - 1| < sin1\}.$$

To ensure that $\chi(\psi) \prec 1 + sin\psi$, we require:

$$\frac{2nr^n}{|\gamma|(1 - r^{2n})} \leq sin1,$$

or equivalently, $|\gamma|(sin1)r^{2n} + 2nr^n - |\gamma|(sin1) \leq 0$.
Thus, the sharp radius R corresponds to the smallest positive root of the equation:

$$|\gamma|(sin1)r^{2n} + 2nr^n - |\gamma|(sin1) = 0.$$

To show sharpness, consider the function:

$$f_o(\psi) = \frac{1 + \psi^n}{1 - \psi^n} \in \mathcal{P},$$

then

$$\frac{\psi f_o'(\psi)}{f_o(\psi)} = 1 + \frac{2n\psi^n}{\gamma(1 - \psi^{2n})}$$

$$\Rightarrow |f_o(\psi) - 1| = \frac{2n\psi^n}{|\gamma|(1 - \psi^{2n})} = sin1.$$

This completes the proof.

Remark 9. When $\gamma = 1$, Theorem 11 coincides with the known sharp radius result for the subclass

S^*_{sin}, examineded by Cho *et al.* [18].

Theorem 12. The sharp S^*_{sin} −radius for the subclass $\mathfrak{S}_n$ is given by:

$$R_{S^*_{sin}}(\mathfrak{S}_n) = \left(\frac{sin1}{\sqrt{n^2 + sin^2(1) + n}}\right).$$

5. CONCLUSIONS

In this study, we introduce some new subclasses of analytic functions of complex order γ, defined via subordination involving the sine function. Sharp coefficient estimates, Fekete-Szegö inequalities, and a radius result for a certain class are also obtained. These findings not only support applications in conformal mapping and applied analysis but also enhance the current theory of univalent functions. Furthermore, a well-known class and its associated results are highlighted to demonstrate the connection between earlier research and the present findings.

6. CONFLICT OF INTEREST

The authors declare that they have no conflict of interest.

7. REFERENCES

1. P.L. Duren (Ed.). Univalent functions. Part of the book series: Grundlehren der mathematischen Wissenschaften (Volume 259). *Springer-Verlag, New York* (1983).
2. A. Aleman and A. Constantin. Harmonic maps and ideal fluid flows. *Archive for Rational Mechanics and Analysis* 204: 479-513 (2012).
3. A.W. Goodman (Ed.). Univalent functions. Vol. I & II. *Mariner Publishing Company* (1983).
4. C. Tom (Ed.). Univalent functions: The Basics (Chapter 8). In: Geometric Function Theory. *Springer, Cham, Switzerland* pp. 203-225 (2024).
5. D.K. Thomas, N. Tuneski, and A. Vasudevarao (Eds.). Univalent functions. Part of: De Gruyter Studies in Mathematics. *De Gruyter, Berlin* (2018).
6. W. Ma and D. Minda. A unified treatment of some special classes of functions. In: Proceedings of the Conference on Complex Analysis. Nankai Institute of Mathematics, *Nankai University, Tianjin, China* pp. 157-169 (1992).
7. V. Ravichandran, P. Yasar, B. Metin, and S. Arzu. Certain subclasses of starlike and convex functions of complex order. *Hacettepe Journal of Mathematics and Statistics* 34: 9-15 (2005).
8. M. Fekete and G. Szegö. Eine Bemerkung Über ungerade schlichte Funktionen. *Journal of the London Mathematical Society* 8: 85-89 (1933).
9. L. Bieberbach. Über die Koeffizienten derjenigen Potenzreihen welche eine schlichte Abbildung des Einheitskreises vermitteln. *Sitzungsberichte der Preussischen Akademie der Wissenschaften* 138: 940-955 (1916).
10. L. de Branges. A proof of the Bieberbach conjecture. *Acta Mathematica* 154: 137-152 (1985).
11. N.E. Cho, V. Kumar, and V. Ravichandran. A survey on coefficient estimates for Caratheodory functions. *Applied Mathematics E-Notes* 19: 370-396 (2019).
12. A.A. Bhatti, A.W. Shaikh, and S.A. Shah. Coefficient bounds for certain classes of analytic functions of complex order γ associated with cardioid domain. *Proceedings of the Pakistan Academy of Sciences: Physical and Computational Sciences* 62(2): 131-136 (2025).
13. Y.J. Sun, M. Arif, L. Shi, and M.I. Faisal. Some further coefficient bounds on a new subclass of analytic functions. *Mathematics* 11(12): 2784 (2023).
14. A. Ahmed, A.W. Shaikh, and S.A. Shah. Fekete-Szegö problem for certain analytic functions of complex order associated with cardioid domain. *International Journal of Analysis and Applications* 23: 109-109 (2025).
15. R. Biswas and R. Mandal. A geometric investigation of a certain subclass of univalent functions. *arXiv preprint arXiv*:2411.04235 (2024).
16. R.M. Ali, N. Jain, and V. Ravichandran. On the radius constants for classes of analytic functions. *arXiv preprint arXiv*:1207.4529 (2012).
17. W. Janowski. Some extremal problems for certain families of analytic functions I. *Annales Polonici Mathematici* 28(3): 297-326 (1973).
18. N.E. Cho, V. Kumar, S.S. Kumar, and V. Ravichandran. Radius problems for starlike functions associated with the sine function. *Bulletin of the Iranian Mathematical Society* 45: 213-232 (2019).
19. M. Arif, M. Raza, H. Tang, S. Huo, S. Hussain, and H. Khan. Hankel determinant of order three for familiar subsets of analytic functions related with sine function. *Open Mathematics* 17: 1615-1630 (2019).
20. H.M. Srivastava, K. Nazar, A.B. Muhtarr, A. Ayman, M.T. Ferdous, and S. Zainab. Fourth order Hankel determinants for certain subclasses of modified sigmoid-activated analytic functions involving the trigonometric sine function. *Journal of Inequalities*

and Applications 84: 84 (2024).
21. H. Tang, M. Gangadharan, L. Shu-Hai, and M. Li-Na. Fekete-Szegö and Hankel inequalities for certain class of analytic functions related to the sine function. *AIMS Mathematics* 7: 6365-6380 (2022).
22. S.B. Al-Shaikh, K. Matarneh, A.A. Abubaker, and M.F. Khan. Sharp Coefficient Bounds for a New Subclass of Starlike Functions of Complex Order γ Associated with Cardioid Domain. *Mathematics* 11(9): 2017 (2023).
23. C. Pommerenke (Ed.). Univalent Functions. *Vandenhoeck and Ruprecht, Göttingen* (1975).
24. F.R. Keogh and E.P. Merkes. A coefficient inequality for certain classes of analytic functions. *Proceedings of the American Mathematical Society* 20: 8-12 (1969).
25. G.M. Shah. On the univalence of some analytic functions. *Pacific Journal of Mathematics* 43: 239-250 (1972).
26. R.M. Ali, N.K. Jain, and V. Ravichandran. Radii of starlikeness associated with the lemniscate of Bernoulli and the left-half plane. *Applied Mathematics and Computation* 218(11): 6557-6565 (2012).

Instructions For Authors

Manuscript Writing

The manuscript may contain a Title, Abstract, Keywords, INTRODUCTION, MATERIALS AND METHODS, RESULTS, DISCUSSION (or RESULTS AND DISCUSSION), CONCLUSIONS, ETHICAL STATEMENT (if applicable), ACKNOWLEDGEMENTS, CONFLICT OF INTEREST and REFERENCES, *and any other information that the author(s) may consider necessary*.

Title (Bold and font size 16): The title should be expressive, concise, and informative to the entire readership of the journal. It may include common terms, to make it more identifiable when people search online. Please avoid the use of long pervasive terms and non-standard or obscure abbreviations, acronyms, or symbols.

Abstract (font size 10, max 250 words)**:** Must be self-explanatory**,** stating the rationale, objective(s), methodology, main results, and conclusions of the study. Abbreviations, if used, must be defined on the first mention in the Abstract as well as in the main text. Abstracts of review articles may have a variable format.

Keywords (font size 10)**:** Provide five to eight keywords consisting of words and phrases that are closely associated with the topic depicting the article.

INTRODUCTION (font size 11)**:** Provide a clear and concise statement of the problem, citing relevant recent literature, and objectives of the investigation. Cite references in the text by number in square brackets**,** the reference must be cited in a proper English sentence [1]. or "... as previously described [3, 6–8]". For a single author: Bednorz [2] investigated the environmental pollution ... When there are only two authors: Bednorz and Allan [2] investigated the environmental pollution ... and for three or more authors: Bednorz *et al.* [2] investigated the environmental pollution ..; and list them in the REFERENCES section, in the order of citation in the text.

MATERIALS AND METHODS (font size 11)**:** Provide an adequate account of the procedures or experimental details, including statistical tests (if any), concisely but sufficiently enough to replicate the study. Relevant references to methodology must be cited.

RESULTS (font size 11)**:** Be clear and concise with the help of appropriate Tables, Figures, and other illustrations. Data should not be repeated in Tables and Figures but must be supported with statistics. The data presented in Tables and Figures must be elaborated in the main text.

DISCUSSION (font size 11)**:** Provide interpretation of the RESULTS in the light of previous relevant studies, citing published references.

CONCLUSIONS (font size 11)**:** Briefly state the implication of your study findings, and carefully address the study questions. Confine your conclusions according to the objectives of your study and the aspects covered in the abstract. Discuss both positive and negative findings.

ETHICAL STATEMENT (font size 10)**:** The statement of ethical approval by an appropriate ethics committee or review board must be included in the manuscript (if applicable), as per the Journal's policy.

ACKNOWLEDGEMENTS: (font size 10)**:** In a brief statement, acknowledge the financial support and other assistance.

CONFLICT OF INTEREST (font size 10)**:** State if there is any conflict of interest.

REFERENCES (font size 10)**:** References must be listed in numerical order as listed in the main text. Only published (and accepted for publication) journal articles, books and book chapters, conference proceedings, online reports, a degree thesis, and materials available on the website qualify for REFERENCES.

Declaration: Provide a declaration that: (i) the results are original, (ii) the same material is neither published nor under consideration for publication elsewhere, (iii) approval of all authors has been obtained, and (iv) in case the article is accepted for publication, its copyright will be assigned to the *Pakistan Academy of*

Sciences. Authors must obtain permission to reproduce, where needed, copyrighted material from other sources and ensure that no copyrights are infringed upon.

Manuscript Formatting

Manuscripts must be submitted in Microsoft Word (Latest Version .doc or .docx format); pdf files are not acceptable. Figures can be submitted separately in TIFF, GIF, JPEG, EPS, or PPT. Manuscripts, in *Times New Roman*, 1.15 spaced (but use single-space for Tables, long headings, and long captions of tables and figures). The Manuscript sections must be numbered, i.e., **1. INTRODUCTION, 2. MATERIALS AND METHODS,** and so on… (a) **Title** of the article **(**Capitalize the initial letter of each main word, font-size 16, **bold**), max 160 characters (no abbreviations or acronyms), depicting article's contents; (b) Author's complete name (font size 12, **bold**), and professional affiliation (i.e., each author's Department, Institution, Mailing address, and Email and Contact number, but no position titles) (font size 12); (c) Indicate the corresponding author with *; and (d) **Short running title**, max 50 characters (font size 10).

Headings and Subheadings (font size 11): All flush left

LEVEL-1: **ALL CAPITAL LETTERS; Bold**

Level-2: **Capitalize Each First Letter (**Except prepositions**); Bold**

Level-3: Capitalize the first letter only (Sentence case)***; Bold, Italic***

Level-4: *Run-in head*; *Italics*, *in the normal paragraph position. Capitalize the first letter only and end in a colon (i.e., **:**)*

A list of REFERENCES must be prepared as under:

a. Journal Articles *(Name of journals must be stated in full)*

1. J. Rashid, A. Ahsan, M. Xu, I. Savina, and F. Rehman. Synthesis of cerium oxide embedded perovskite type bismuth ferrite nanocomposites for sonophotocatalysis of aqueous micropollutant ibuprofen. *RSC Advances* 13(4): 2574-2586 (2023).
2. A. Fayyaz, N. Ali, Z.A. Umar, H. Asghar, M. Waqas, R. Ahmed, R. Ali, and M.A. Baig. CF-LIBS based elemental analysis of Saussurea simpsoniana medicinal plant: a study on roots, seeds, and leaves. *Analytical Sciences* 40(3): 413-427 (2024).
3. W. Bialek and S. Setayeshgar. Cooperative sensitivity and noise in biochemical signaling. *Physical Review Letters* 100: 258–263 (2008).

b. Books

4. W.R. Luellen (Ed.). Fine-Tuning Your Writing. *Wise Owl Publishing Company, Madison, WI, USA* (2001).
5. U. Alon and D.N. Wegner (Eds.). An Introduction to Systems Biology: Design Principles of Biological Circuits. *Chapman & Hall/CRC, Boca Raton, FL, USA* (2006).

c. Book Chapters

6. M.S. Sarnthein, J.E. Smolen, and J.D. Stanford. Basal sauropodomorpha: historical and recent phylogenetic developments. In: The Northern North Atlantic: A Changing Environment. P.R. Schafer and W. Schluter (Eds.). *Springer, Berlin, Germany* pp. 365–410 (2000).
7. S. Brown and L.A. Boxer. Functions of Europhiles. In: Hematology, (4th ed). W.J. Williams, E. Butler, and M.A. Litchman (Eds.). *McGraw Hill, New York, USA* pp. 103–110 (1991).

d. Reports

8. M.D. Sobsey and F.K. Pfaender. Evaluation of the H_2S method for Detection of Fecal Contamination of

Drinking Water. Report No.-WHO/SDE/WSH/02.08. *Water Sanitation and Health Programme, WHO, Geneva, Switzerland* (2002).

e. Online References

These should specify the full URL for reference, please check again to confirm that the work you are citing is still accessible:

9. UNESCO. Global Education Monitoring Report 2024/5: Leadership in education−Lead for learning. *United Nations Educational, Scientific and Cultural Organization, Paris, France* (2024). https://digitallibrary.un.org/record/4066661?ln=en&v=pdf

10. L.M. Highland and P. Bobrowsky. The landslide handbook−A guide to understanding landslides. Circular 1325. *US Geological Survey, Reston, Virginia* (2008).

    https://pubs.usgs.gov/circ/1325/pdf/C1325_508.pdf

f. Conference Proceedings

11. M. Khalid, A.B. Majid, F. Mansour, and C.R. Smith. Word Representations with Recursive Neural Networks for Morphology. *27th European Conference on Signal Processing, (2nd - 6th September 2021), Madrid, Spain* (2021).

g. A Degree Thesis

12. M. Afzal. Investigation of structural and magnetic properties of nanometallic Fe-Mn Alloys. Ph.D. Thesis. *Quaid-i-Azam University, Islamabad, Pakistan* (2023).

Tables: Insert all tables as editable text, not as images. Number tables consecutively following their appearance in the text. A concise but self-explanatory heading must be given. Tables should be numbered according to the order of citation (like **Table 1.**, **Table 2.** (font size 10)). *Do not* abbreviate the word "Table" to "Tab.". Round off data to the nearest three significant digits. Provide essential explanatory footnotes, with superscript letters or symbols keyed to the data. Do not use vertical or horizontal lines, except for separating column heads from the data and at the end of the Table.

Figures: In the main text write Figure, not Fig. Figures may be printed in two sizes: column width of 8.0 cm or page width of 16.5 cm; In the Figure caption, number them as **Fig. 1.**, **Fig. 2.** Captions to Figures must be concise but self-explanatory (font size 10). Laser-printed line drawings are acceptable. Do not use lettering smaller than 9 points or unnecessarily large. Photographs must be of high quality. A scale bar should be provided on all photomicrographs. All Figures should have sufficiently high resolution (minimum 300 dpi) to enhance the readability. Figures as separate files in JPG or TIFF format may be provided.

SUBMISSION CHECKLIST

The following list will be useful during the final checking of an article before submission to the journal.

1. Manuscript in MS Word format
2. Cover Letter
3. Novelty Statement
4. Copyright Form
5. Figures in JPG or TIFF format

In case of any difficulty while submitting your manuscript, please get in touch with:

Editor-in-Chief

Pakistan Academy of Sciences
3-Constitution Avenue,
G-5/2, Islamabad, Pakistan
Email: editor@paspk.org
Tel: +92-51-920 7140
Websites: http://www.paspk.org/proceedings/; http://ppaspk.org/

PROCEEDINGS OF THE
PAKISTAN ACADEMY OF SCIENCES: PART A
Physical and Computational Sciences

CONTENTS

Volume 62, No. 3, September 2025 **Page**

Research Articles

Instructions for Authors

Websites: http://www.paspk.org/proceedings/; http://ppaspk.org

PAKISTAN ACADEMY OF SCIENCES, ISLAMABAD, PAKISTAN

HEC Recognized; Scopus Indexed